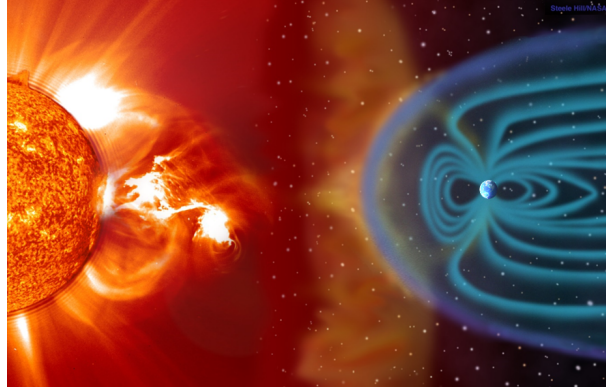


Space Weather Drivers and their Geoeffectiveness



A Thesis Submitted for the degree of

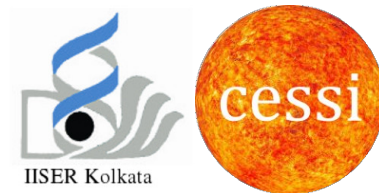
Doctor of Philosophy

by

Sanchita Pal (15RS036)

under the supervision of

Prof. Dibyendu Nandi



Centre of Excellence in Space Sciences India
Indian Institute of Science Education and Research Kolkata

December 2020

Declaration by the Student

Date: 22 July 2020

I, Ms. Sanchita Pal (Registration No. 15RS036 dated 24th July 2015), a student of the PhD program of the Center of Excellence in Space Sciences India (CESSI), IISER Kolkata, hereby declare that this thesis is my own work, and, to the best of my knowledge, it neither contains materials previously published or written by any other person, nor has it been submitted for any degree, diploma or any other academic award anywhere before. I have used the originality checking service to prevent inappropriate copying. I also declare that all copyrighted material incorporated into this thesis is in compliance with the Indian Copyright Act, 1957 (amended in 2012) and that I have received written permission from the copyright owners for my use of their work. I hereby grant permission to IISER Kolkata to store the thesis in a database which can be accessed by others.

Sanchita Pal.

Sanchita Pal

Center of Excellence in Space Sciences India

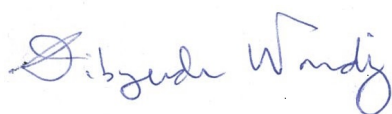
Indian Institute of Science Education and Research Kolkata

Mohanpur 741246, West Bengal, India

Certificate from the Supervisor

Date: 22 July 2020

This is to certify that the thesis entitled "Space Weather Drivers and their Geoeffectiveness" submitted by Ms. Sanchita Pal (Registration No. 15RS036 dated 24th July 2015), a student of the PhD program of the Center of Excellence in Space Sciences India (CESSI), IISER Kolkata, is based upon her own research work under my supervision. This is also to certify that neither the thesis nor any part of it has been submitted for any degree, diploma or any other academic award anywhere before. In my opinion, the thesis fulfils the requirement for the award of the degree of Doctor of Philosophy.



Dr. Dibyendu Nandi

Professor

Center of Excellence in Space Sciences India

Department of Physical Sciences

Indian Institute of Science Education and Research Kolkata

Mohanpur 741246, West Bengal, India

Acknowledgements

During my post-graduation, I took a few courses on space science which made me curious about our space environment and its connection to solar activity which motivated me to dedicate my career to studying the Sun and space weather. It has been almost five years since I started my journey as a Ph.D. scholar, and there are many people whose encouragement and inspiration helped me accomplish this journey. I am thankful to Dr. Ashik Paul and Dr. Sarbani Ray from IRPE, University of Calcutta, who encouraged me during my postgraduate days to be a part of this research field.

The enthusiasm and dedication of my supervisor Dr. Dibyendu Nandi to the advancement of science has inspired me and driven me to reach the verge of acquiring a Ph.D. degree. His valuable insights and experience in solar physics consistently led me to proceed in the right direction. His way of guidance has allowed me to develop ideas of my own and to independently explore new scientific problems. Apart from this, I am grateful to him for teaching me how to present and highlight my research works in front of other experts as well as amateurs. I express my gratitude to Dr. Nat Gopalswamy and Dr. Seiji Yashiro for hosting me as a SCOSTEP Visiting Scholar at NASA/Goddard Space Flight Center and helping me build up skills that have been extensively used in my research work. I would like to thank Prof. Nandita Srivastava, Dr. Benoit Lavraud, Dr. K. Marubashi and Dr. R. P. Lepping for helpful suggestions and useful discussions which benefited my research.

This research has been supported by the Ministry of Human Resource Development (MHRD), Govt. of India, under the Frontier Areas of Science and Technology (FAST) scheme through funding to the Center of Excellence in Space Sciences India (CESSI). I am grateful to several national and international astronomy and space science communities for providing support for attending conferences, schools, and opportunities to present my research.

I sincerely thank our system administrator, Mr. Prosenjit Lahiri, for his active help in technical and administrative needs. I express my gratitude to Dr. Rajesh k. Nayak, Head of the Department, CESSI, and IISER Kolkata administration for their help on many occasions.

A huge thanks to the past and present members of my CESSI family including, Prantika, Lekshmi, Soumya, Suvadip, Maitreya, Suman, Srijan, Avyarthana, Rakesh, Souvik, Shaonwita, Athira, Amar, Aditi, Ranaeep, Sajal, Arghya and Arnab with whom I have gathered a lot of fond memories over the last few years. I am thankful to my seniors from CESSI, who were always ready to clarify my doubts on solar physics and answer my queries. I would like to especially thank Arnab, Lekshmi, and Arghya for reading and commenting on earlier drafts of my thesis. They have always been an excellent company over the past five years.

The last five years of my life have been the most extraordinary ones filled with memories that can be cherished over my lifetime. I met a few crazy people after joining here in IISER Kolkata including, Dipanjan, Manna, Avijit, Anurag, Deban-gana and Tapas, who made my days awesome and enjoyable. Starting from in-depth discussion on politics, chit chat on several topics most of the evenings, we enjoyed several nights together with good food and beverages. I am so lucky to have my childhood best friend Sangita by my side in person through all ups and downs. I will miss our cooking of unusual items with ordinary things and visiting numerous places on most of the weekend afternoons.

It is hard to express my gratitude to my family in words. The positive attitude of my Baba and Didi has inspired me always to accept any new challenge. I admire Didi's dedication towards her research, which has always encouraged me to pursue my research interests. I will be indebted to my parents for supporting all my aspirations unconditionally. My Maa's strong desire led me to pick up skills in playing instruments and singing, which has helped me refresh my mind in between my research works. Last but not the least, I express my love and gratitude to Sounak. He has always helped me make important decisions in my life, pushed me to believe in myself, and mirrored me to the bright side of myself to grow my confidence.

Time has come to bid goodbye to the most exciting and beautiful days of my life

till now and move on to shape the next phase of my life; holding memories because only memories can bring back all those days.

Synopsis

Understanding the Earth's natural environment for forecasting day to day variability of the planetary atmospheric state is of utmost importance and constitutes one of the oldest human endeavors that began in the 18th century. With the advent of the space age in the 20th century, the effects of space weather were gradually uncovered, and subsequently, its exploration was initiated. Space weather originates at the Sun and is primarily driven by intense solar activities, which often manifest as large-scale magnetized plasma being ejected into the heliosphere. Such a phenomenon is known as a Coronal Mass Ejection (CME).

CMEs often inject energetic particles and large amounts of energy into the Earth's magnetosphere thereby resulting in geomagnetic storms. Their impact on the planetary space environments is capable of causing severe harm to satellites, space-based technologies, health of astronauts involved in long-duration space missions, global communication and navigation systems, air-traffic on polar routes and high-voltage power grids. The ability of CMEs to drive geomagnetic storms is referred to as geoeffectiveness. The geoeffectiveness of CMEs depend on their kinematics and magnetic properties, which might evolve in the course of their interplanetary propagation. Forecasting space weather through prior estimation of the geoeffectiveness of CMEs is quite a challenging task as it has to be made in a dynamic and complex solar-terrestrial system with considerable accuracy, reliability and timeliness.

This research presented in this dissertation investigates and thereby, improves the current understanding of the probable origin and Sun-Earth evolution of the properties determining the geoeffectiveness of CMEs. With an intention to predict the geoeffectiveness of CMEs, we attempt to constrain their magnetic structures before they arrive at Earth. We begin in Chapter 1 with an overview of space weather, its origins, drivers and potential effects on Earth, and subsequently,

provide an outline of the connections between the properties of one of the significant space weather drivers, i.e., CMEs, and their geoeffectiveness. CMEs are born in solar magnetic structures, whose properties ascertain their associated eruption characteristics. Although the ambient solar wind influences interplanetary CMEs (ICMEs), the inherent features of ICMEs are determined by the properties of their associated CMEs and solar sources.

The near-Sun kinematics of CMEs determine the severity and arrival time of the resulting geomagnetic storms. We investigate the relationship between the deprojected speed and kinetic energy of CMEs and magnetic measures of their solar sources and intrinsic flux rope characteristics. The near-Sun velocity and kinetic energy of CMEs are found to be well correlated with the associated magnetic reconnection flux. On the contrary, the correlation between CME speed and their source active region size & global nonpotentiality is found to be comparatively weak. A statistically significant empirical relationship is found between the CME speed and reconnection flux which may be utilized for prediction purposes. Apart from this, we find that CME kinematics are related to the axial magnetic field intensity and relative magnetic helicity of their intrinsic flux ropes. These results constrain processes related to the origin and propagation of CMEs and may lead to better empirical forecasting of their arrival speed, time and geoeffectiveness. This research is reported in [Chapter 2](#).

The proper understanding of the origin and evolution of the magnetic properties is necessary for determining the geoeffectiveness of Earth-directed interplanetary coronal mass ejections (ICMEs). We compare their magnetic properties, specifically magnetic flux and helicity with those of their solar sources with the aim of understanding the origin of magnetic properties of flux ropes. The magnetic helicity describes the twisting, writhing and linking of ICME flux ropes at 1 AU. It is observed that the poloidal flux and helicity of 1-AU flux ropes, i.e., magnetic clouds (MCs) are highly relevant to low-corona magnetic reconnection at the associated eruption site. In contrast to the above, the toroidal flux of MC flux ropes is a fraction of the total magnetic reconnection flux. These results indicate that CMEs are formed due to low-coronal magnetic reconnection at their solar sources, a process that transfers magnetic properties to the flux ropes. This research is reported in

Chapter 3.

While interacting with the ambient solar wind magnetic fields (i.e., heliospheric open flux) during interplanetary passages, MCs may lose a substantial amount of their initial magnetic flux via magnetic reconnection, which in some cases, reduce their geoeffectiveness. A linear correlation is found between the eroded flux of MCs and solar open flux, which is consistent with the scenario that MC erosion is mediated via the local heliospheric magnetic field draping around an MC during its interplanetary propagation. The solar open flux is governed by the sunspot cycle. Thus, we uncover a hitherto unknown pathway for solar cycle modulation of the properties of MCs. This research is reported in Chapter 4.

The MCs having prolonged southward magnetic field components are bound to expose the Earth's atmosphere to the heliospheric environment via magnetic reconnection. Thus, it is essential to predict the magnetic profile of Earth-directed MCs to estimate their geomagnetic responses. The configuration of a flux-rope CME can be approximated as a radially expanding force-free cylindrical structure. Near-Sun geometrical, magnetic and kinetic properties of CMEs are combined with the self-similarly expanding force-free cylindrical model to forecast the magnetic vectors within the Earth-directed segments of MCs. A proper estimation of near-Sun CME properties can lead to prediction of MC magnetic profiles with minimum deviations from their in situ observations. We employ this approach and devise a methodology that is quite successful in predicting near-Earth magnetic profile of MCs. This research is reported in Chapter 5.

The ultimate goal of this thesis is to investigate the key factors governing the geoeffectiveness of CMEs and devise improved methodologies for predicting their geoeffectiveness – thereby contributing significantly to understanding and forecasting space weather. We conclude with a brief discussion in Chapter 6.

This thesis research has been reported in the three publications listed below. The Chapters 2, 3 and 4 are reproductions of the publications with minor changes and additional clarifications, where appropriate.

Publications from this Thesis Research

1. “A Sun-to-Earth analysis of magnetic helicity of the 2013 March 17–18 interplanetary coronal mass ejection”, **S Pal**, N Gopalswamy, D Nandy, S Akiyama, S Yashiro, P Makela, H Xie, 2017, The Astrophysical Journal 851 (2), 123.
2. “Dependence of coronal mass ejection properties on their solar source active region characteristics and associated flare reconnection flux”, **S Pal**, D Nandy, N Srivastava, N Gopalswamy, S Panda, 2018, The Astrophysical Journal 865 (1), 4.
3. “Flux erosion of magnetic clouds by reconnection with the Sun’s open flux”, **S Pal**, S Dash, D Nandy, 2020, , Geophysical Research Letters, 47(8), e2019GL086372.

Contents

Synopsis	ix
1 Introduction	1
1.1 What is space weather?	1
1.2 The trigger of space weather: The Sun	2
1.2.1 The solar interior and atmosphere	3
1.2.2 The solar magnetic field	4
1.2.3 Solar activity	7
1.3 Coronal mass ejections (CMEs) as a space weather driver	10
1.3.1 CME initiation mechanisms	12
1.3.2 Signatures of CME initiation	16
1.3.3 Several properties of CMEs	19
1.3.4 Interplanetary manifestations of CMEs	24
1.4 Space weather consequences: Geomagnetic storms	28
1.4.1 Geomagnetic indices	31
1.4.2 The CME link to geomagnetic disturbances	32
1.5 Motivation and thesis outline	33
2 Dependence of CME kinematics on their solar source active regions	37
2.1 Introduction	37
2.2 Methodology	40
2.2.1 Magnetic properties of ARs and CMEs	44
2.3 Analysis and Results	48
2.3.1 Magnetic properties of ARs versus associated CME speeds	49

2.3.2	Kinetic properties versus magnetic properties of CMEs	54
2.4	Discussion	54
2.5	Conclusions	57
3	Investigating the origin of CME magnetic properties	59
3.1	Introduction	60
3.2	Observations	61
3.2.1	in situ observation of ICMEs at 1 AU	62
3.2.2	Identification and observation of ICME solar sources	63
3.3	Methodology	65
3.3.1	Analysis of ICME data	65
3.3.2	Analysis of ICME associated solar sources	71
3.4	Results and Discussion	76
3.5	Summary and Conclusions	80
4	Flux erosion of CMEs during their interplanetary propagation	81
4.1	Introduction	81
4.2	Instrumentation and overview of data	85
4.2.1	MC events and criteria for selection	85
4.3	Analysis methodology	86
4.3.1	Measurement of MC's eroded magnetic flux	87
4.3.2	Estimation of the Sun's open flux	88
4.4	Analysis and Results	91
4.4.1	Distribution of the MC's eroded azimuthal magnetic flux	93
4.4.2	Comparison between the Sun's unsigned open flux and MC flux erosion	93
4.5	Discussion	96
4.6	Conclusions	97
5	An approach for forecasting the magnetic profiles of Earth-directed CMEs	99
5.1	Introduction	100
5.2	Methodology: Modeling of MCs using near-Sun observations	102
5.2.1	Model description	102

5.2.2	Estimates of the geometrical properties of flux ropes	105
5.2.3	Estimation of flux-rope's near-Sun magnetic properties	107
5.2.4	Estimation of the arrival time and speed of CMEs	113
5.2.5	Coordinate conversion of magnetic field vectors	115
5.3	Results: Model validation using observed MC events	115
5.3.1	Preparation of model inputs	116
5.3.2	Model outputs	118
5.4	Discussion	123
5.5	Conclusions	124
6	Concluding remarks	127
	Bibliography	131

Chapter 1

Introduction

1.1 What is space weather?

On the morning of September 1, 1859, Richard Carrington, a British astronomer, was sketching a large group of sunspots from a projected image of the Sun in his private observatory in Redhill (Surrey). Suddenly, his attention was drawn to an extremely bright white light patch over the cluster of the large dark spots that gradually contracted to a pinpoint and disappeared within about sixty seconds of its appearance. On that same night, the skies above polar to low-latitude regions close to the equator were illuminated by very bright, colorful, stunning auroras. In the following day, the telegraph communications across Europe and North America malfunctioned due to the existence of a powerful magnetic storm resulting from the solar explosion. This event came to be known as “*Carrington event*” (Carrington, 1859), which was named after the amateur astronomer. On 15 May 1921, the electrical systems controlling train movements at the Grand Central station of New York were disrupted as an adverse impact of geoelectric fields induced by major geomagnetic storms resulting from series bombardments of solar explosions on the Earth (Hapgood, 2019). In 1972 and 1989, two more severe to extreme solar storms (Flynn et al., 2018; Allen et al., 1989) occurred and caused extensive disturbances in the electrical and communication grids of North America and Quebec, respectively. A severe power outage, satellite malfunction, and disruptions in space-based navigation systems followed two more massive storms, known as the “*Bastille Day*” (Andrews, 2001) and the “*Halloween*” storm (Lopez, Baker, and Allen, 2004) which

occurred in 2000 and 2003, respectively. In November 2015, flights in Sweden disappeared for more than one hour from the air traffic control screen as a consequence of a strong magnetic storm. These events serve as good examples showing how the technology dependent modern society is susceptible to space weather effects.

The term “*space weather*” came into popular use in the 1990s. It is derived from the terminologies – “*Solar meteorology*”, “*magnetic weather*”, and “*cosmic meteorology*” from the middle to late 1800s (Cade III and Chan-Park, 2015). Space weather refers to disturbances in the Earth’s space environment caused due to conditions on the Sun and its atmosphere. Alongside other natural hazards like pandemics, volcanic activity, earthquake and extreme temperatures, space weather is now regarded as a major societal risk (OECD, 2018). A formal definition of space weather introduced in “Understanding space weather to shield society: A global road map for 2015-2025 commissioned by COSPAR and ILWS” (Schrijver et al., 2015) is as follows: *Space weather refers to the variable state of the coupled space environment related to changing conditions on the Sun and in the terrestrial atmosphere, specifically those conditions that can influence the performance and reliability of space-borne and ground-based technological systems, and that can directly or indirectly endanger human well-being.* With the advent of the space age, a detailed understanding of responses of space environment to the disturbances produced by solar transient events becomes imperative in mitigating the technological and societal impacts of space weather. Through reliable predictions, efficient warning, and infrastructure designing, a better way of shielding modern society against space weather effects can be achieved.

1.2 The trigger of space weather: The Sun

Since the early days of human civilization, the Sun has been revered for its power of sustaining life on Earth. It produces light and heat which maintain the Earth’s atmosphere, influence the planet’s climate and make life possible. On the other hand, its violent activities are the roots of inclement space weather which has profound impact on solar system planets as well as the whole interplanetary space extending to the far end of the heliosphere. The Sun is a G-type main-sequence star which

came into existence as a result of the collapse of an interstellar gas cloud that initially reached an equilibrium due to the balance between the outward pressure force (due to nuclear energy generation) and the inward gravitational force. It has a mass of $M_{\odot} = 1.99 \times 10^{30}$ kg contained in a sphere of radius $R_{\odot} = 6.96 \times 10^8$ m (Lang, 2013). It holds about 99% of the total mass of the solar system and consists of 73.46% hydrogen, 24.85% helium and about 1.69% heavy elements including oxygen, carbon, neon, and iron, by mass.

1.2.1 The solar interior and atmosphere

The solar interior has a layered structure. The core which is located at the center of the Sun is the crucible for thermonuclear fusion that converts hydrogen into helium and releases energy in the form of gamma-ray photons. The energy propagates toward the radiative zone that extends out to approximately 72.5% of the solar radius from the core. In this region, the photons generated at the core are repeatedly absorbed and emitted. The re-emitted photons have longer wavelengths and lower energies. Above the radiative zone, there exists the convective zone that rotates differentially and transports energy to the solar surface (also known as the photosphere) by convection (e.g., Priest, 1995). At this zone, the temperature decreases rapidly with increasing height and becomes around 5700 K at the solar surface. The transition layer between the radiative and convective zones is known as the tachocline that is located at 0.675-0.725 R_{\odot} . The temperature and density decrease with increasing distance from the core to the photosphere. A pictorial representation of the layer-wise structure of the Sun is given in Figure 1.1.

The solar atmosphere begins at the solar surface and merges with the heliosphere. Based on the density, temperature and composition profiles of plasma, the solar atmosphere is subdivided into three layers: the photosphere, chromosphere and corona. The photosphere is composed of convection cells known as granules having a life-span of the order of ten minutes and an average size of 1000-2000 kilometers. The plasma density decreases from the photosphere to the corona. Due to the low density of plasma, the solar atmosphere is only visible while the brighter photosphere is obscured. The temperature falls gradually from the photosphere to the base of the chromosphere, then slowly increases until there is a drastic rise to

about a million Kelvins at the solar corona. The reason for this unexpected heating of solar corona is still an unsolved question and is known as *coronal heating problem* (Grotrian, 1939; Gudiksen, 2004; Klimchuk, 2015; Klimchuk, 2006; Downs et al., 2016). Studies propose that the plausible reasons of coronal heating are the dissipation of Alfvén waves (Asgari-Targhi et al., 2013) and small-scale impulsive heating events like nanoflares (Ishikawa et al., 2017). The Alfvén waves are transverse magnetic tension waves propagating along magnetic field lines (Finlay, 2007).

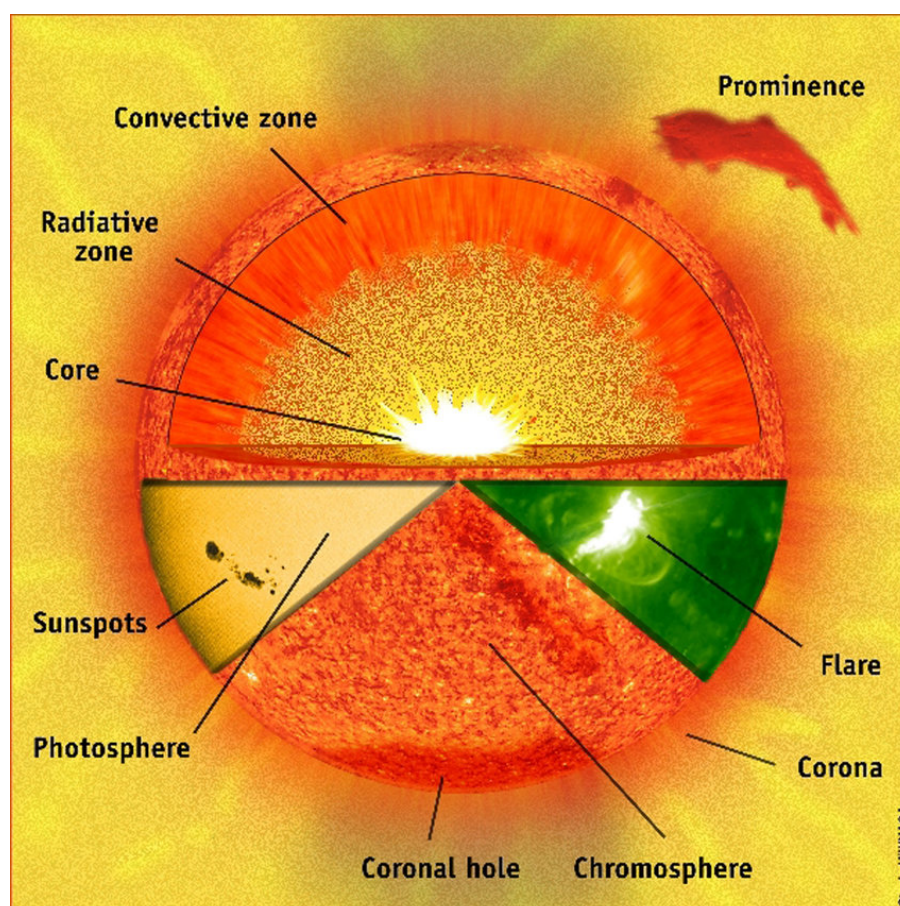


Figure 1.1: The internal structure of the Sun along with the solar atmosphere. Some of the basic solar activity features are also indicated using SOHO images of the Sun. Image Credit: ESA & NASA/ SOHO.

1.2.2 The solar magnetic field

The first evidence of solar magnetic field was found by G. Hale in the early twentieth century (Hale, 1908). Hale identified strong magnetic regions on the solar surface

using the technique of Zeeman spectral splitting. The magnetic field of all astronomical bodies are produced by a *hydromagnetic dynamo process* (Elsasser, 1956). Hence, the Sun's magnetic field is generated and sustained in its interior by a *solar dynamo* that is regulated by the dynamics of plasma inside the Sun. The Sun is a spherical blob of ionised plasma. The evolution of plasma as well as magnetic field follow the laws of Magnetohydrodynamics (MHD). Under ideal MHD, it is assumed that the plasma is an electrically conducting fluid. The MHD equations include the Navier-Stokes equation,

$$\frac{\rho \partial \mathbf{v}}{\partial t} + \rho(\mathbf{v} \cdot \nabla)\mathbf{v} = -\nabla p + \mathbf{J} \times \mathbf{B} + \rho \mathbf{g} + \nabla \cdot \boldsymbol{\tau}, \quad (1.1)$$

the magnetic induction equation,

$$\frac{\partial \mathbf{B}}{\partial t} = \nabla \times (\mathbf{v} \times \mathbf{B} - \eta \nabla \times \mathbf{B}), \quad (1.2)$$

mass continuity, energy equation and the equation corresponding to the solenoidal nature of magnetic field (i.e., $\nabla \cdot \mathbf{B} = 0$). In Equation 1.1 and 1.2, \mathbf{B} , \mathbf{v} , η , ρ , p , \mathbf{g} , \mathbf{J} and $\boldsymbol{\tau}$ represent magnetic field, large-scale velocity, magnetic diffusivity, plasma density, pressure, gravitational acceleration, current density and viscous stress tensor, respectively. The Navier-Stokes equation represents the evolution of velocity field in the presence of magnetic field. In case of static equilibrium, $\mathbf{v} = \text{constant}$ and $\frac{\partial}{\partial t} = 0$. Thus, Equation 1.1 becomes

$$-\nabla p + \mathbf{J} \times \mathbf{B} + \rho \mathbf{g} = 0. \quad (1.3)$$

If mechanical body forces such as gravity are negligible compared to the other forces, Equation 1.3 becomes

$$\mathbf{J} \times \mathbf{B} = \nabla p. \quad (1.4)$$

The magnetic field of Equation 1.4 is called as pressure-balanced field. If the plasma- β parameter represented by the ratio of gas pressure to magnetic pressure is much lower than unity in a plasma medium, the magnetic pressure dominates the gas pressure and the pressure gradient can not balance the magnetic stress. In this condition, magnetic field re-configures itself in such a way that the magnetic force vanishes. Thus, the magnetic force, i.e., Lorentz force becomes zero,

$$(\nabla \times \mathbf{B}) \times \mathbf{B} = 0. \quad (1.5)$$

The magnetic field when satisfies Equation 1.5 is called the force-free field. A linear solution of Equation 1.5 is

$$\nabla \times \mathbf{B} = \alpha \mathbf{B}, \quad (1.6)$$

where α is a constant. Equation 1.6 corresponds to nonpotential field. In some special cases where $\alpha = 0$, the Equation 1.5 becomes $\nabla \times \mathbf{B} = 0$ and characterises a potential field.

The induction equation (Equation 1.2) describes magnetic field evolution in the presence of large-scale velocity and magnetic diffusivity. Using the solenoidal property of magnetic field and assuming η to be independent of space, Equation 1.2 may be written as,

$$\frac{\partial \mathbf{B}}{\partial t} = \nabla \times (\mathbf{v} \times \mathbf{B}) + \eta \nabla^2 \mathbf{B}, \quad (1.7)$$

where the first and second terms of R.H.S are known as advective and diffusive terms, respectively. In astrophysical MHD, the ratio of these two terms denoted by magnetic Reynolds number $R_m = vL/\eta$ (L corresponds to the plasma length scale), is very large. As a large value of R_m implies a small η , Equation 1.8 can be simplified to

$$\frac{\partial \mathbf{B}}{\partial t} \sim \nabla \times (\mathbf{v} \times \mathbf{B}). \quad (1.8)$$

Equation 1.8 leads to the flux freezing theorem (Alfvén, 1942). This states that magnetic field is frozen into the plasma and magnetic fluids remain coupled in astrophysical system with high R_m . Inside the Sun, magnetic field exists in the form of flux tubes which are basically concentrations of magnetic field lines in plasma (Choudhuri, 2003). If a flux tube with average magnetic field intensity B_i , density ρ_i and pressure p_i is present at the base of the solar convection zone where the pressure and density outside the flux tube is represented by p_o and ρ_o , respectively, the tube rises up against gravity and emerges on the solar surface as a bipolar magnetic region, i.e., a sunspot. This is because in hydrostatic equilibrium, $p_o = B_i^2/8\pi + p_i$, which implies $p_o > p_i$. Considering the temperature inside the tube to be equal to that outside, the flux tube is unstable to buoyancy because of the condition $\rho_o > \rho_i$.

According to Larmor and Joseph (1919), the motion of electrically conducting ionised plasma in the convection zone maintains the solar magnetism. As the Sun is composed of hot and dense plasma, it rotates differentially with the equator

rotating faster (25 days/rotation) than the pole (33 days/rotation; Thompson et al., 1996). For illustrative purposes, let us assume that initially a large-scale north-south oriented poloidal magnetic field exists in the solar interior. Due to the differential rotation, the poloidal field is stretched out more toward the direction of rotation near the equator creating a toroidal field. The direction of the toroidal field is opposite in the two hemispheres. The toroidal magnetic field is stored and amplified at the tachocline where the magnetic buoyancy is suppressed, and a strong radial shear exists (Spiegel and Weiss, 1980; Van Ballegoijen, 1982). When very strong magnetic flux tubes come out of this stable layer to the convection zone, magnetic buoyancy forces make the magnetic loops erupt through the surface as bipolar sunspot pairs where the magnetic field is directed outward in one of the spots and inward in the other. As the underlying toroidal field has opposite direction in two hemispheres, bipolar sunspot pairs have opposite orientations in the northern and southern hemispheres. Due to the Coriolis force, the axis of the buoyantly rising flux tubes acquires a tilt, which roughly increases with increasing solar latitude (Joy's law; Hale et al., 1919). The trailing part of the tilted flux tube has an opposite magnetic polarity than the pole. The tilted sunspot pairs decay via diffusion and its flux is redistributed by meridional circulation (Nandy and Choudhuri, 2002). In this way, a net flux is carried to the polar region. It reverses the older polar field and builds up a new cycle poloidal field (Babcock, 1961; Leighton, 1969) that eventually leads to a global reconfiguration of the Sun's magnetic field. The poloidal and toroidal components of the magnetic field interchange between themselves in a about 11 years (Parker, 1955) which is defined as the time period of a sunspot cycle. During the purely dipolar configuration state, the sunspot cycle crosses through the solar minimum phase, whereas the toroidal field configuration state corresponds the solar maximum phase.

1.2.3 Solar activity

The Sun's magnetic field shapes and modulates solar activity. Due to magnetic buoyancy, the ' Ω '-shaped loops containing magnetised plasma rise up the photosphere. The footpoints of the loops called sunspots are concentrated magnetic field regions (magnetic field intensity is on the order of 1000 G) and are observed as

dark spots in white light. The spots appear dark because strong magnetic field inhibits the upward plasma motion and lowers the temperature. As the sunspots are the centers of solar magnetic activity, they are named as solar active regions (ARs). The magnetic fields of ARs are measured using photospheric magnetic maps – magnetograms. The magnetograms are generated utilizing Zeeman effect – the splitting of the energy levels of an atom in the presence of external magnetic field (e.g., Lagg et al., 2017). Depending on the size and magnetic flux content, the lifetime of an AR ranges from a few hours to several months. The level of activities of ARs is dependent on their magnetic properties like magnetic flux and nonpotentiality throughout their evolutionary stages, starting from their emergence to decay (Driel-Gesztelyi and Green, 2015). If ARs have a large store of nonpotential magnetic energy generated from the field lines which are strongly sheared relative to their minimum-energy (potential) configurations, they are susceptible to magnetic relaxation. Thus, the global nonpotentiality of ARs favor eruptive events from ARs (Moore, Hagyard, and Davis, 1987; Moore, 1987; Moore, 1988; Moore and Roumeliotis, 1992). In Figure 1.2, the monthly averages (blue curve) and 13 months smoothed (red curve) sunspot numbers are plotted as a function of time. The magnetograms show AR distributions during solar minimum (Figure 1.2I.) and maximum (Figure 1.2II.). The black and white patches on the magnetogram denote the negative and positive polarities of the magnetic field, respectively.

A flux tube rising above the photosphere encounters the chromosphere where the emission line spectrum dominates. In $H\alpha$ (one of the strongest emission lines of the chromospheric spectrum), ARs look brighter than quiet regions. A dark structure of cool, dense material called filament is suspended against gravity by magnetic tension at this layer. One of the major features observed in the chromosphere are filaments. At the solar limb, the filaments appear bright against the dark background and are called prominences. In Figure 1.1, an example of a solar prominence is shown. The lifespan of a filament may vary from several days to a few months. Depending on the location, the filaments are subdivided into quiescent, intermediate, and active region filaments (Engvold, 2015). Filaments may erupt due to instability or disappear by draining their mass toward the chromosphere. Generally, the active region filaments appear above polarity inversion lines (PIL) separating opposite polarity magnetic

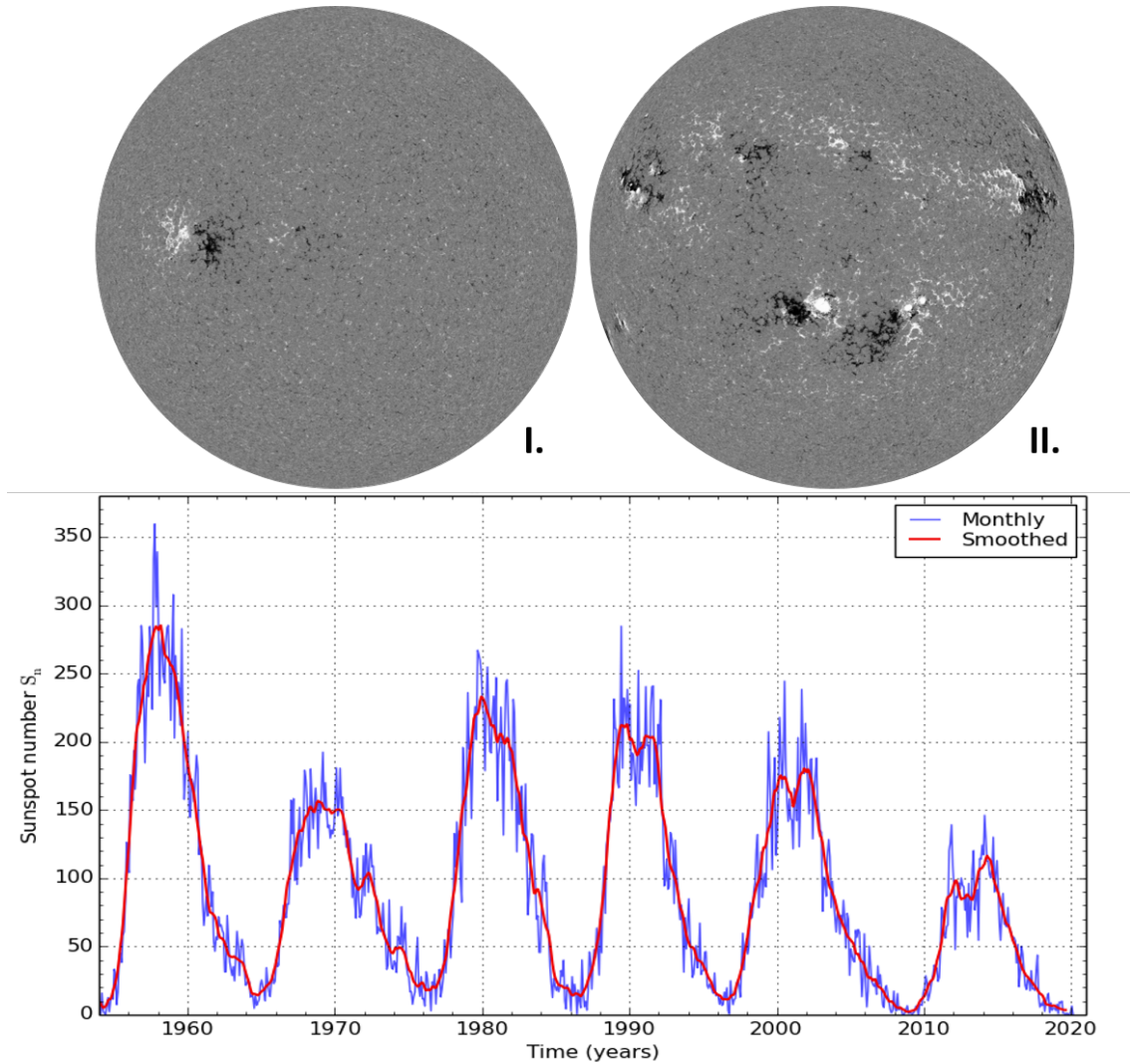


Figure 1.2: Averaged sunspot number (S_n) plotted as a function of time along with examples of AR distribution on photospheric magnetic maps during I. solar minimum and II. solar maximum periods. Image credit: SILSO data/image, Royal Observatory of Belgium, Brussels and SDO/HMI.

field regions of the Sun.

A flux tube extending above the chromosphere reaches the outer atmosphere of the Sun – corona. The corona is roughly divided into lower (region close to the chromosphere), middle (extends up to few solar radii), and upper (ranges up to tens of solar radii) regions. The middle corona is observed naturally during a solar eclipse as well as using an artificial occulter of the solar disk termed as a coronagraph (Lyot, 1939). At the solar corona, the flux tubes associated with ARs appear as bright and dynamic structures known as coronal loops (e.g., Reale, 2014).

They are observed in extreme ultra-violet (EUV) wavelengths. Sometimes, a cap-like coronal structure with long pointed peaks is observed using a coronagraph. Such structures are called helmet streamers (e.g., Wang et al., 2000). Another important feature of the solar corona is the coronal hole (e.g., Cranmer, 2009) often found at the Sun's pole during solar minimum. Coronal holes are regions of open magnetic field lines that appear dark in EUV wavelengths. Corona is the source of solar wind – a constant stream of charged particles flowing out from the Sun to interplanetary space (Parker, 1958; Biermann, 1965). As the corona is very hot, the Sun's gravity can not prevent the charged particles from escaping continuously. The solar wind particles carry energies of ~ 1 KeV and are observed in two states, slow and fast. The slow solar wind has a typical speeds of 300-400 km/s and is believed to be related to the streamer belt regions (e.g., McComas et al., 2008). During low solar activity, it is concentrated near the solar equatorial plane and when activity increases, it extends up to higher latitudes (Saez et al., 2005). The fast solar wind has a speed of 700-800 km/s and originates from coronal holes (Zirker, 1977). The density of fast solar wind particles is less than that of the slow wind.

The magnetic pressure dominates the gas pressure at the solar corona, and the coronal magnetic field is frozen in to the plasma flow. In the presence of pressure gradient, the Sun's magnetic field is carried out with the solar wind plasma to the heliosphere and form the interplanetary magnetic field (IMF; Owens and Forsyth, 2013). Although the plasma motion is radial, the IMF forms a spiral configuration because the footpoints of IMFs remain rooted in the rotating solar surface. The spiral pattern of IMF is known as the Parker spiral (Parker, 1958). Figure 1.3 illustrates the Parker spiral configuration. The angle between the radial and IMF direction increases with the increasing distance from the Sun. At Earth, this angle takes a value of about 45° .

1.3 Coronal mass ejections (CMEs) as a space weather driver

Transient disturbances in the solar wind drive space weather. These mainly originate from the Sun's magnetised plasma on very different temporal and spatial

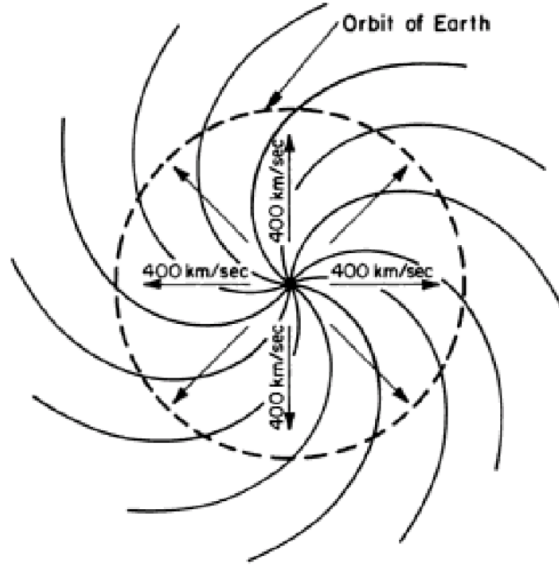


Figure 1.3: Schematic explaining the IMF's Parker spiral structure. The black curves show IMF field lines, whereas the black arrows indicate the solar wind plasma flow directions, reproduced from Hundhausen (1995).

scales. The important sources of space weather are coronal mass ejections (CMEs; Webb and Howard, 2012) which inject large quantities of magnetised plasma into the heliosphere solar energetic particles (SEPs; Klein and Dalla, 2017) like electrons, protons and high-energy nuclei originating from solar flares, CME-driven interplanetary shocks, and stream interaction regions (SIR; Richardson, 2018) arising from interaction of high-speed solar wind with the preceding slow solar wind. Of them, CMEs drive the most extreme space weather effects on Earth and throughout the heliosphere (Schwenn, 1986; Tsurutani et al., 1988; Gosling, 1993; Zhang et al., 2007; Green and Baker, 2015).

CMEs involve an expulsion of large amounts of magnetised plasma at high velocities from the solar corona into the solar wind and are believed to be responsible for accelerating coronal ions to high energies. They are important not only from the solar physics viewpoint but also for their significant role in studies of solar-terrestrial relationships. In the corona, CMEs are observed using coronagraphs. In the interplanetary medium, they are identified using solar wind plasma parameters and magnetic field measured in situ by spacecrafts. An example of a CME is shown in Figure 1.4. It is observed by the Large Angle and Spectrometric Coronagraph

(LASCO) on board the *Solar and Heliospheric Observatory* (SOHO). The importance of studying CMEs lies in space weather forecasting that requires appropriate knowledge of CME initiation from the Sun, CME properties, and their evolution through interplanetary space.

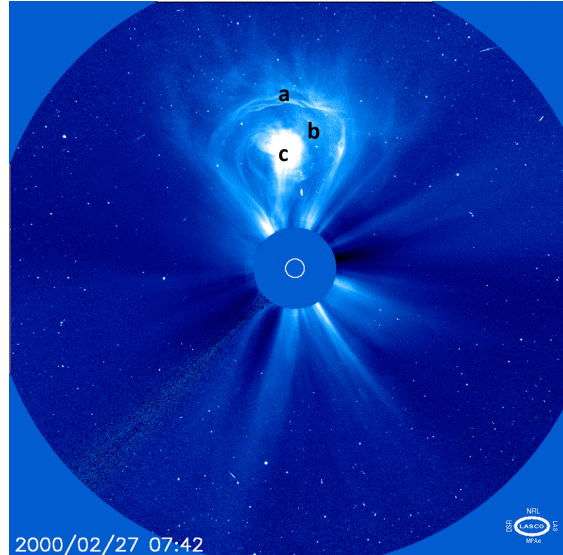


Figure 1.4: Observation of a CME using a white-light coronagraph. Credit: SOHO/LASCO. The indicated regions are a) bright-front, b) cavity, and c) core. of the CME’s three-part structure.

1.3.1 CME initiation mechanisms

A stable coronal field structure involves a balance of forces as expressed in Equation 1.4. The onset of CMEs needs a triggering mechanism that generates instability in the magnetic structures and requires a source of energy for the early evolution of CMEs. As CMEs are coronal phenomena, the energies responsible for their early acceleration are believed to be available in the solar corona. This energy is predominantly provided by the stressed and sheared magnetic field since magnetic pressure dominates the gas pressure in the solar corona.

One of the significant factors that leads to the generation of instability is magnetic reconnection (Mozer and Pritchett, 2010). Due to this, a rapid transfer of energy from the magnetic field to the surrounding plasma occurs. Reconnection occurs at a region where oppositely directed magnetic fields are present (Vasyliu-

nas, 1975) and an X-type neutral point is formed as shown in Figure 1.5. At this region called “diffusion region”, a current sheet is formed due to the presence of electric fields directed perpendicular to the two dimensional plane of the plasma flows (i.e., perpendicular to the plane of the image in Figure 1.5). The plasma flows across the field lines from either side of the diffusion region and channelled into the outflow regions along the neutral line. The reconnection results in a dissipative process that converts magnetic energy to kinetic energy. The kinetic energy accelerates particles out of the diffusion region. In Figure 1.5, we demonstrate a basic configuration of two-dimensional steady-state magnetic reconnection that follows the Sweet-Parker reconnection model (Sweet, 1958; Parker, 1963). The plasma flow velocity \mathbf{V} and magnetic field vector \mathbf{B} is in the x - y plane. The v_1, v_2 are inflow and outflow plasma velocities, and B_1, B_2 are magnetic field intensity of inflowing and outflowing regions, respectively. The symbols Δ and δ indicate the inflow and outflow length-scales. The length of the current sheet in this reconnection model is same as the scale size of the global field. The rate of Sweet-Parker reconnection is much slower than the rate required to release magnetic energy in solar eruptive events like solar flare and CMEs. Petschek (1964) proposed a reconnection model in which the reconnection rate is much faster than that of Sweet-Parker model. In Petschek configuration (Vasyliunas, 1975; Priest and Forbes, 2000), the length of the diffusion region current sheet is much shorter than that of Sweet-Parker model and the conversion of magnetic energy in the form of heat and kinetic energy occurs at the standing slow-mode shocks attached to the corners of the diffusion region.

CME initiation triggered by magnetic reconnection

Several models advocate magnetic reconnection as an initiation mechanism of CMEs (Antiochos, DeVore, and Klimchuk, 1999). If the core magnetic field becomes strongly sheared and runs nearly parallel to the polarity inversion line in the presence of the less-sheared overlying fields it can rise up because of the imbalance between the pressure force of sheared magnetic field and the tension from the overlying fields. A current sheet is formed beneath the core magnetic field between the oppositely directed stretched legs of the overlying field lines and magnetic reconnection takes place. The reconnection allows the core field to penetrate the

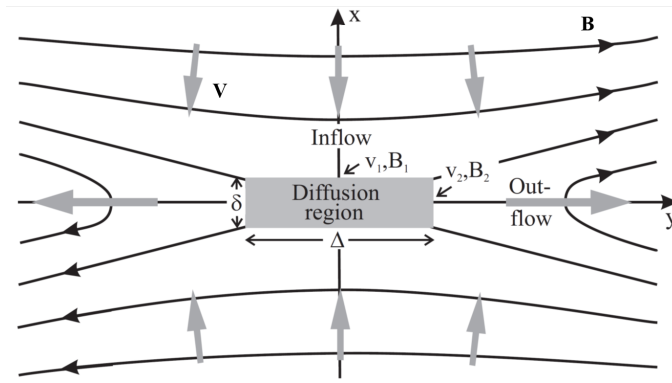


Figure 1.5: A basic two dimensional configuration of magnetic reconnection driven by two oppositely directed inflows along x -direction. The outflows are created along y -direction. The diffusion region is shown using a grey box where plasma- $\beta > 1$ (Schindler and Hornig, 2000)

overlying field lines. The erupting core stretches the remaining overlying field lines and excites magnetic reconnection that provides more energy to the eruption. This process is well-known as the *Tether Cutting* process (Sturrock, 1989). It can result in magnetic configurations like post-eruption arcades and flare ribbon structures which have been confirmed by observations (Falconer, 2001; Hagyard et al., 1984). According to Antiochos, Burch, and Carovillano (1999), the problem with Tether Cutting is that it can not provide sufficient energy required to initiate a CME even though magnetic reconnection plays a crucial role. As an alternative to this process, a model called the *Breakout* model was introduced (Antiochos, DeVore, and Klimchuk, 1999) that relies on magnetic reconnection to occur between a sheared arcade and nearby magnetic field structures during an eruption. The model assumes that the CME takes a form of closed plasmoid originating from an existing field structure. The plasmoid breaks off the coronal fields with energy acquired from magnetic reconnection with the surrounding fields. Also, the overlying fields are pushed aside by reconnection during the initiation process. Figure 1.6I and II show schematic diagrams of the Tether Cutting and Breakout models including each of their phases. The instabilities leading to eruption may originate from reasons other than magnetic reconnection as well.

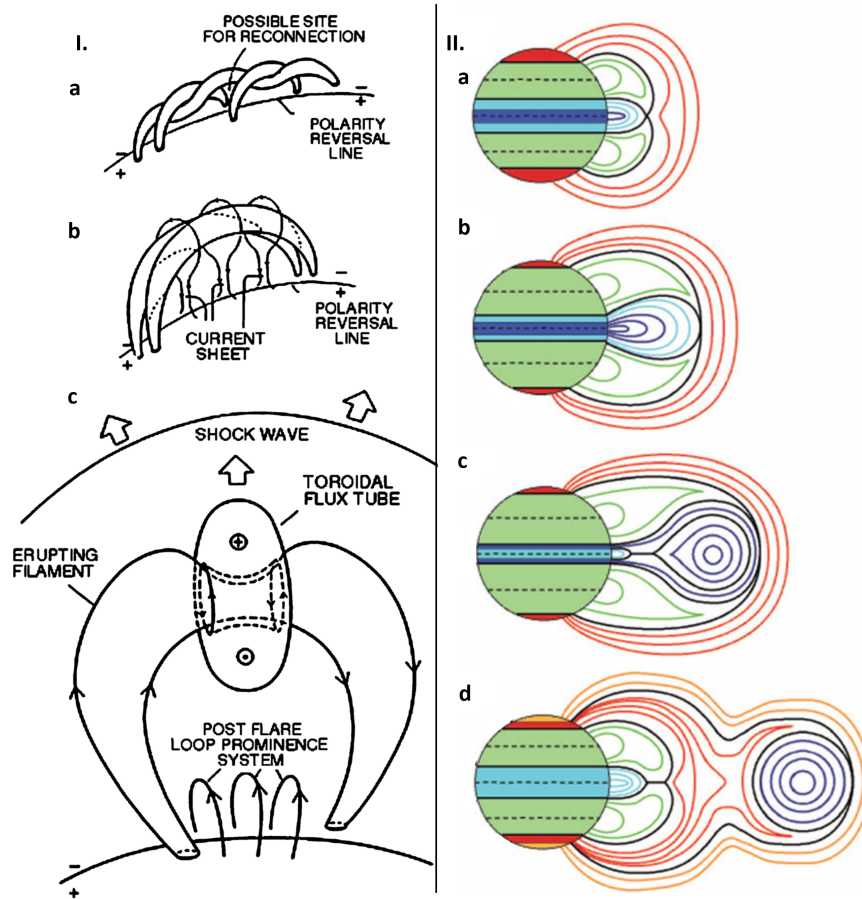


Figure 1.6: I. A diagram representing the Tether Cutting model with a) a configuration showing pre-launch magnetic field with prominence structure followed by the b) magnetic field evolution to allow magnetic reconnection, and c) eruption of flux rope (Sturrock, 1989). II. The four stages of Breakout model showing a) the initial configuration, b) shearing of field lines, c) starting of reconnection at the shear channel, d) separation of the plasmoid from the main configuration due to reconnection (Lynch et al., 2008).

Onset of CMEs without magnetic reconnection

Due to photospheric motions including shearing, rotational and granulation flow, the flux rope footpoints are stressed, sheared, and twisted (kinked). Thus, the flux rope forms helical (projected S-shaped) sigmoid structures. As the twist increases magnetic tension, the flux rope loses its equilibrium and becomes vulnerable to *Kink instability*. This further produces a disturbance to the magnetic field, leading to expulsion of CMEs (Török and Kliem, 2003). In Figure 1.7, an eruption of a

kink-unstable flux rope is shown using snapshots of a kink instability simulation performed by Török and Kliem (2005). Also, the magnetic flux injected from the photosphere to a flux rope may enhance the flux rope’s toroidal current giving rise to a significant Lorentz force ($\mathbf{J} \times \mathbf{B}$). The flux rope attains initial acceleration from a large twist over a small timescale and can be driven by the Lorentz force away from the Sun. This phenomenon is known as *Toroidal instability* [also called a *Flux injection model* (Chen, 1989)]. In this model, the energy required to launch CMEs arises from the photosphere, although no evidence of energetic surge from the photosphere is observed.

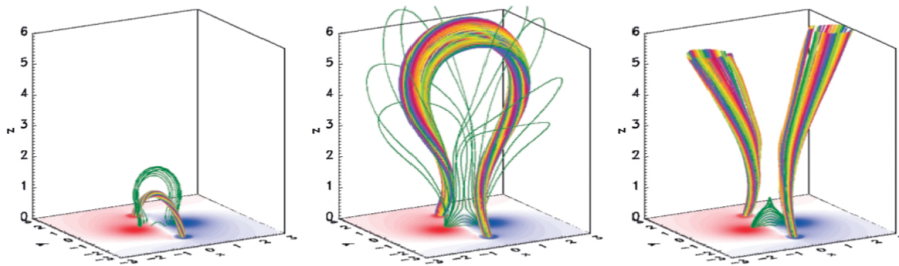


Figure 1.7: Simulation of a kink-unstable flux-rope eruption (Török and Kliem, 2005).

1.3.2 Signatures of CME initiation

Coronal observations of the triggering mechanisms responsible for the onset of CMEs are difficult. Only near-solar-surface phenomena are identified as associated with the CME initiations. These phenomena are observed using the electromagnetic spectrum specifically EUV and H- α imagers. In this section, we briefly discuss few of them.

Solar flare

In 1973, when CMEs were first discovered, it was believed to be a flare-driven phenomenon. Later, several studies (Gosling, 1993; Hudson, Haisch, and Strong, 1995) established that CMEs are a completely separate phenomenon often associated with flares. It is accepted that both CMEs and flares belong to a single magnetically-driven event. A standard flare model (Švestka and Cliver, 1992; Shibata et al., 1995; Lin, 2004) has been developed to explain such a magnetically-driven event.

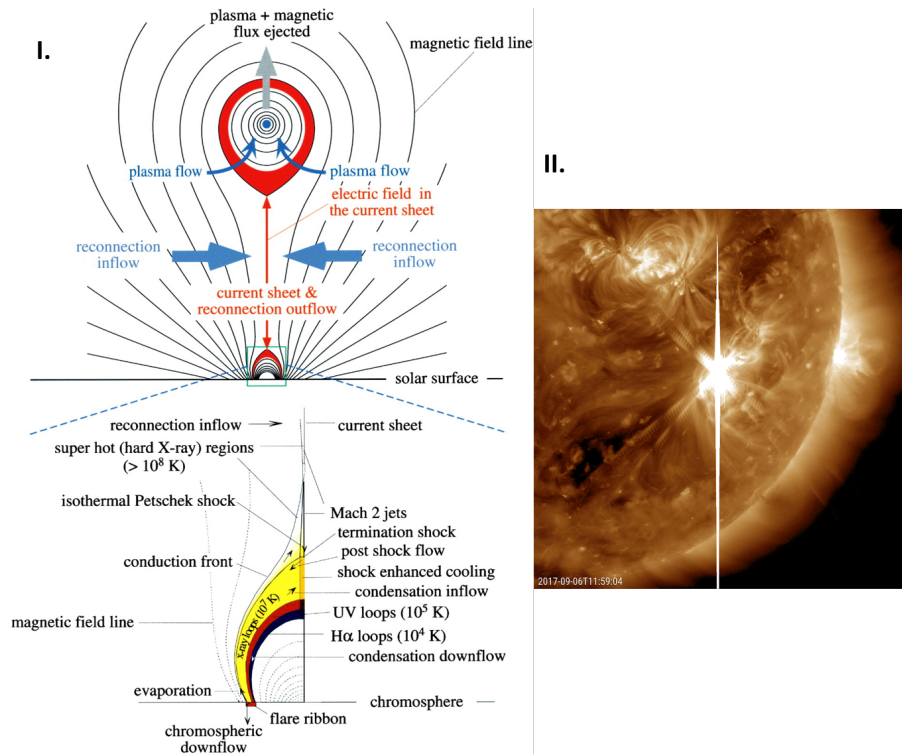


Figure 1.8: I. Schematic showing an eruptive process involving magnetic reconnection leading to both CME and flare. The different colors are used to indicate the different temperatures of plasma. The diagram corresponds to the two-ribbon flare configuration (Forbes and Acton, 1996). II. An observation of a solar flare in EUV wavelength. Credit: SDO/AIA

When an external pressure brings oppositely directed magnetic field lines closer beneath a sheared magnetic arcade, the field lines converge and involve reconnection. Some of the energies generated due to this process heat up the plasma, add mass and magnetic flux to the flux rope inside the arcade. The remaining energy flows downward in the form of a shock, the energetic particles heat up the low-lying reconnected loops, and produce flares. This phenomenon is demonstrated using a schematic (Lin, 2004) shown in Figure 1.8 along with an observed flare in EUV wavelength. The most energetic fast CMEs tend to be associated with bright flares (e.g., Webb, 2002; Gopalswamy, Yashiro, and Akiyama, 2007). Sheeley et al. (1983) showed that CME's association with flares increases linearly with the flare duration. Flares release energy in the forms of electromagnetic rays, energetic particles, and plasma flows. Based on the intensity of flares in X-rays, it can be classified as 'X',

‘M’, ‘C’, ‘B’ and ‘A’-class depending on its intensity in Watt/m² unit.

Erupting prominence

Several studies explore an association of erupting prominences (disappearing filaments) with CMEs (Munro et al., 1979; Sinha, Srivastava, and Nandy, 2019). Due to the presence of overlying magnetic structures, the magnetic field in a prominence material is confined near the solar surface. If the overlying fields are destabilized and result in an eruption of a CME, the prominence can also erupt along with the CME. Figure 1.9a shows a fragment of an erupting prominence associated with a CME eruption at the North-East side of the solar limb in a EUV difference image of the Sun.

Post-eruption arcade or Post-flare loops

Post-eruption arcades (PEAs; Tripathi, Bothmer, and Cremades, 2004) are bright structures observed using EUV wavelengths in the low-coronal region. This structure is formed occasionally following the launch of a CME due to magnetic reconnection. When reconnection triggers a CME upward, it compresses the reconnected field lines towards the Sun in an arcade form. Tripathi, Bothmer, and Cremades (2004) found remarkable associations between PEAs and CME footpoints. Figure 1.9b shows an example of a PEA associated with the Bastille Day CME that occurred on 14 July 2000.

Coronal dimming

Coronal dimming (Sterling and Hudson, 1997) represents the removal of coronal mass that follows the launch of a CME and lasts for several hours. Several studies on coronal dimming using observations in X-rays (Rust and Hildner, 1976), EUV (Thompson et al., 2000), and H- α (Jiang et al., 2003) led to the conclusion that dimming occurs due to the reduction of density and not because of change in temperature. As the structure of dimming matches well with that of CME, dimming appears to be one of the best indicators of the projection of CMEs on the solar surface (Reinard and Biesecker, 2008). A study by Mandrini et al. (2007) suggests

that dimming marks the footpoints of CME flux ropes. An example of a CME associated dimming region is shown in Figure 1.9a.

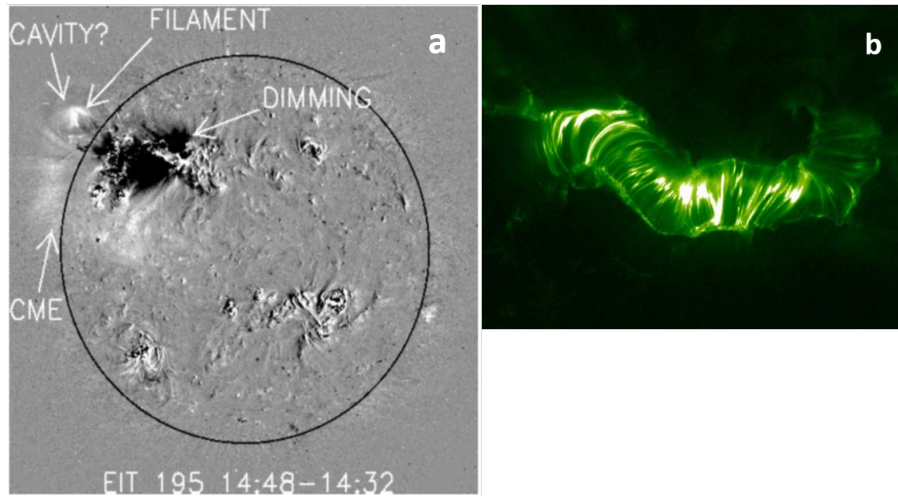


Figure 1.9: a) An EUV difference image of the Sun showing an example of an eruptive prominence and dimming region associated with a CME (Gopalswamy and Thompson, 2000). b) A post-eruption-arcade formed during the Bastille Day CME on July 14, 2000 (Schwenn et al., 2006)

1.3.3 Several properties of CMEs

The basic characteristic of CMEs are their source locations on the solar disk, velocities, energies, angular widths, occurrence rates, masses and magnetic structure (St. Cyr et al., 2000; Webb, 2002). Generally, the measurements of the basic properties are done on the plane of the sky (a plane orthogonal to the Sun-Earth line). Therefore, if a CME is not located at the solar limb, estimates of its properties are compromised. By utilizing auxiliary data and multiple viewpoint capabilities (e.g., Mierla et al., 2010), this problem has been reasonably solved. Below we summarise current knowledge of the structures and basic properties of CMEs.

Morphology

The white-light images of the solar corona record the photospheric radiation scattered by electrons present in ionised plasma. Thus, the diagnosis of coronal plasma density is independent of other physical characteristics like the temperature of the

plasma. In white-light images, CMEs exhibit a variety of forms, including a three-part structure, narrow jets, and streamer blowouts (such kind of CMEs arise from pre-existing coronal streamers). Among these, the most important morphological pattern is the three-part structure (Illing and Hundhausen, 1985; Hundhausen, 1999). This structure consists of a bright front – a shell of dense coronal plasma surrounding a dark region and associated with overlying fields swept up by erupting flux ropes, cavity – a region associated with flux rope, and the core that represents the cooler plasma usually associated with bright prominence material. The CME shown in Figure 1.4 shows a three-part structure.

Location, size, and occurrence rate

During solar minimum, CMEs appear near the solar equator but at solar maximum, the sources of CMEs may extend up to 60 degree solar North and South (St. Cyr et al., 2000; Yashiro et al., 2004). Hundhausen (1993) noted that CMEs originating from high latitude regions correspond to large structures like prominence and streamers instead of ARs and flares.

As observed in plane-of-sky, the distribution of CME angular size varies over the solar cycle and peaks at about 40° (Hundhausen, 1993). CMEs having angular width of 360° appear as bright circular structures surrounding a coronagraph. These are called halo CMEs. The solar sources of halo CMEs are typically located within a few tens of degrees of the Sun's center from an observer's perspective (Webb, 2002). There are claims that these CMEs are faster as well as more energetic than the non-halo CMEs (Gopalswamy et al., 2010). The average CME mass is about 1.4×10^{12} kg (Vourlidas et al., 2002). A CME with larger mass can reach a greater height (Webb and Howard, 2012).

The rate of CME occurrence typically follows a solar cycle in phase and amplitude (Webb and Howard, 1994). In Figure 1.10a, the variation of CME occurrence rate averaged over Carrington rotations during 1996-2011 has been shown. It is noted that the rate varies from around one per day at solar minimum to about five per day during solar maximum (St. Cyr et al., 2000).

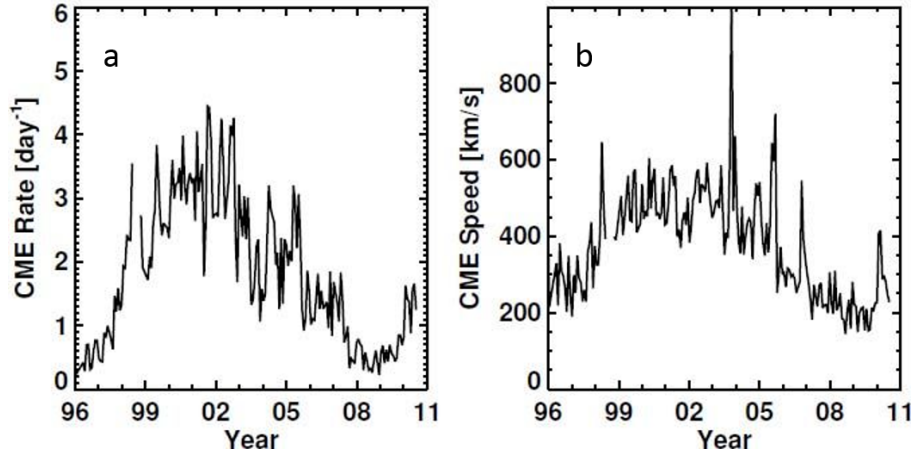


Figure 1.10: a) CME occurrence rate, and b) speed averaged over Carrington rotations during 1996-2011. Due to highly energetic CMEs appear during late 2003 a large spike is present in CME speed. The image is adapted from Gopalswamy (2010)

Kinematics

The distribution of the plane-of-sky speed of CMEs ranges from 20 km/s to more than 2500 km/s with a peak value of about 350 km/s (Hundhausen, 1999). According to Sheeley et al. (1999), CMEs are of two types: gradual CMEs and fast CMEs. Gradual CMEs are associated with prominences and their speed ranges from 400-600 km/s. On the other hand, the fast CMEs are related to flares and their speeds are usually more than 750 km/s. Figure 1.10b shows the speed of CMEs averaged over Carrington rotations during 1996-2011. The mean speed of CMEs peaks during solar maximum and early declining phase of a solar cycle (Gopalswamy, 2004). After $2 R_{\odot}$, the speed of a typical CME becomes constant although the slowest CMEs accelerate and the fastest tend to decelerate due to interaction with the solar wind (St. Cyr et al., 2000; Yashiro et al., 2004). Generally, the intrinsic acceleration of a CME occurs close to the Sun, within $1.5 R_{\odot}$ (Jing et al., 2005). As the plane-of-sky measurements of CME properties are subject to projection effect, several geometrical techniques for determining three dimensional deprojected information are devised (Howard, Nandy, and Koepke, 2008). Such techniques include tie-pointing (e.g., Mierla et al., 2009), forward modeling (e.g., Thernisien, Howard, and Vourlidas, 2006), and inverse reconstruction (Antunes, Thernisien, and Yahil, 2009).

Estimations of CME energy are necessary for understanding their kinematics and dynamics. While CMEs progress through the outer corona, their energy can be segregated into potential, kinetic and magnetic energy. It is observed that at the outer corona, unlike fast CMEs, slow CMEs have higher potential energy than kinetic energy (Vourlidas et al., 2000). Vourlidas et al. (2000) demonstrated that CMEs are magnetically driven phenomena. The study showed that when CMEs move out from the outer corona, their potential and kinetic energy increase at the expense of their magnetic energy. Thus, the total energy stays roughly constant. As magnetic energy primarily drives CMEs, the magnetic properties of CMEs are important to understand.

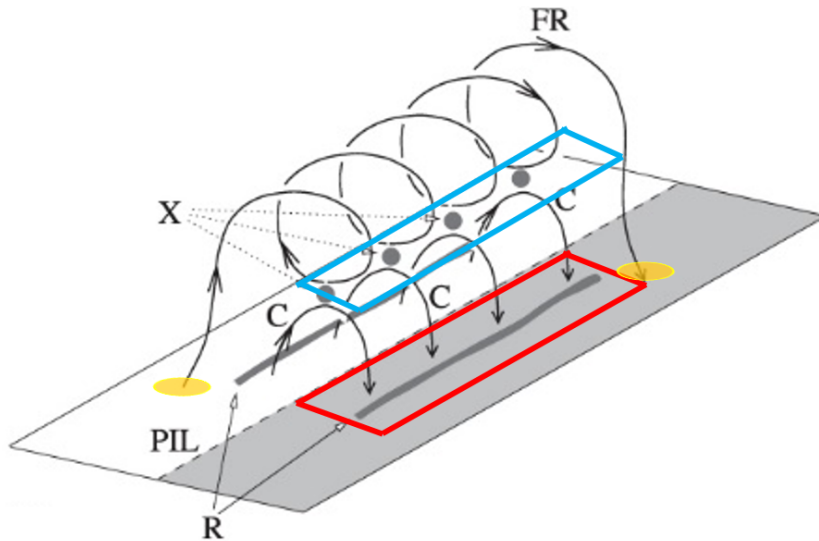


Figure 1.11: A schematic of the two ribbon flare model in three dimensions (Longcope and Beveridge, 2007) with possible reconnection region enclosed by red curve and dimming region indicated by yellow circle. The flux associated with the reconnection area is equivalent to the poloidal flux of the twisted flux rope (FR) measured using poloidal field lines perpendicular to the plane enclosed by the blue curve. The dimming region associated flux corresponds to the toroidal flux of the FR. The ribbons are indicated by ‘R’, the polarity inversion line (PIL) is shown by a dashed line, and the reconnection sites and arcades are denoted by ‘X’ and ‘C’, respectively.

Magnetic properties of CMEs

As Zeeman splitting measurements are compromised in solar corona due to thermal broadening, it is hard to directly observe the magnetic field in near-Sun CME flux ropes. Mouschovias and Poland (1978) first applied a flux-rope model to CMEs and estimated their geometrical and magnetic properties. Thereafter, several studies have modeled CMEs using three-dimensional flux ropes and the results are found to be responsible (Gibson and Low, 1998; Krall and Cyr, 2006b). Thernisien (2011) introduced a forward model known as Graduated Cylindrical Shell (GCS) model that uses multiple views of CMEs. If a CME is assumed to be a cylindrical flux rope and formed because of magnetic reconnection process, its poloidal flux is equivalent to the associated reconnection flux (Longcope and Beveridge, 2007; Longcope et al., 2007; Priest and Longcope, 2017). Furthermore, Webb et al. (2000) suggested that the magnetic flux at the dimming regions associated with CME source locations is comparable to the toroidal flux of CME flux ropes. Figure 1.11 shows the correspondence between reconnection flux and poloidal flux, CME-footpoint associated dimming flux and toroidal flux. The topological properties of magnetic field lines are quantified by magnetic helicity (Berger, 1999). Various geometrical forms such as linking, twisting, and kinking contribute to magnetic helicity associated dynamics. If magnetic field lines do not change their topology by processes like magnetic reconnection, the helicity remains constant. Thus, for ideal MHD, magnetic helicity is a conserved quantity (Woltjer, 1958). CMEs carry away a part of the Sun's magnetic helicity into interplanetary space (Rust and Kumar, 1996).

The magnetic helicity (H) in a volume V is defined by $\int_V \mathbf{A} \cdot \mathbf{B} dV$, where \mathbf{A} is the vector potential and \mathbf{B} is the magnetic field with $\mathbf{B} = \nabla \times \mathbf{A}$. The Helicity is conserved and gauge-invariant in ideal MHD if the volume V is bounded by a surface S on which $\mathbf{B} \cdot \hat{n}|_S = 0$. As coronal magnetic fields are not bounded by magnetic surfaces, it is difficult to apply helicity conservation argument to coronal fields. The magnetic field lines enter the corona through the photosphere. To reveal the linkage structure of coronal field lines, the knowledge of magnetic field structure underneath the photosphere is necessary. Berger (1984) proposed the concept of relative helicity to derive the helicity of coronal field lines. The relative helicity (H_r) is the difference between the helicity of the entire volume under consideration

(H_c) and a reference field (H_p) obtained by replacing the coronal field with the corresponding potential field which has the same normal magnetic field ($\mathbf{B} \cdot \hat{n}|_s$) at the boundary surface of the volume. Thus, the relative helicity, i.e., $H_r = H_c - H_p$ becomes independent of magnetic field structure beneath the photosphere. Berger (1999) defined the coronal magnetic field $\mathbf{B}_c = \mathbf{B}_{cl} + \mathbf{B}_p$, where \mathbf{B}_p is a potential field satisfying $\nabla \times \mathbf{B}_p = 0$ and associated with the vector potential \mathbf{A}_p . The closed field (Kusano, Suzuki, and Nishikawa, 1995), \mathbf{B}_{cl} is related to the vector potential \mathbf{A}_{cl} . In this case, $\mathbf{B}_{cl} \cdot \hat{n}|_s = 0$ and $\mathbf{B}_p \cdot \hat{n}|_s = \mathbf{B}_c \cdot \hat{n}|_s$. The study derives the helicity of the coronal field by summing up the self-helicities and mutual helicity of \mathbf{B}_{cl} and \mathbf{B}_p . In the solar corona, the helicity of CME flux ropes with cylindrical symmetry can be obtained following a similar procedure.

1.3.4 Interplanetary manifestations of CMEs

During transition through interplanetary space, CMEs gradually expand and decelerate or accelerate depending on the difference in velocities of CMEs and ambient solar wind. A study by Reiner et al. (2003) provides evidence of constant deceleration of a fast CME during its Sun-Earth propagation. In the interplanetary medium, aerodynamic drag is considered to govern CME dynamics. At high Reynolds number, vortices are shedded downstream and formed in the trailing edges of rigid bodies (Batchelor, 1967). Thus, the moving bodies transfer momentum and energy to the surrounding fluid, and experience a retarding force, i.e., the drag force (F_d). The force F_d exerted on a moving body is regulated by a number of parameters like the body's cross-sectional area, intrinsic velocity with respect to the velocity of the external fluid, and density of the surrounding fluid. The observed acceleration/deceleration of some of the CMEs has been reproduced by only using the drag force that acts between the CME and ambient solar wind (Cargill, 2004; Vrřnak et al., 2010; Borgazzi et al., 2009). Gopalswamy et al. (2001) and Sachdeva et al. (2015) introduced an empirical model of CME's acceleration that is analogous to the drag acceleration, $a = -\gamma(V_{CME} - V_{sw})|V_{CME} - V_{sw}|$ (e.g., Cargill et al., 1996; Cargill, 2004; Vrřnak et al., 2010; Vrřnak et al., 2013). Here, V_{CME} and V_{sw} are velocities of CME and solar wind, respectively. The drag parameter γ is expressed as $\gamma = \frac{c_d A \rho_w}{V(\rho + \rho_w/2)}$, where c_d , ρ_w , ρ , V and A are the dimensionless drag coefficient,

ambient solar wind density, CME density, its volume and cross-sectional area, respectively. When a CME propagates, it expands in order to maintain a pressure balance with the surrounding solar wind. Several studies have noted that a CME expansion occurs in a self-similar manner, i.e., the ratio of minor to the major radius of CMEs remains constant with time while propagating through the interplanetary medium (e.g., Poomvises, Zhang, and Olmedo, 2010; Subramanian et al., 2014). However, MHD simulations of interplanetary propagation of CMEs demonstrate that sometimes CMEs are significantly distorted by the time they reach the Earth (Riley and Crooker, 2004).

Signatures of ICMEs

Over the years, space-based instruments probing the solar wind have identified interplanetary CMEs (ICMEs) by noting the deviations from the solar wind's ambient configuration. A comprehensive review of all in situ ICME signatures is provided in Zurbuchen and Richardson (2006). Some of the widely observed signatures are,

- a smooth rotating magnetic field vector with enhanced magnetic field intensity,
- low value of plasma- β that indicates the magnetically dominated dynamics that drives the motion of plasma,
- presence of bi-directional or counter-streaming hot electrons that indicates a closed magnetic configuration with footpoints rooted at the photosphere,
- a depression in proton and electron temperature because of the presence of frozen in flux,
- an enhancement in the Helium to Hydrogen composition ratio, and
- negative velocity slope representing the expansion of ICMEs.

ICME shocks and sheath regions

If an ICME propagates through the heliosphere with a speed much greater than the ambient solar wind speed, a shock front will form. More specifically, to form a

shock, the difference in speed between ICME and local solar wind should be more than the local magnetosonic speed (e.g., Blanco-Cano et al., 2016). About 50% of ICMEs involve shock formation (Marsden et al., 1987).

Behind an ICME shock, a region of compressed solar wind is found. The region is called a sheath region and formed due to the draping of solar wind field lines around the ICME front (McComas et al., 1989). Therefore, a sheath region is likely to have a north-south directed magnetic field component. Figure 1.12 shows a schematic of shock and sheath regions in front of an interplanetary CME plasma body along with their corresponding plasma and magnetic field parameters observed in situ at the Lagrangian point L1.

Magnetic clouds (MCs)

Although CMEs mostly appear as flux ropes in near-Sun observations, not all ICMEs show flux rope characteristics in the near-Earth in situ observations (e.g., Gosling, 1990; Richardson and Cane, 2004). The flux-rope ICMEs are known as magnetic clouds (MCs; Burlaga et al., 1981) which are identified by three particular signatures – an enhanced strength of magnetic field, a smooth rotation in magnetic field vectors, and a low proton temperature. In Figure 1.12II, the solar wind magnetic and plasma parameters during an MC passage are shown. The MC interval is indicated in orange. About one-third of the total observed ICMEs show clear flux-rope structures at 1 AU (e.g., Gosling, 1990; Cane and Richardson, 2003). One of the smooth rotating field vectors that changes its sign due to rotation represents the helical field, while the other component that does not change its sign during rotation represents the axial field of MCs. Inside an MC, the angle between the helical field lines and axial field, i.e., pitch angle, increases from the MC center to its edges (as shown in Figure 1.13I).

The MCs can be considered as force-free magnetic structures because the convective term ($\rho \mathbf{v} \cdot \nabla \mathbf{v}$) and the pressure gradient (∇p) of the momentum equation $\rho \mathbf{v} \cdot \nabla \mathbf{v} = -\nabla p + \mathbf{J} \times \mathbf{B}$ (in a frame moving with MC that is considered to be time-independent) can be neglected in first approximation (Goldstein, 1983). Here, \mathbf{v} is the flowing speed, c is the speed of light, \mathbf{J} represents the electric current density, and \mathbf{B} is the magnetic field vector of MCs. The force-free configuration

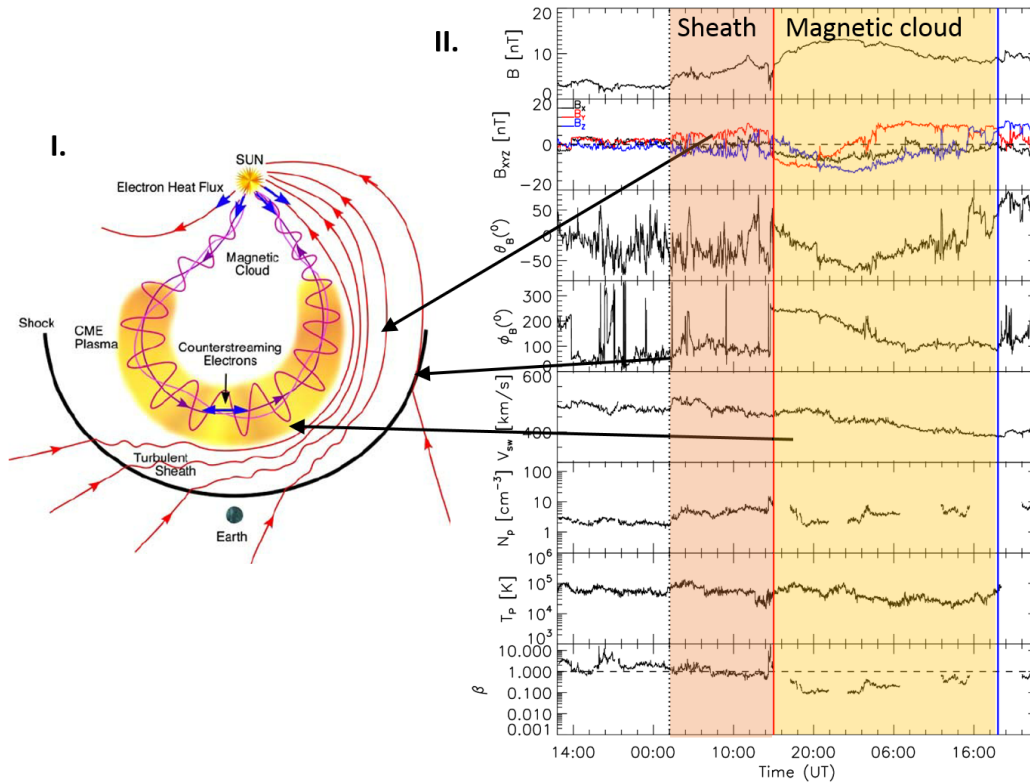


Figure 1.12: I. A schematic showing shock (black arc) and sheath (red curves) regions in front of an ICME plasma. Blue arrows show paths of counter-streaming electrons (Zurbuchen and Richardson, 2006). II. The solar wind plasma and magnetic field parameters associated with the shock, sheath, and ICME plasma observed at the Lagrangian point L1 as shown on the plot. The panels from top to bottom show magnetic field magnitude (B), vectors (B_x, B_y, B_z), latitude (θ_B) and longitude angles (ϕ_B) of the magnetic field, plasma speed (V_{SW}), density (N_p), temperature (T_p), and plasma beta (β). The vertical black dotted line indicates the shock, and the red and blue vertical lines show the start and end times of the ICME plasma, respectively.

represents the absence of Lorentz force $\mathbf{J} \times \mathbf{B}$. It implies that \mathbf{J} is parallel to \mathbf{B} which follows that follows Equation 1.6 (Goldstein, 1983; Burlaga et al., 1981). In cylindrical coordinates (r, θ, z), if cylindrical symmetry applies, i.e., magnetic field varies only with r (Goldstein, 1983; Choudhuri, 1998) is assumed, then Equation 1.6 gives $-\frac{dB_z}{dr} = \alpha B_\theta$ and $\frac{1}{r} \frac{d}{dr}(rB_\theta) = \alpha B_z$. These equations are satisfied

by $B_z = B_0 J_0(\alpha)r$ and $B_\theta = B_0 J_1(\alpha r)$ (Choudhuri, 1998), where B_0 and α are considered to be constant and J_0 and J_1 are zeroth and first order bessel functions, respectively. A schematic illustrating the force-free cylindrical structure of an MC is shown in Figure 1.13II. The MC axis lies on the equatorial plane and perpendicular to the radial direction \hat{r} . An observer crossing the axis of the MC flux-rope radially will notice the rotation of the magnetic field in a plane shown above of the schematic. MCs expand during their propagation (Burlaga et al., 1981; Burlaga, 1991) and the expansion is manifested by a smooth decrease in MC speed (as shown in Figure 1.12II). Also, low proton temperature is believed to be a result of MC expansion (Burlaga, 1991). A study by Ivanov, Kharshiladze, and Romashets (1993) interpreted that the velocity profile of MCs results from the combined effect of MC expansion and deceleration by the ambient solar wind.

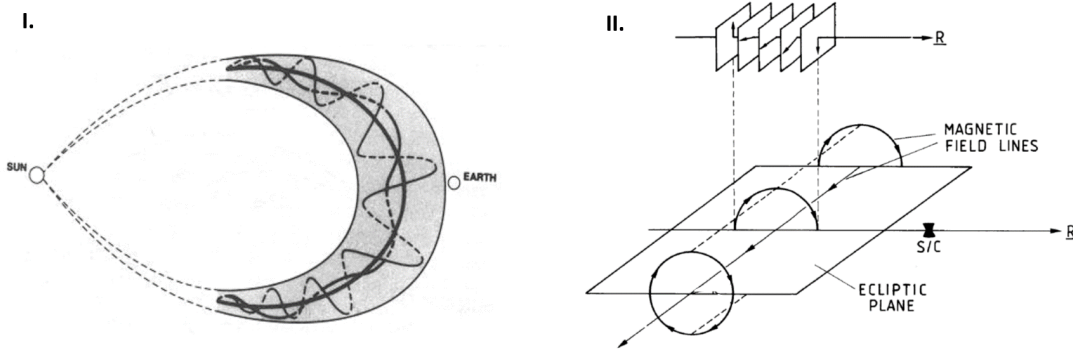


Figure 1.13: I. Magnetic field orientation inside an MC (Burlaga 1990). II. An idealised sketch of a cylindrical MC whose axis is on the equatorial plane and perpendicular to the Sun-Earth line. When this MC crosses a spacecraft (S/C), the rotation of the magnetic field vector that the S/C observes is shown on the upper part of the Figure (Goldstein, 1983).

1.4 Space weather consequences: Geomagnetic storms

Since the First Polar Year (1882-1883), “geomagnetic storms” (Gonzalez et al., 1994) are defined as intense and irregular variabilities of geomagnetic field occur-

ring due to solar disturbances. S. Chapman reasoned that the cause of worldwide geomagnetic disturbances are electric current, i.e., the ring current encircling the Earth (Kamide and Chian, 2007). The ring current is carried by energetic ions having energies of 10-200 KeV. The ring current particles are confined to the inner magnetosphere, i.e., 2-7 R_E , where R_E represents the Earth's radius. The particles flow westward (the direction of ions) and eastward (the direction of electron) around the Earth as the curvature drift and gradient drift of the particles superpose and reinforce one another. Thus, the ring current flows toward West in the equatorial plane (Prölss, 2012). An injection of energetic particles through the Earth's magnetotail results in the growth of the ring current that causes geomagnetic disturbances at low latitude regions by decreasing the intensity of the Earth's horizontal magnetic field (Howard, 2014). The north-south component of the interplanetary magnetic field mainly regulates the injection of energetic particles in the Earth's magnetosphere (Kamide and Chian, 2007).

The magnetosphere shields our planet from cosmic and solar energetic particle radiations. The Earth has a northward directed quasi-dipolar magnetic field at the dayside (toward the Sun). Solar transients (such as CMEs, SIRs) can cause deviations from the ambient solar wind in terms of plasma flow speed and strong out-of-ecliptic magnetic field component which further reconnects with the geomagnetic field on the dayside (Howard, 2011). Through the reconnected magnetic field lines, solar energetic particles enter and precipitate at the Earth's polar regions. The particles energize the atmosphere and result in an emission of light in the forms of spectacular auroras (Kamide and Chian, 2007). On the other hand, the reconnected field lines are dragged toward the magnetotail and initiate reconnection at the night-side as well (Dungey, 1961). Thus, the solar energetic particles are injected into the inner magnetosphere from the tail plasma sheet and contribute to the ring current. Therefore, the reconnection between solar transients and geomagnetic field has two major effects on the Earth's magnetosphere. Those are (1) insertion of energetic particles into the magnetosphere through open geomagnetic field lines resulting from reconnection and (2) injection of the energy released by reconnection process into the Earth's magnetosphere. Thus, reconnection causes massive disruptions to the magnetospheric system and results in geomagnetic storms. Fig-

Figure 1.14 shows a schematic illustrating the interaction between the southward IMF (shown in blue) and the Earth's dipolar magnetic field (indicated in red) at the day-side magnetopause. The orange curves represent the reconnected field lines which again reconnect at the magnetotail. The direction of the flow of plasma at the magnetopause and magnetotail regions are indicated using black arrows.

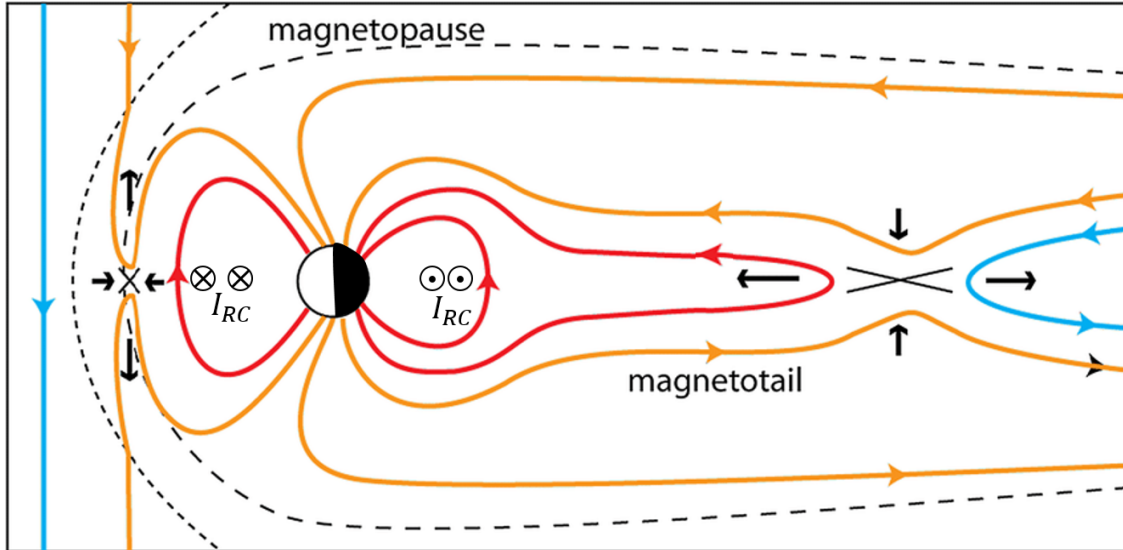


Figure 1.14: A schematic showing the configuration of the geomagnetic field when southward IMF's (blue lines) arrive at the Earth. The reconnection sites at the day-side magnetopause and magnetotail are shown by 'X'. The Earth's closed magnetic field and the reconnected field lines are shown in red and orange, respectively. I_{RC} represents the westward directed ring current. Black arrows show the direction of plasma flow due to the reconnection. Image credit: Eastwood et al. (2017).

Several studies have shown that large geomagnetic storms are caused due to high-speed solar wind flow and prolonged interval of strong southward IMF's (Rostoker and Fälthammar, 1967; Burton, McPherron, and Russell, 1975). As high speed flows, strong magnetic field intensity with southward magnetic field component are common characteristics of ICMEs and ICME driven interplanetary disturbances, CMEs are observed to be one of the major sources of geomagnetic storms (Gosling, 1993). In summary, the major effects of geomagnetic storms are (Howard, 2014)

- generation of fluctuations in the geomagnetic field's magnitude and orientation,
- reconfiguration of plasma and magnetic components of magnetosphere,

- enhancement of energetic particles in the magnetosphere causing an intensification of the magnetospheric ring current and radiation belts.

1.4.1 Geomagnetic indices

Geomagnetic indices are introduced to monitor geomagnetic activities. The indices are measured using observations from a network of ground-based magnetometers. The indices represent different aspects of the dynamic geomagnetic field. Two widely used indices are Dst (Sugiura et al., 1964) and k_p . Both ring current and auroral electrojets contribute to k_p index. The index k_p measures the deviations of Earth's horizontal magnetic field component in a semi-logarithmic scale and ranges from 0 (quiet) to 9 (active). It is computed every 3 hours using all magnetometer observations. The most commonly used geomagnetic index is the Dst (Disturbance storm time) index proposed by Kamide and Chian (2007). It is defined as $Dst = 1/N \sum_{n=1}^N \frac{H - H_{quiet}}{\cos\sigma}$, where H is the horizontal component of magnetic field disturbance, H_{quiet} is the same component during the quietest days, N , and σ represent the total number of stations and station latitudes, respectively. The calculation of Dst involves observations from four magnetometer stations located near the Earth's equator. It measures the variations of the Earth's dipole field caused by the ring current every hour. The minimum value of Dst (Dst_m) throughout a storm period defines the magnitude of a geomagnetic storm (Gonzalez et al., 1994). During a classic storm, Dst shows three phases (Kamide et al., 1998) – initial phase, main phase, and storm recovery phase. The initial phase represents small variations in field intensity that follows the storms sudden commencement (SSC; a sudden positive enhancement due to southward IMF). The main phase shows a sharp decrease in field intensity that defines the intensification of the ring current, and the storm recovery phase corresponds to the gradual recovery of the ring current. Depending on the Dst values, Zhang et al. (2007) has categorised a storm as minor ($0 \text{ nT} > Dst_m > -50 \text{ nT}$), moderate ($-50 \text{ nT} \leq Dst_m < -100 \text{ nT}$), and major ($Dst_m \leq -100 \text{ nT}$).

1.4.2 The CME link to geomagnetic disturbances

The ability of an interplanetary structure to cause a geomagnetic storm is known as geoeffectiveness. When a prolonged out-of-ecliptic southward magnetic field component B_z of a high speed interplanetary magnetic structure reconnects with the Earth's magnetosphere, the solar wind energy enters into the magnetosphere. The major sources of such magnetic field structures in the interplanetary medium are CMEs (Lindsay, Russell, and Luhmann, 1995; Echer, Gonzalez, and Alves, 2006). Using statistical analysis, Srivastava and Venkatakrishnan (2002) have shown that an increased ram pressure (p_{ram}) causing a sudden compression of the Earth's magnetosphere (Gonzalez, Tsurutani, and De Gonzalez, 1999) is a good predictor of the geomagnetic activity. The ram pressure p_{ram} is generated across the interplanetary shocks produced by high speed CMEs and it is proportional to the density and speed of the solar wind. Wu and Lepping (2006) found that the intensity of geomagnetic storm in a solar active period is higher than a quiet period because of the presence of strong southward B_z and high speed CMEs. According to Green and Baker (2015), one of the factors that trigger the geoeffectiveness of CMEs is its high dynamic pressure. Magnetic clouds (MCs), a subset of ICMEs, are primarily responsible for causing intense geomagnetic storms as they usually have a long-lasting strong southward B_z (Burlaga et al., 1981; Wilson, 1990).

To understand the connection between CME kinematics and geomagnetic storm intensity, Gopalswamy (2009) derived the distribution of plane-of-sky speed and width of CMEs that produced major geomagnetic storms ($Dst_m \leq -100$ nT) in the course of solar cycle 23. The study found that the speed distribution peaks at 700 km/s and has an average value of 999 km/s. The peak value of the width distribution was found to be 360° . Also, an intermediate correlation with correlation coefficient $r = -0.68$ (Gopalswamy et al., 2008) between MC speed V_{MC} and Dst_m suggests that mainly the fast and wide CMEs are responsible for major geomagnetic storms. To understand the connection between CME's magnetic nature and associated geomagnetic storm intensity, Gopalswamy et al. (2008) studied the effect of total magnetic field intensity B_t , southward magnetic field intensity B_z , and the speed-magnetic field product ($V_{MC}B_z$) on Dst_m using statistical analysis. They found a high correlation between Dst_m and B_t ($r = -0.83$) and Dst_m and B_z

($r = -0.82$). The correlation between $V_{MC}B_z$ and Dst_m was the highest ($r = 0.91$). The product of V_{MC} and B_z provides the electric field directed perpendicular to the Sun-Earth line in ecliptic plane. The electric field contributes to the interplanetary energy flux that is estimated by the Poynting flux $\mathbf{E} \times \mathbf{B}/4\pi$ (Perreault and Akasofu, 1978) entering the magnetosphere over a storm period, where \mathbf{E} and \mathbf{B} represent the interplanetary electric and magnetic fields, respectively. Perreault and Akasofu (1978) demonstrated that part of the Poynting flux that enters the magnetosphere across the dayside is closely related to the growth of geomagnetic storms. Gopalswamy et al. (2008) obtained a linear empirical relationship between $V_{MC}B_z$ and Dst_m which has important implications for forecasting space weather. The relationship between $V_{MC}B_z$ and Dst_m is in agreement with the studies by Wu and Lepping (2006) and Gonzalez and Echer (2005). Gopalswamy (2009) found a significant correlation ($r = 0.78$) between CME and MC speed. It suggests a strong dependency of the 1-AU MC speed on their associated CME speed near Sun (although CMEs are subjected to the drag force depending upon their speed, physical properties and ambient solar wind condition during their interplanetary propagation). Therefore, to obtain the geoeffectiveness of CMEs, understanding the origin and evolution of their kinematics and magnetic properties which primarily determine the strength of the CME associated geomagnetic disturbances is necessary.

1.5 Motivation and thesis outline

Being one of the significant space weather drivers, understanding the origin and dynamics of CMEs are of great importance in predicting geomagnetic storms that lead to a multitude of space weather effects (Pulkkinen, 2007). While colliding with the Earth's magnetosphere, a high-speed CME compresses the dayside magnetosphere, and with southward magnetic field orientation, it may lead to magnetic reconnection (Wilson, 1987; Tsurutani et al., 1988; Gonzalez, Tsurutani, and De Gonzalez, 1999). By re-configuring the magnetic field lines and converting magnetic energy to other forms, the reconnection causes significant magnetospheric disturbances that produce geomagnetic storms. The near-Earth kinematics and magnetic nature of CMEs are prime determinants of their arrival speed and time at Earth and their

geoeffectiveness (e.g., Gopalswamy et al., 2015; Gopalswamy, 2009). Therefore, knowledge of the origin and evolution of kinematics and magnetic characteristics of CMEs is necessary to forecast its arrival time, speed and geoeffectiveness. Moreover, a reliable prediction of ICME's magnetic field intensity and orientation in a plane perpendicular to the ecliptic plane is of prime interest to determine its geoeffectiveness. Due to the complexity of the heliospheric environment causing dramatic evolution of CME properties (e.g., Vourlidas et al., 2011; Isavnin, Vourlidas, and Kilpua, 2013), forecasting the magnetic field orientation of ICMEs is a challenging task. The influence of near-Earth CME properties on the strength of geomagnetic storms has been investigated by several studies (Srivastava and Venkatakrisnan, 2002; Wu and Lepping, 2006; Michalek et al., 2006; Gopalswamy et al., 2008; Gopalswamy, 2009; Gopalswamy, 2010). Using statistical analysis, several studies found the *Dst* index to be significantly correlated with associated ICME speed (Gopalswamy et al., 2008), the strength of ICME's southward magnetic field (Gopalswamy et al., 2015; Lawrance, Moon, and Shanmugaraju, 2020), and the product of these two parameters (Gopalswamy et al., 2008; Gopalswamy et al., 2015; Lawrance, Moon, and Shanmugaraju, 2020). Furthermore, observational analysis by Harrison (1990) and Subramanian and Dere (2001) and Michalek and Yashiro (2013) infer that the major solar sources of CMEs are solar active regions and the properties of active regions ascertain their associated eruption characteristics. Although interplanetary propagation of ICMEs is influenced by ambient solar wind speed and IMF intensity (Vršnak et al., 2013), the inherent features of ICMEs are determined by the properties of their associated CMEs and solar sources (Gopalswamy et al., 2008; Gopalswamy et al., 2017a; Qiu et al., 2007).

This thesis primarily aims to investigate the key factors determining the kinematics and magnetic properties of CMEs at their solar sources and deals with the evolution of CME magnetic properties in the course of their interplanetary propagation. This thesis attempts to forecast the magnetic structure, magnetic strength and field orientation of interplanetary CMEs and thus their geoeffectiveness. Major issues which are addressed in this thesis are as follows.

- What determines the kinematics of CMEs?
- How are the solar magnetic flux and helicity transferred to CME flux ropes?

- How are the magnetic properties and geoeffectiveness of CMEs affected during their interplanetary propagation?
- How do we predict the geoeffectiveness of CMEs?

The studies carried out to accomplish the aforementioned objectives are organised into four chapters. By exploring the dependency of CME kinematics on the magnetic characteristics of associated active regions, Chapter 2 establishes out the key factor that governs the near-Sun kinematics of CMEs. Chapter 3 connects the magnetic properties – magnetic flux and helicity of flux ropes through the Sun-Earth system and identifies the origin of magnetic properties in near-Sun flux ropes such as CMEs. Chapter 4 deals with the distortion of CME’s magnetic properties such as magnetic flux during its interplanetary propagation and discusses the flux erosion of ICME flux ropes, i.e., magnetic clouds (MCs) due to interaction with the ambient interplanetary magnetic field. Also the impact of erosion on the geoeffectiveness of MCs is established. Chapter 5 provides an approach for forecasting the magnetic vectors within the Earth-directed segment of ICME flux ropes. It provides a solution to the most challenging problem in space weather forecasting, i.e., prediction of the southward B_z . Conclusions and a future outlook are discussed in Chapter 6.

Chapter 2

Dependence of CME kinematics on their solar source active regions

Chapter Summary

The near-Sun kinematics of coronal mass ejections (CMEs) determine the severity and arrival time of associated geomagnetic storms. This Chapter investigates the relationship between the deprojected speed and kinetic energy of CMEs and magnetic measures of their solar sources and intrinsic flux rope characteristics. Based on an analysis we report that the correlation between CME speed and their source active region size and global nonpotentiality is weak, but not negligible. We find the near-Sun velocity and kinetic energy of CMEs to be well correlated with the associated magnetic reconnection flux. We establish a statistically significant empirical relationship between the CME speed and reconnection flux that may be utilized for prediction purposes. Our results constrain processes related to the origin and propagation of CMEs and may lead to better empirical forecasting of their arrival and geoeffectiveness.

2.1 Introduction

A Coronal mass ejection (CME) represents one of the most energetic phenomenon on the Sun, ejecting a massive amount of solar magnetized plasma (order of 10^{12} kg) carrying significant energy ($10^{31} - 10^{33}$ erg) (e.g., Gosling et al., 1974; Hund-

hausen, 1997; Gopalswamy, 2016; Manchester et al., 2017; Green et al., 2018) in to interplanetary space. The origin of CMEs is related to the magnetic field dynamics on the solar photosphere (e.g., Nandy et al., 2007). If a CME is directed towards Earth, it may cause major geomagnetic storms depending upon its kinematics, magnetic structure and magnetic field strength at 1 AU (e.g., Gopalswamy, 2009; Kilpua et al., 2017). When a high-speed interplanetary CME (ICME) with an enhanced southward magnetic field component hits the Earth, it reconnects with the Earth's magnetosphere, enhances the ring current (Kamide et al., 1998) and temporarily decreases the strength of Earth's horizontal magnetic field component. Such solar-induced magnetic storms can result in serious disruptions to satellite operations, electric power grids and communication systems. Understanding the origin of CMEs, their subsequent dynamics and developing forecasting capabilities for their arrival time and severity are therefore important challenges in the domain of solar-terrestrial physics.

Near-Sun kinematic properties is one of the features of CMEs that can be used to predict the intensity and onset of associated geomagnetic storms (Srivastava and Venkatakrisnan, 2002). In order to predict the CME arrival time at 1 AU, several empirical and physics based models constrain CME propagation through interplanetary space (Gopalswamy et al., 2001; Gopalswamy et al., 2013a; Cho et al., 2003; Fry et al., 2003; Gopalswamy et al., 2013a; Vršnak et al., 2013; Mays et al., 2015; Takahashi and Shibata, 2017; Dumbović et al., 2018; Möstl et al., 2014). The models are usually based on the initial speed of CMEs. CMEs originate in closed magnetic field regions on the Sun such as active regions (ARs) (Subramanian and Dere, 2001) and filament regions (Gopalswamy et al., 2015). Several studies have attempted to connect the near-Sun CME speeds and magnetic measures of their source regions (Kim et al., 2017; Tiwari et al., 2015; Wang and Zhang, 2008; Moon et al., 2002). Fainshtein, Popova, and Kashapova (2012) studied the projected speed of 46 halo CMEs and found that the CME speed is well correlated with the average intensity of line-of-sight magnetic fields at CME associated flare onset. A recent study by Gopalswamy et al. (2017b) and Qiu et al. (2007) showed that the poloidal magnetic flux of flux rope ICMEs at 1 AU depends on the photospheric magnetic flux underlying the area swept by the flare ribbons or the post eruption arcades on

one side of the polarity inversion line (defined as flare reconnection flux). Extension of these studies offer great potential for better constraining the origin and dynamics of CME flux ropes.

Magnetic reconnection plays an essential role at the early stage of CME dynamics. Theoretical calculations, numerical simulations and observational analysis show that enhancement of CME mass acceleration is accompanied by an enhancement in the rate of magnetic reconnection at its solar source (Lin and Forbes, 2000; Cheng et al., 2003; Deng and Welsch, 2017). Also, an observation by Qiu et al. (2004) revealed a temporal correlation between the reconnection rate inferred from two-ribbon flare observations and associated CME acceleration. Several previous studies attempted to compare the total flux reconnected in the CME associated flares and CME velocity and observed a strong correlation between these parameters (Qiu and Yurchyshyn, 2005; Miklenic, Veronig, and Vršnak, 2009; Gopalswamy et al., 2017b). It is well established that the acceleration phase of CMEs is synchronized with the impulsive phase of associated flares (Zhang et al., 2001; Gallagher, Lawrence, and Dennis, 2003). A study by Bein et al. (2011) found that CMEs originating from compact sources at lower corona are more impulsive and reach higher peak accelerations at lower heights. Temmer et al. (2008) observed a close relationship between CME acceleration and flare energy release during its impulsive phase. There exists a feedback relationship between flares and associated CMEs through magnetic reconnection that occurs in the current sheet formed below the erupting CME flux rope (Temmer et al., 2010; Vršnak, 2008; Vršnak, 2016). This reconnection process significantly enhances the mass acceleration of the ejections as well as release energy through the accompanied two-ribbon flares (Forbes, 2000; Lin and Forbes, 2000). These studies motivate us to explore the relationship between CME kinematics and the magnetic reconnection which causes the CME flux rope eruption.

CMEs are typically observed by coronagraphs which occult the photosphere of the Sun and expose the surrounding faint corona. Basic observational properties of CMEs such as their structure, propagation direction, and derived quantities such as velocity, accelerations, and mass are subject to projection effects depending on the location of the CME source region on the solar surface (Burkepile et al., 2004; Schwenn et al., 2005; Vršnak et al., 2007; Howard, Nandy, and Koepke,

2008). The coronagraphs of the Sun-Earth Connection Coronal and Heliospheric Investigation (SECCHI, Howard et al., 2008) aboard the Solar TERrestrial RELations Observatory (STEREO) spacecrafts A & B provide simultaneous observations of CMEs from two different viewpoints in space. Applying the forward modeling technique (Thernisien, Howard, and Vourlidas, 2006; Thernisien, Vourlidas, and Howard, 2009; Thernisien, 2011) to CME white-light images observed from different vantage points, one can better reproduce CME morphology and dynamics. Thus deprojected CME parameters can be estimated (Bosman et al., 2012; Shen et al., 2013; Xie, Gopalswamy, and St. Cyr, 2013).

In this Chapter, we examine the size, nonpotentiality and the flare reconnection flux of CME associated flaring active regions using observations from different instruments on the Solar Dynamic Observatory (SDO, Pesnell, Thompson, and Chamberlin, 2012) and connect them with CME kinematics and flux properties. Gopalswamy et al. (2017b) studied about 50 CMEs from solar cycle 23 and their flux rope properties. Here we consider a number of CMEs from cycle 24 using a different flux rope fitting method for multi-view observations and confirm, extend and set better constraints on the relationship between CME properties and its source regions.

We organize this Chapter as follows. In Section 2.2 we describe the procedure of selecting CMEs and their associated solar sources and summarize the method of measuring the deprojected geometric properties of CMEs and the magnetic properties of their solar sources. In Section 2.3 we examine the relationship between CME kinematics with magnetic measures of their source regions as well as their intrinsic, near-Sun flux rope magnetic properties. We discuss our results in Section 2.4 and conclude in Section 2.5.

2.2 Methodology

We construct a list of 438 CMEs which have clear flux-rope morphology (determined manually) characterized by a bright front encompassing a dark cavity that surrounds a bright core and appear as a single event in each data frame of white-light movies provided by SECCHI/COR2 A & B during solar cycle 24 (between the initiation of

SDO observations in May 2010 and until data from both STEREO spacecrafts are available). We also identify the observed CMEs in the images obtained by the Large Angle and Spectrometric Coronagraph (LASCO) (Brueckner et al., 1995) telescope’s C2 and C3 on board Solar and Heliospheric Observatory (SOHO, Domingo, Fleck, and Poland, 1995). The corresponding solar source location of the CMEs were determined using SDO’s Atmospheric Imaging Assembly (AIA) (Lemen et al., 2012) images at 193 Å and SECCHI’s Extreme Ultraviolet Imager (EUVI) data at 195 Å. From the list of selected events we isolate those which originated on the Earth facing side of the Sun. In our study, we consider the source ARs within $\pm 45^\circ$ longitude from the disk center to avoid projection effects in magnetogram observations of ARs. We further short list the events by the requirement that their source regions have been identified by NOAA and that their vector magnetograms exist from Helioseismic Magnetic Imager observations (HMI, Scherrer et al., 2012) on board SDO. This careful manual selection method leaves only 36 CMEs for our study.

The flux rope structure of the identified CMEs allows us to apply the Graduated Cylindrical Shell (GCS) forward modeling technique developed by Thernisien, Howard, and Vourlidas (2006). The GCS model is meant to reproduce the large-scale structure of flux ropes by a tubular section (main body) attached to two cones representing the flux rope legs. Thus, the shape of the model looks like a croissant. The model’s cross section forms a circular annulus with a radius R_0 being a function of r – a distance between the Sun’s center and the shell’s outer edge. Thus, R_0 is given by, $R_0(r) = \kappa r$, where κ is a constant representing the aspect ratio of the flux rope. The model is based on an asymmetric Gaussian electron density profile that peaks at the shell’s outer surface (at R_0) and falls off with different Gaussian width on either side. Figure 2.1 shows the GCS model’s face-on (Figure 2.1(a)) and edge-on (Figure 2.1(b)) views. The axis of the model is indicated by dash-dotted line and the model outline is shown by a solid line. The height of the flux rope leg is represented by h_{leg} . The Gaussian electron density profile (N_e) is shown on the upper-right of the edge-on view of the model. Here, the distance d is along R_0 and starts from the shell center. The leading and trailing fall off coefficients of the Gaussian profile are represented by σ_l and σ_t , respectively.

The GCS model helps derive the deprojected parameters of CMEs from pro-

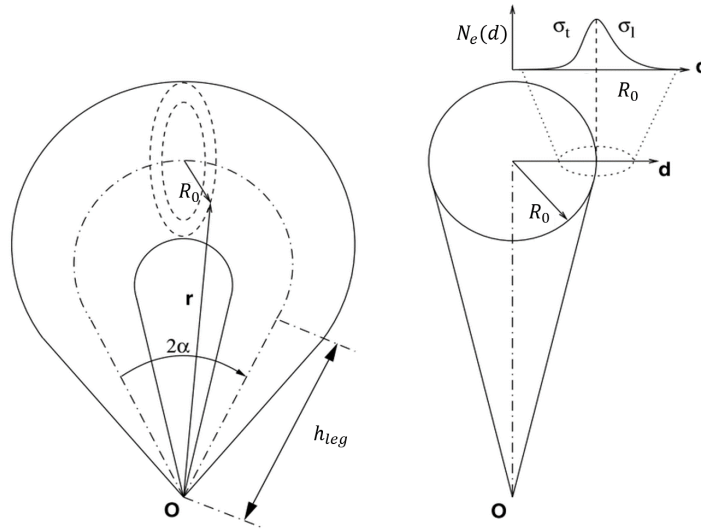


Figure 2.1: Face-on (a) and edge-on (b) views of GCS model where the solid line represents the model's outline, dash-dotted line is the axis of the model, dotted circular annulus indicates the model's cross section. On the upper-right of (b) the electron density profile (N_e) is shown. The image is adapted from (Thernisien, Howard, and Vourlidas, 2006).

jected white-light images (e.g., Liu et al., 2010; Poomvises, Zhang, and Olmedo, 2010; Vourlidas et al., 2011). The six geometric parameters, which model the flux rope CMEs are the propagation longitude (ϕ), latitude (θ), aspect ratio (κ), tilt angle (γ) between the source region neutral line and the equator, the half angular width between the legs (α) and the height (h) of the CME leading edge (see Figure 1 of Thernisien, Howard, and Vourlidas (2006)). By adjusting these six parameters manually, we try to achieve the best match between the model CMEs and the observed CMEs in LASCO and STEREO coronagraphs. In Figure 2.2, we show an example of GCS model fitting result. The model is applied to COR2 A & B and calibrated (Level 1) LASCO C3 base difference white-light CME images. The COR2 images are used after being processed by the standard routines (`secchi_prep`) available in SolarSoft. For a well fitted CME, we obtain the CME speed by tracking its leading edge until it reaches the edge of the field of views (FOVs) of the coronagraphs. Some of the observed CMEs become faint before reaching the edges of the FOVs of the coronagraphs. The deprojected propagation speed of CME (V_{gcs})

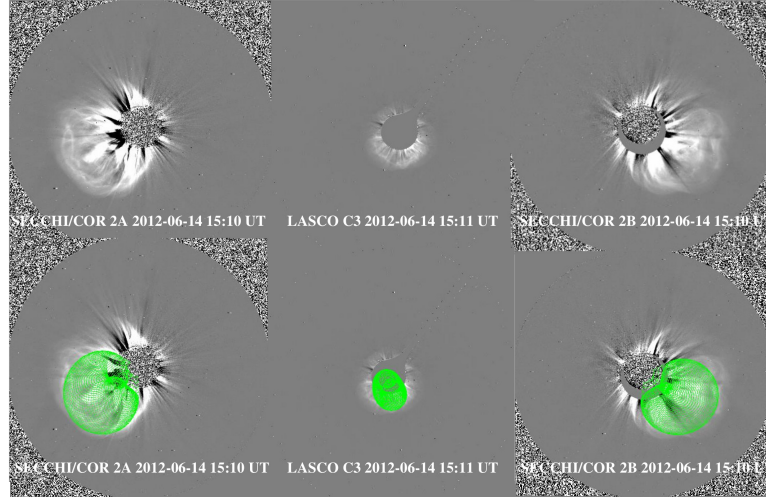


Figure 2.2: Forward modeling of white-light images of CME (observed on 14 June, 2012) with the GCS model. Top three panels (left-to-right) represent CME white-light images observed by STEREO B, LASCO C3, and STEREO A, respectively. Bottom three panels show CME with GCS wire frame (in green symbol) overlaid on top. The fitting results the deprojected geometric parameters of the CME as, $\phi = 89.07^\circ$, and $\theta = -32^\circ$ (in Carrington co-ordinate), $\gamma = -67^\circ$, $\kappa = 0.58$, $\alpha = 23^\circ$, and $h = 10.5R_s$

we quote here is obtained by linear fitting of the height-time measurement of CME leading edges propagating within the FOVs of the coronagraphs.

To obtain the magnetic properties of source ARs, we use Space-Weather HMI AR Patch (SHARP) data series (hmi.Sharp_cea_720s) and full disk HMI vector magnetogram data series (hmi.B_720s) along with the AIA 193 Å data. The hmi.B_720s data series provides vector field information in the form of field strength, inclination and azimuth in plane-of-sky co-ordinates (Hoeksema et al., 2014). We perform a co-ordinate transformation and decompose the magnetic field vectors into r (radial distance), θ (polar angle), and ϕ (azimuthal angle) components in spherical co-ordinates (Sun, 2013). To derive the vector magnetic field components we use HMI pipeline codes publicly available in the SDO webpage. In our data set, we find many ARs identified with different NOAA numbers although they are magnetically connected. Therefore, we use SHARP vector magnetograms (as each AR patch includes single or multiple connected ARs) to measure the global magnetic parameters of source ARs.

2.2.1 Magnetic properties of ARs and CMEs

In this section, we discuss the magnetic properties of ARs and describe the methods used to measure their properties. Guided by widely utilized AR characteristics in the community in this context, we consider a few relevant AR parameters for our study. We determine the total unsigned magnetic flux as a proxy of AR size. We also determine the AR nonpotentiality through estimates of three different proxies – total unsigned vertical current, total photospheric magnetic free energy density, and length of the strong field neutral line. We further compute the magnetic reconnection flux in the low corona associated with each event by utilizing the fact that post eruption arcades (PEAs) map out the reconnection region leading to formation of flux ropes during solar eruptive events. (Qiu et al., 2007; Longcope and Beveridge, 2007; Hu et al., 2014; Gopalswamy et al., 2017a). We obtain the magnetic properties of CME flux rope following the Flux Rope from Eruption Data (FRED) technique that combines the reconnection flux with geometrical flux rope properties (Gopalswamy et al., 2017b; Gopalswamy et al., 2017c; Pal et al., 2017).

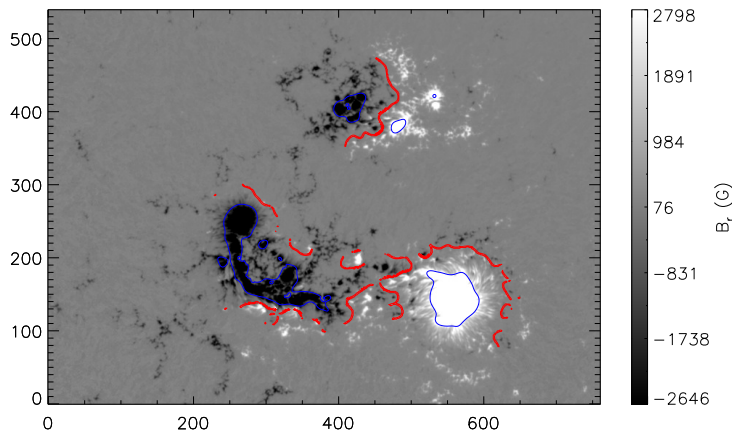


Figure 2.3: SHARP vector magnetogram of AR 11504 on 14 June 2012 from which a CME erupted at 12:48 UT. Blue contours define the region above the disambiguation noise threshold ($B_r \approx 150$ G, CONF_DISAMBIG= 90). The red lines denote the strong field neutral lines associated with the magnetic field distribution. The vertical, gray color bar shown on the right depicts the values of B_r . The maximum and minimum B_r of the AR are respectively, 2798 G and -2645 G.

Total unsigned magnetic flux

The total unsigned magnetic flux (ϕ_{AR}) of an AR is calculated by integrating the radial magnetic field component (B_r) over the high-confidence region within the HARP. Here the high-confidence region is defined by cluster of pixels above the disambiguation noise threshold (where the confidence in disambiguation, CONF_DISAMBIG is equal to 90; see Table A.5 of Bobra et al. (2014)). Thus, ϕ_{AR} is defined by,

$$\phi_{AR} = \int |B_r| dA \quad (2.1)$$

Here each pixel area is defined by $A (= 0.5'' \times 0.5'')$. In Figure 2.3, we display an example of a SHARP vector magnetogram of AR NOAA 11504 located at S17E06, where, the blue contours enclose regions with B_r values greater than the noise threshold.

Total vertical current

The vertical current density (J_z) is measured using Ampere's current law which gives,

$$J_z = \frac{1}{\mu} \left(\frac{\partial B_y}{\partial x} - \frac{\partial B_x}{\partial y} \right), \quad (2.2)$$

Where B_x and B_y are the observed horizontal components of AR magnetic field and μ is the magnetic permeability. The total unsigned vertical current (I_{tot}) is computed by integrating J_z over all pixels above the noise threshold (CONF_DISAMBIG=90).

Total photospheric free magnetic energy density (ρ_{tot})

Wang et al. (1996) define the density of the free magnetic energy (ρ_e) in terms of observed magnetic field (B_{obs}) and potential magnetic field (B_p) components obtained from vector magnetogram. The formula that is used to calculate this measure is,

$$\rho_e = \frac{(B_{obs} - B_p)^2}{8\pi} \quad (2.3)$$

Now ρ_{tot} is measured by integrating ρ_e over all the pixels above the noise threshold.

Length of strong field neutral line

The length of the strong field neutral line, L_{nl} is formulated as,

$$L_{nl} = \int_{B_{pt} > 150G} dl \quad (2.4)$$

Here the integration involves all neutral line increments dl on which the transverse potential magnetic field component (B_{pt}) of the vector magnetogram is greater than 150 G (Falconer, Moore, and Gary, 2008; Falconer et al., 2011). Also dl separates opposite polarities of B_r of at least 20 G (Falconer, Moore, and Gary, 2008). We calculate B_{pt} from B_r , where B_r is greater than the noise threshold. In Figure 2.3 we indicate the locations of neutral lines (in red) on which the transverse potential field is greater than 150 G.

Magnetic reconnection flux

To measure the magnetic reconnection flux (ϕ_{RC}), we use the PEA technique proposed by Gopalswamy et al. (2017a). In our study, we identify 33 out of 36 CMEs for which post-eruption loops are clearly observed in AIA 193 Å images. We mark the foot prints of PEAs on AIA 193 Å images and define the area under the PEAs by creating a polygon connecting the marked foot prints. We then overlay the polygon on the differential-rotation corrected full disk HMI vector magnetogram obtained ≈ 30 minutes before the onset of the eruption and integrate the absolute value of B_r in all the pixels within the polygon. The resulting ϕ_{RC} is half of the total flux through the polygon. Therefore, ϕ_{RC} is defined by,

$$\phi_{RC} = \frac{1}{2} \int_{PEA} |B_r| dA \quad (2.5)$$

In Figure 2.4(a) and (b) we show NOAA AR11504 in 193 Å (from the AIA instrument) and its vector magnetogram, respectively. The red dashed lines on both the images define the PEA foot prints.

Magnetic properties of CME flux ropes

We apply the “flux rope from eruption data” (Gopalswamy et al., 2017c, FRED) technique to obtain the magnetic properties such as axial magnetic field intensity, magnetic helicity of near-Sun coronal flux ropes. The technique, FRED combines

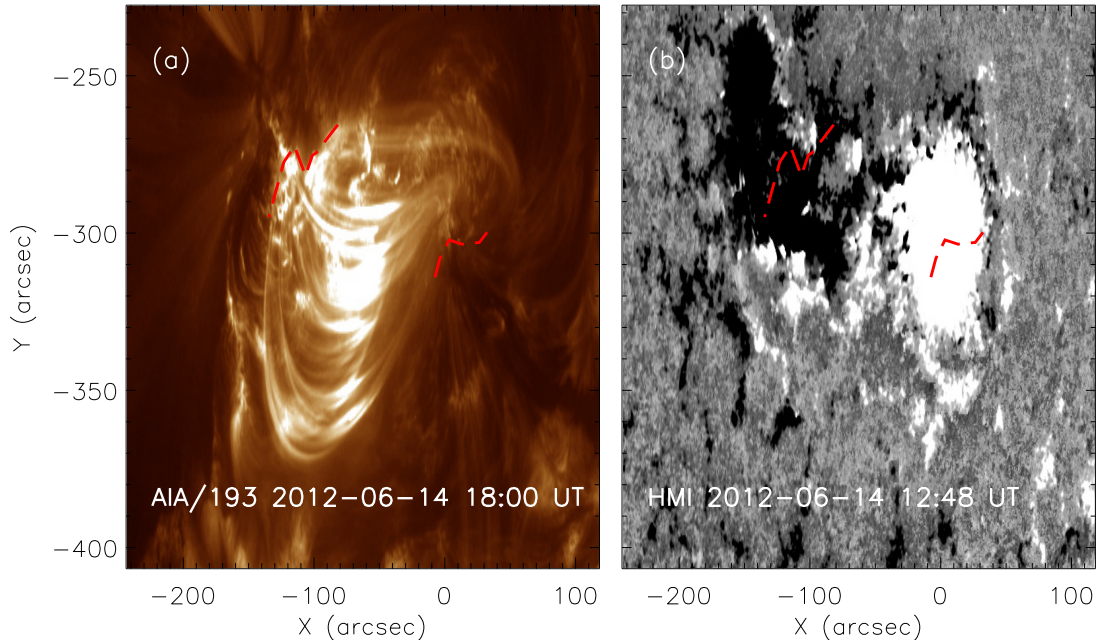


Figure 2.4: Post eruption arcade (PEA) and corresponding vector magnetogram associated with the 14 June, 2012 CME. (a) SDO/AIA/193 Å image of PEA observed in low corona at 18:00 UT. (b) HMI vector magnetogram of AR 11504 (solar source of the observed CME) at 12:48 UT. The red dashed lines in (a) and (b) represent the PEA foot prints. The ϕ_{RC} associated with the arcade is 7.45×10^{21} Mx.

two key results – (1) the photospheric magnetic flux ϕ_{RC} under post-eruption arcade that is approximately equal to the poloidal flux of flux ropes (Longcope and Beveridge, 2007; Qiu et al., 2007; Hu et al., 2014), and (2) flux rope geometric properties. Assuming CMEs as force free flux ropes, the axial, azimuthal magnetic field components, toroidal flux and helicity can be calculated. The relative magnetic helicity, H_m , is derived by subtracting the reference magnetic field (B_{ref}) helicity from the magnetic helicity (H) of a field B within a volume V (Berger and Field, 1984a) and is given by

$$H_m = \int_V A \cdot B dV - \int_V A_{ref} \cdot B_{ref} dV \quad (2.6)$$

Here A is the vector potential. For a CME with flux rope structure, $B_{ref} = B_z \hat{z}$ and $B = B_\phi \hat{\phi} + B_z \hat{z}$, where B_z is the axial magnetic field component and B_ϕ is the azimuthal magnetic field component of a cylindrical flux rope. The magnetic field components are derived using Lundquist's constant- α force-free field solution

in cylindrical coordinates (Lepping, Burlaga, and Jones, 1990). Using $A = B/\alpha$ we calculate the magnetic helicity of a CME flux rope as (Dasso et al., 2003; Démoulin et al., 2002; DeVore, 2000),

$$H_m = 4\pi L \int_0^{R_0} A_\phi B_\phi r dr \approx 0.7 B_0^2 R_0^3 L \quad (2.7)$$

Here R_0 is the radius of the circular annulus of CME at its leading edge point. It is defined by $R_0 = h/(1 + 1/\kappa)$ estimated using Equation 1 of Thernisien, Howard, and Vourlidas (2006). L is the length of CME flux rope approximated as $L = 2h_{leg} + (\pi/2 + \alpha)(h - h_{leg}/\cos\alpha) - 2R_\odot$ (Pal et al., 2017), where h_{leg} is the height of the CME flux rope legs (see Equation 3 of Thernisien, Howard, and Vourlidas (2006)) and $(\pi/2 + \alpha)$ is in radian. B_0 is the axial magnetic field strength of the CME defined by $B_{cme} = \phi_p x_{01}/LR_0$ (assuming a force-free CME flux rope). Here ϕ_p is the azimuthal flux of CME which is approximately equal to ϕ_{RC} and $x_{01} = 2.4048$ is the zeroth order Bessel function.

2.3 Analysis and Results

In this section, we analyze the relationship between CME kinematic properties, magnetic properties of their solar source regions, reconnection flux and associated flux rope characteristics. The inferred parameters are summarized in Table 2.1 which lists 36 CMEs and their properties along with the associated solar source information. The event numbers are shown in column 1. In column 2, we mention the dates and times when the CMEs first appear in the LASCO coronagraphs (CDAW LASCO CME catalog (http://cdaw.gsfc.nasa.gov/CME_list/), Yashiro et al., 2004; Gopalswamy et al., 2009). Column 3 shows the NOAA numbers of the CME associated source ARs. Column 4-9 represent the magnetic information (ϕ_{AR} , I_{tot} , ρ_{tot} , L_{nl} , ϕ_{RC}^p , ϕ_{RC}^r) of the identified ARs. Column 10 lists the mass of corresponding CMEs (M_{cme}) collected from LASCO CME catalog. Column 11 and 12 list α and V_{gcs} of CMEs. Column 13 and 14 represent the magnetic properties of CMEs – B_{cme} , and H_m .

Table 2.1: Properties of selected CMEs and associated source region information.

Event number	Date & time (DD-MM-YYYY hh:mm UT)	NOAA number	ϕ_{AR} (10^{22} Mx)	I_{tot} (10^{14} A)	ρ_{tot} (10^{24} erg cm $^{-1}$)	L_{nl} (10^9 km)	ϕ_{RC}^a (10^{21} Mx)	$\phi_{RC}^{(1)}$ (10^{21} Mx)	M_{cme} (10^{15} gM)	α ($^\circ$)	V_{ges} (km s $^{-1}$)	B_{cme} (mG)	H_m (10^{42} Mx 2)
(1)	(2)	(3)	(4)	(5)	(6)	(7)	(8)	(9)	(10)	(11)	(12)	(13)	(14)
1 ^b	01-08-2010 13:42	11092	1.28	0.533	0.4	0.306	9.36	2.96	-	23.20	1260	62.59	86.30
2 ^b	07-08-2010 18:36	11093	0.89	0.543	0.21	0.0288	1.58	4.75	-	14.81	779	14.92	1.87
3	14-02-2011 18:24	11158	2.50	1.39	0.83	5.63	4.54	-	0.86	22.36	359	51.44	12.40
4	15-02-2011 02:24	11158	2.69	1.55	0.85	5.15	10.4	11.6	4.3	28.51	868	119.13	62.90
5	01-06-2011 18:36	11226	2.81	1.73	0.36	3.28	1.49	2.2	1.8	22.64	527	20.29	1.09
6	02-06-2011 08:12	11227	2.39	1.67	0.34	3.1	1.81	1.7	1.4	17.33	1176.4	42.63	0.96
7	21-06-2011 03:16	11236	1.98	1.46	0.41	1.82	6.1	1.13	6.2	26.55	970	72.40	21.10
8	09-07-2011 00:48	11247	0.16	0.14	0.01	0.356	3.54	-	1.8	23.20	861	33.56	8.89
9	03-08-2011 14:00	11261	2.42	1.69	0.49	3.63	4.4	7.61	8.7	17.90	1228	55.26	10.70
10	04-08-2011 04:12	11261	2.56	1.81	0.44	3.74	5.58	8.26	11	24.87	1737	69.37	17.00
11	06-09-2011 23:05	11283	1.73	1.24	0.33	2.6	5.59	5.92	15	35.50	900	52.40	20.90
12	07-09-2011 23:05	11283	1.89	1.31	0.31	2.5	8.44	7.98	1.1	15.93	914	79.43	53.30
13 ^a	24-09-2011 19:36	11302	5.73	2.35	1.82	8.47	-	-	3.1	21.24	944.46	-	-
14	09-11-2011 13:36	11343	1.06	0.475	0.19	0.418	5.4	6.36	14	35.78	1285	29.02	28.30
15	26-12-2011 11:48	11384	2.08	1.27	0.6	2.06	1.95	1.09	4.3	6.98	777	21.79	2.46
16	19-01-2012 14:36	11402	7.01	4.02	1.32	7.07	10.4	4.56	19	25.50	1069	119.83	63.30
17	23-01-2012 03:12	11402	7.10	4.39	0.89	7.26	14.3	17.2	5.3	43.60	1916	116.40	144.00
18 ^a	06-06-2012 20:36	11494	1.15	0.74	0.3	2.58	-	2.05	2.6	13.13	569.4	-	-
19	14-06-2012 14:12	11504	3.75	1.96	1.19	9.62	7.45	3.88	12	23.00	1146	56.40	48.00
20	02-07-2012 20:24	11515	3.62	2.29	0.91	7.78	4.78	4.78	8.6	19.85	715	58.23	12.90
21	03-07-2012 00:48	11515	4.45	4.54	1.01	0.283	2.44	3.78	3	12.90	409	36.59	2.76
22	12-07-2012 16:48	11520	9.04	5.26	2.28	13.7	13.3	8.64	6.9	26.00	1700	129.30	103.00
23	14-08-2012 01:25	11543	1.47	0.974	0.43	3.34	1.3	1.04	1.8	15.40	457	15.25	1.01
24	28-09-2012 00:12	11577	2.41	1.75	0.24	2.15	2.81	2.33	9.2	30.00	1229.16	24.43	5.79
25	20-11-2012 12:00	11616	1.57	1.25	0.21	2.01	3.09	-	8.4	32.70	719	49.21	4.08
26	13-03-2013 00:24	11692	2.56	1.19	0.49	1.67	4.79	1.64	4.2	23.00	680.5	48.88	15.20
27	15-03-2013 07:12	11692	1.71	1.11	0.43	1.74	4.75	-	13	25.16	1354.4	64.23	11.40
28	11-04-2013 07:24	11719	1.83	1.55	0.25	2.45	5.04	4.5	22	36.33	1063	69.35	12.30
29	07-05-2013 09:36	11734	4.54	2.42	0.78	4.33	1.3	1.15	4.3	12.60	361	18.54	0.83
30	28-06-2013 02:00	11777	0.89	0.573	0.2	1.07	1.92	1.02	6.6	21.80	1069	38.29	1.28
31	07-08-2013 18:24	11810	0.58	0.418	0.03	0.356	2.29	-	3.1	23.48	521	21.72	3.71
32	12-08-2013 12:00	11817	1.81	0.799	0.27	1.94	2.75	3.46	3.1	19.30	395.8	49.87	2.88
33	17-08-2013 19:12	11818	1.55	0.99	0.41	2.05	6.09	6.1	12	25.43	986	73.71	20.70
34 ^a	26-10-2013 12:48	11877	3.33	2.08	0.76	4.32	-	0.8	3.3	20.12	472	-	-
35	07-01-2014 18:24	11944	8.38	4.78	2.82	12.8	10.9	11.6	22	31.30	2187.8	124.16	68.70
36	29-03-2014 18:12	12017	1.30	0.931	0.18	1.36	5	4.94	5	25.16	673.6	52.79	15.90

^a Events with undetected PEAs.

^b Events with unavailable mass information in LASCO CME catalog.

⁽¹⁾ Data collected from RibbonDB catalog.

2.3.1 Magnetic properties of ARs versus associated CME speeds

In Figure 2.5 we plot the deprojected speed of CMEs versus the unsigned magnetic flux and nonpotential parameters (I_{tot} , ρ_{tot} , and L_{nl}) of their progenitor ARs. We perform a correlation analysis and estimate the linear correlation coefficients (r) along with the confidence levels defined by (1-P-value). The P-value refers to the probability value of finding a result in a statistical study when the null hypothesis

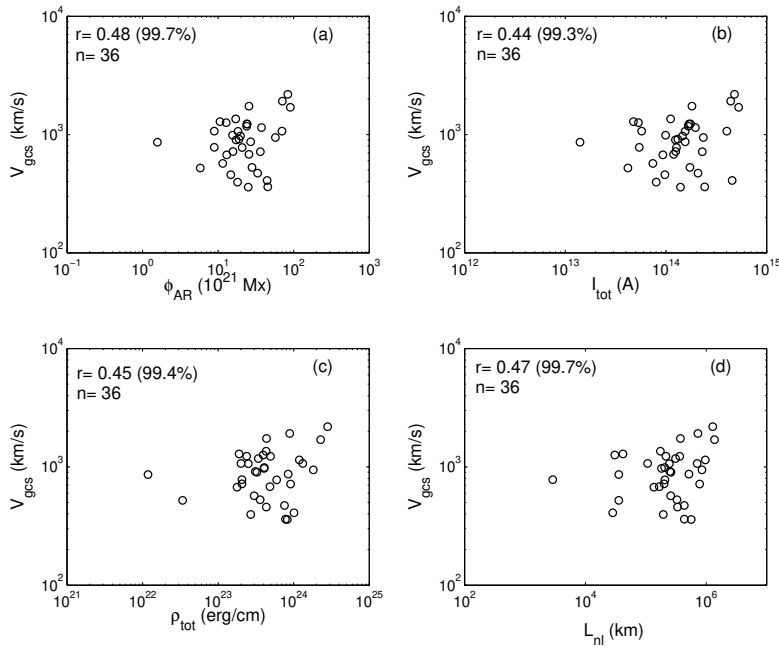


Figure 2.5: Scatter plots between V_{gcs} and (a) ϕ_{AR} , (b) I_{tot} , (c) ρ_{tot} , and (d) L_{nl} in our dataset. The Pearson’s linear correlation coefficients (r), confidence levels and the number of events (n) are mentioned in each of the plots.

is true. We mention r and $1-P$ -value in each of the plots of Figure 2.5. The correlation analysis implies a weak positive correlation between CME speeds and each of the AR magnetic parameters. The similarity of the correlation coefficients imply that the analyzed AR parameters are also inter-related, plausibly, through their dependence on AR size.

Our result is in agreement with numerical simulations which suggest that an AR can produce both fast and slow CMEs but the larger and more complex (non-potential) ones produce the fastest CMEs (Török and Kliem, 2007). Often, it is only a small part of a large AR that is involved in an eruption (Tiwari et al., 2015). Therefore, a single eruption is not enough to release the total free energy stored in ARs. Depending upon the release of free energy in each eruption, the associated CME speed may vary from slow to fast. So, complex ARs are capable of producing single or multiple eruptions and one should not necessarily expect a strong correlation between the CME speeds associated with individual events and source AR properties.

ϕ_{RC} of ARs versus properties of CMEs

Several investigations show that reconnection of coronal field lines during eruptive events like flare results in the formation of PEAs as well as flux ropes. In this section we identify the AR segments involved in eruptions using PEAs formed due to the flare reconnection process. We estimate the reconnection flux (ϕ_{RC}) of these segments and analyze their influence on CME kinematics. In Figure 2.6, we plot ϕ_{RC} versus V_{gcs} . The data points marked by ‘o’ (black) and ‘+’ (red) in the plot denote ϕ_{RC} measured using PEAs (referred as ϕ_{RC}^p) and ribbons (referred as ϕ_{RC}^r), respectively. We acquire ϕ_{RC}^r from the RibbonDB catalog (<http://solarmuri.ssl.berkeley.edu/~kazachenko/RibbonDB/>, Kazachenko et al., 2017). The catalog contains the active region and flare-ribbon properties of 3137 flares of GOES class C1.0 and larger located within 45 degrees from the central meridian and observed by SDO from April 2010 until April 2016. We find a significant positive correlation between V_{gcs} and ϕ_{RC} for both ϕ_{RC}^p and ϕ_{RC}^r (which are similar in their strength). The correlation coefficients are respectively 0.66 and 0.68 at 99.99% confidence level. The correlations are quite similar because the ϕ_{RC} for both the cases agree quite well (as was first shown by Gopalswamy et al. (2017a)). The correlation coefficients are lower than that reported by Qiu and Yurchyshyn (2005) for 13 events and Miklenic, Veronig, and Vršnak (2009) for 21 events but similar to that of Gopalswamy et al. (2017b) for 48 events of solar cycle 23. The linear least-squares fits to the relationships yield the regression equations,

$$V_{gcs} = 327\phi_{RC}^p{}^{0.69} km s^{-1}, \quad (2.8)$$

and

$$V_{gcs} = 430\phi_{RC}^r{}^{0.58} km s^{-1}, \quad (2.9)$$

respectively. Here ϕ_{RC} is in unit of 10^{21} Mx.

We analyze the relationship between ϕ_{RC} and kinetic energy of the resulting CMEs. Initially, we use CME masses (M_{cme}) listed in CDAW LASCO CME catalog and V_{gcs} to calculate the kinetic energy of CMEs (KE_{cme}^L). In Figure 2.7(a) we show the correlation between ϕ_{RC} and KE_{cme}^L . We find a weak positive correlation with a correlation coefficient of 0.44 which is greater than the Pearson’s critical correlation coefficient ($r_c = 0.306$) at 95% confidence level. It is well known that mass

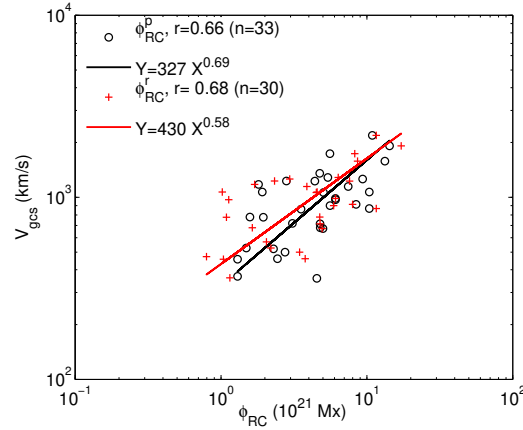


Figure 2.6: Scatter plot between ϕ_{RC} and associated V_{gcs} . The markers ‘o’ and ‘+’ denote ϕ_{RC}^p and ϕ_{RC}^r , respectively. The correlation coefficients (r) and number of events (n) corresponding to both ϕ_{RC}^p and ϕ_{RC}^r are shown in the plot. The black and red solid lines are the least-squares fits to the ϕ_{RC}^p - V_{gcs} and ϕ_{RC}^r - V_{gcs} pairs. The regression line equation for each solid line is depicted in the figure.

of wide CMEs measured using SOHO/LASCO white-light images suffers from serious projection effects. To estimate the true masses (M_{cme}^t) of CMEs, we use CME angular widths (AW s) in the equation $\log M_{cme}^t = 12.6 \log AW$ (Gopalswamy et al., 2005). The positive correlation ($r=0.56$ at 99% confidence level) between AW and ϕ_{RC} (shown in Figure 2.7(b)) statistically confirms that CME’s final angular width can be estimated from the magnetic flux under the flare arcade (Moore, Sterling, and Suess, 2007) which is equal to ϕ_{RC} in our case. Since ϕ_{RC} is proportional to AW , we do expect a better correlation between ϕ_{RC} and M_{cme}^t which further provides a good positive correlation between ϕ_{RC} and kinetic energy of associated CMEs (KE_{cme}) measured using mass, M_{cme}^t and V_{gcs} . In Figure 2.7(c), we show the correlation between ϕ_{RC} and KE_{cme} . We find $r=0.68$ at 99.9% confidence level and derive the regression equations of the least-squares fits (see Figure 2.7). The correlation coefficient and the slope of fitted regression line are very similar to that obtained by Gopalswamy et al. (2017b) for cycle 23. The significant correlation between KE_{cme} and ϕ_{RC} confirms that ϕ_{RC} is a good indicator of CME kinetic energy. The acceleration of CMEs is mainly driven by the Lorentz force component representing the magnetic pressure gradient and a diamagnetic effect that comes from the induced eddy current at the solar surface (Green et al., 2018; Schmieder,

Aulanier, and Vršnak, 2015). The acceleration is limited by the inductive decay of the electric current that implies the decrease of Lorentz force and the free energy contained in the system (Vršnak, 2016; Chen and Kunkel, 2010). In our study, the positive correlation found between KE_{cme}^L and ϕ_{RC} suggests that the reconnected field lines cause a rapid energy deposition in corresponding CME flux ropes. Here ϕ_{RC} serves as a proxy for reconnected magnetic field intensity.

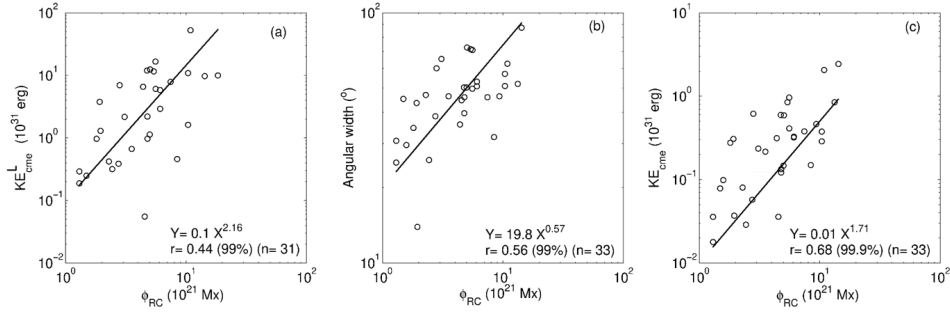


Figure 2.7: Scatter plots between ϕ_{RC} and (a) KE_{cme}^L , (b) angular width (AW), and (c) KE_{cme} . The correlation coefficients (r) mentioned in each plot suggest a significant positive correlation between each of the CME parameters and ϕ_{RC} . The solid black lines are the least-squares fits to the plots. The regression equations are mentioned in the plots.

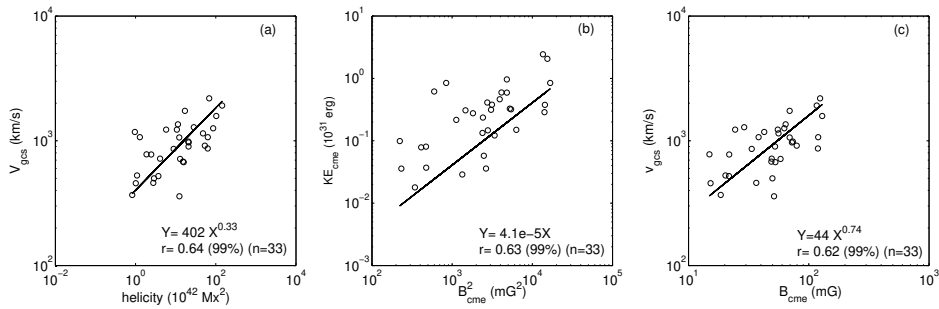


Figure 2.8: Scatter plots between (a) V_{gas} and H_m , (b) KE_{cme} and B_{cme}^2 , and (c) V_{gas} and B_{cme} of CME flux ropes at $10 R_s$. The straight line in each plot shows the linear least-squares fit to the data. The correlation coefficients (r) along with the equations of the regression lines are mentioned in each plot.

2.3.2 Kinetic properties versus magnetic properties of CMEs

In Figure 2.8(a), (b) and (c), we study the relationship between CME kinematics (velocity and kinetic energy) and intrinsic CME magnetic properties (B_{cme} , magnetic pressure (B_{cme}^2), and H_m). According to the FRED technique, the axial magnetic field strength B_{cme} of the flux rope depends on its geometric parameters (from the GCS model) and ϕ_{RC} under the assumption that the CME flux rope is force-free (Gopalswamy et al., 2017b; Gopalswamy et al., 2017c). We derive B_{cme} as well as H_m at $10 R_s$ from ϕ_{RC}^p and statistically establish a positive correlation between H_m and V_{gcs} (shown in Figure 2.8(a)), B_{cme}^2 and KE_{cme} (shown in Figure 2.8(b)) as well as B_{cme} and V_{gcs} (shown in Figure 2.8(c)). The correlation coefficients are respectively 0.64, 0.63, and 0.62 at 99% confidence level. The correlations suggest that CME flux ropes with higher magnetic field strength and helicities tend to have higher speeds and energies – which is not unexpected because the CME kinematics is governed by the free magnetic energy contained in its current carrying sheared and twisted magnetic field structure (Vršnak, 2008). We find that at a radial distance (R_{rad}) of $10 R_s$, the average magnetic pressure of a CME flux rope is an order of magnitude greater than the background magnetic pressure (B_{bg}^2) computed using $B_{bg}(R_{rad}) = 0.356R_{rad}^{-1.28}$ for an adiabatic index of 5.3 (Gopalswamy and Yashiro, 2011). This plausibly explains our observations that CME flux ropes with large magnetic content expands faster through the interplanetary medium (Gopalswamy et al., 2014).

2.4 Discussion

We investigate the dependence of the initial speed of CMEs on the magnetic properties of their source ARs, reconnection flux of associated eruptive event, and the intrinsic magnetic characteristics of the CME flux rope. We measure the proxies of AR size (i.e., ϕ_{AR}), nonpotentiality (i.e., I_{tot} , ρ_{tot} , and L_{nl}) and find a weak positive correlation ($r \approx 0.5$) between CME speed and the measured AR parameters. Gopalswamy (2017d) pointed out that the magnetic reconnection flux (ϕ_{RC}) is typically smaller than the total unsigned magnetic flux (ϕ_{AR}) of an AR. For our events, we find the average ratio of ϕ_{RC} and ϕ_{AR} as 0.3. The value of ϕ_{RC}/ϕ_{AR} suggests

that only a smaller section of the active region is involved in a given eruption. This fact might be the main reason for a weak positive correlation between CME speeds and associated global, source AR parameters.

Tiwari et al. (2015) studied 189 CMEs to investigate the relationship between CME speed and their sources. The study did not find any correlation between the projected CME speed and the global area and nonpotentiality of their sources. Kim et al. (2017) studied 22 CMEs of solar cycle 24 and examined the relationship between the CME speed, calculated from the triangulation method and the average magnetic helicity injection rate ($|\dot{H}_{avg}|$) and the total unsigned magnetic flux [$\phi(t_f)$]. They classified the selected events into two groups depending on the sign of injected helicity in the CME-productive ARs. For group A (containing 16 CMEs for which the helicity injection in the source ARs had a monotonically increasing pattern with one sign of helicity), the correlation coefficient for CME speed and $|\dot{H}_{avg}|$ was found to be 0.31, and for CME speed and $\phi(t_f)$ it was 0.17. Whereas, for group B (containing only 6 CMEs for which the helicity injection was monotonically increasing but followed by a sign reversal), the correlation coefficient for CME speed and $|\dot{H}_{avg}|$ was found to be -0.76 and for CME speed and $\phi(t_f)$ it was 0.77. Although the correlation coefficients are high for group B events, they are not statistically significant (as the number of events is minimal for group B).

Qiu and Yurchyshyn (2005) studied ϕ_{RC} of 13 CME source regions of varying magnetic configurations and found a strong correlation (with a linear correlation coefficient of 0.89 at greater than 99.5% confidence level) between CME plane-of-sky speeds and associated ϕ_{RC} . The study also suggested that the kinematics of CMEs is probably independent of magnetic configurations of their sources. Miklenic, Veronig, and Vršnak (2009) combined ϕ_{RC} and linear speed of five CME events analyzed in their study with those from the other events derived by Qiu and Yurchyshyn (2005), Qiu et al. (2007), and Longcope et al. (2007) and found a significant correlation ($r=0.76$) with a confidence level greater than 99%. Our result confirms both Qiu and Yurchyshyn (2005) and Miklenic, Veronig, and Vršnak (2009) with better statistics. In our study, the linear correlation coefficient between ϕ_{RC} and V_{gcs} is found as 0.66 (99.99%). The accuracy of our findings is expected to be better as we consider the deprojected speed of CMEs and vector magnetograms

of ARs to calculate the ϕ_{RC} of CME sources. The mean relative error for ϕ_{RC} is estimated from the average error of ϕ_{AR} over the pixels above the noise level. The error is inferred to be 5% in our dataset. We also consider the uncertainty in V_{gcs} . Thernisien, Vourlidas, and Howard (2009) found that the mean uncertainty involved in obtaining the height of CME using the GCS model is 0.48 Rs. We consider this uncertainty into the linear fitting process to estimate the error involved in V_{gcs} calculation. We find a mean relative error of 12.4% for the V_{gcs} of our events. The estimated error is quite similar to what Shen et al. (2013) found in measuring the deprojected propagation speed of 86 full Halo CMEs using the GCS model.

A recent study by Gopalswamy et al. (2017b) found a significant positive correlation ($r= 0.6$ at 99.99%) between the speed of 48 CMEs that have signatures in interplanetary medium (in the form of magnetic clouds and non-cloud ejectas) and associated ϕ_{RCS} . It must be noted that for the study they used the Krall and Cyr (2006a) flux rope model and deprojected speed of CMEs from the flux rope fit. They used CME observations from a single view (SOHO/LASCO) compared to the multi-view observations used in our study. In Figure 2.9, we compare the reconnection flux-CME speed relation between the events of solar cycle 23 and 24. The reconnection flux and CME speed information of the events of cycle 23 are taken from Gopalswamy et al. (2017b). The filled blue symbols in the Figure represent the events of cycle 24. We find similar slopes for both the regression lines representing the linear least square fits CME speed-reconnection flux pairs of the events of two different solar cycles. We combine the events of both the solar cycles and find the regression equation of the linear least square fit to the scatter plot of total 81 events (the associated regression line is shown in red colour in Figure 2.9). The relationship established from this combined and more statistically significant database is

$$V_{cme} = 355\phi_{RC}^p 0.69 km s^{-1}, \quad (2.10)$$

Here V_{cme} stands for the deprojected CME speed estimated from both the single view and multi-view observations and ϕ_{RC} is in 10^{21} Mx unit. The power-law relationship between ϕ_{RC} and V_{cme} depicted in Equation 2.10 has an exponent ≈ 0.7 . We note that Vršnak (2016) found a linear relationship between peak velocity of the

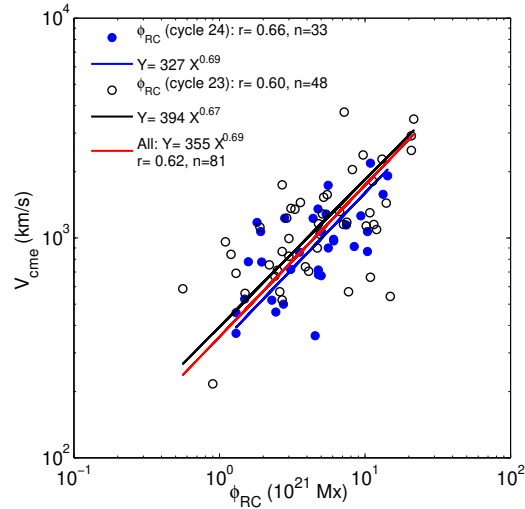


Figure 2.9: Scatter plot between CME speed and ϕ_{RC} of 33 events of solar cycle 24 and 48 events of solar cycle 23. Solar cycle 23 data is acquired from Gopalswamy et al. (2017b). The filled blue symbols represent the events of cycle 23. The black, blue and continuous red lines are the regression lines derived from least-squares fits to the scatter plot of the events of cycle 23, 24 and combined cycle 23-24 data, respectively. The corresponding regression line equations are depicted in the Figure.

eruption and the added flux to the erupting flux rope by the reconnection process.

We also find a significant positive correlation ($r \approx 0.6$ at 99% confidence level) between CME kinematics (i.e., speed and kinetic energy) and some of the magnetic properties of CMEs (i.e., magnetic field intensity, magnetic pressure, and magnetic helicity) at $10 R_s$. Gopalswamy et al. (2017b) studied the relationship between CME speed and its magnetic field intensity at $10 R_s$ for 48 CMEs and found a positive correlation with $r = 0.58$ (at 99.9% confidence level), which is similar to what we find. We study two additional magnetic parameters of CMEs (i.e., magnetic pressure and magnetic helicity) and find a good positive correlation between the parameters and the CME kinematics with a correlation coefficient of ≈ 0.64 at 99% confidence level.

2.5 Conclusions

In this study, we obtain the deprojected physical parameters of flux rope CMEs of solar cycle 24 and calculate their magnetic (azimuthal flux, axial magnetic field intensity, and magnetic helicity) and kinetic parameters (speed and kinetic energy).

Next, we measure the magnetic parameters of the associated source ARs and find the dependency of near-Sun CME kinematics on the AR magnetic parameters. We explain the basis of the relationship found between these parameters and also investigate the correspondence between the magnetic and kinetic properties of CMEs. The main conclusions of this study are:

1. The area and nonpotentiality of the entire source regions and the speed of associated CMEs are weakly correlated. The reason is probably the small average ratio (≈ 0.3) of reconnection flux during eruptions and the total flux in the source ARs. The smaller value of the flux ratio indicates that usually only a fraction of an AR involves an associated eruption.
2. The flare reconnection flux is a proxy of the reconnection energy associated with an eruptive event. In our study, we find a good correlation between CME kinematics (speed and kinetic energy) and reconnection flux with $r=0.66$ and 0.68 in case of CME speed and kinetic energy, respectively. The slope of the regression line fitted to the reconnection flux-CME speed pairs for the events of solar cycle 24 is 0.69 which is in agreement with that derived by Gopalswamy et al. (2017b) for the events of solar cycle 23. The regression equation for the combined 81 events of both cycle 23 and 24 can be further used as an empirical model for predicting the near-Sun speed of CMEs.
3. The magnetic content of a CME flux rope is well correlated with its velocity and kinetic energy. We find a good correlation between the magnetic pressure of CME and its kinetic energy. This relationship is evident from the fact that the rapid expansion of CME occurs due to the higher magnetic pressure of CME flux rope relative to that of the background magnetic field.
4. We find that CME speed increases with the coronal magnetic helicity carried by the CME flux rope.

Chapter 3

Investigating the origin of CME magnetic properties

Chapter Summary

To determine the geoeffectiveness of Earth-directed interplanetary coronal mass ejections (ICMEs) it is necessary to have proper understanding of origin and evolution of their magnetic properties. In the previous chapter we have studied the factors governing the CME kinematics. This chapter analyses the magnetic properties specifically magnetic flux and helicity of near-Sun and 1-AU flux ropes. We observe a significant positive correlation between the magnetic properties of near-Sun and 1-AU flux ropes. Our results show that the poloidal flux and helicity in 1-AU flux ropes are highly relevant to low-corona magnetic reconnection at the associated eruption site, and the toroidal flux of flux ropes is a fraction of the total reconnection flux. Our results are consistent with the fact that near-Sun helical flux ropes are majorly formed due to low-corona magnetic reconnection and the magnetic properties are transferred to the flux ropes during the magnetic reconnection process. This study connecting the magnetic properties of flux ropes through the Sun-Earth system has important implications for the origin of flux and helicity in the interplanetary medium and the topology of ICME flux ropes at 1 AU and hence their space weather consequences.

3.1 Introduction

Magnetic clouds (MCs) are a special kind of interplanetary manifestation of coronal mass ejections (CMEs) characterised by 1) a low proton temperature and a low proton beta compared to the typical solar wind, 2) an enhanced magnetic field strength and 3) a smoothly rotated magnetic field (Burlaga et al., 1981). The flux rope magnetic structure of MCs makes them a distinct subset of interplanetary coronal mass ejections (ICMEs). The characteristics of MCs are of great interest because about 90% of the observed MCs are responsible for driving geomagnetic storms with Dst_{min} (minimum Dst index observed in geomagnetic storm interval) ≤ -30 nT (e.g., Wu and Lepping, 2007; Wu and Lepping, 2008).

CMEs are generated due to the destabilization of coronal magnetic field structure, usually triggered by magnetic field evolution due to flux emergence, twisting, shearing and converging motions in the photosphere. Magnetic reconnection in the solar corona allows transferring the photospheric shear to the twisted magnetic flux rope (Low, 1996; Démoulin, Pariat, and Berger, 2006). The coronal flux rope thus formed becomes an MC after propagating through the interplanetary medium. Several studies have shown that all ICMEs have plausibly flux rope structure (Gopalswamy et al., 2013b; Marubashi et al., 2015), which is an important fact that can be used for space weather predictions. However only in situ observations of CMEs are not sufficient to conclude that flux rope configuration is present in all CMEs (Al-Haddad et al., 2011; Vourlidas et al., 2013).

The most important magnetic characteristics of CMEs are magnetic flux and helicity that describes how the magnetic flux tubes are twisted, linked and wounded around each other in a closed volume. In the solar atmosphere and heliosphere the magnetic flux and helicity are almost conserved (Berger and Field, 1984b). Theoretical considerations based on the conservation of magnetic helicity generate important constraints on flux tube dynamics in the solar convection zone and the tilt and twist of solar active regions (ARs; Nandy, 2006). Beyond the solar atmosphere, throughout the propagation of MCs in the interplanetary medium, the magnetic flux and helicity remain invariant in a closed volume unless they significantly reconnect with the surrounding interplanetary magnetic field (IMF). This approximation has been the basis of several studies that connect interplanetary flux ropes with their

solar sources (Dasso et al., 2005; Qiu et al., 2007; Cho et al., 2013; Hu et al., 2014).

The computation of magnetic flux and helicity of a flux rope requires the estimation of its geometry and axial magnetic field intensity (Démoulin et al., 2002; DeVore, 2000). Based on the observed data at 1-AU it is possible to analyze the MC geometry by fitting a cylindrical or a torus-shaped flux rope model. Thus the axial magnetic field strength can be estimated. Utilizing the geometry of the causative CME and its poloidal flux the helicity of the progenitor coronal flux rope can be measured. Several studies have shown that the low-coronal reconnection flux is almost equivalent to the azimuthal flux of the flux rope formed due to reconnection (Longcope and Beveridge, 2007; Qiu et al., 2007; Gopalswamy et al., 2017a). Gopalswamy et al. (2017a) devised a convenient method to compute the reconnection flux using the area under the post eruption arcade (PEA) and the photospheric flux threading through this area.

The main aim of this study is to compare the magnetic properties of MCs with their associated coronal flux ropes. In particular, the magnetic flux and helicity in the two domains are compared. For this study, we choose ten identified MC events having post eruption arcades as coronal signatures and line-of-sight and vector magnetograms. Next, we extract the geometrical and magnetic information of those MCs and their solar counterparts. Finally, we comment on the conservation of magnetic flux and helicity in the Sun-Earth system based on our study and reflect upon the major source of magnetic properties of CME flux ropes. In Section 3.2 we discuss the observations of ICMEs and their solar sources. Section 3.3 describes the method of analysis of ICMEs and associated solar sources. The results are discussed in Section 3.4 followed by summary and conclusions in section 3.5.

3.2 Observations

In this section we discuss on observations of ICME flux ropes, and identification of their associated CMEs and solar sources.

3.2.1 in situ observation of ICMEs at 1 AU

Figure 3.1 shows the in situ solar wind plasma and magnetic properties measured by the Advanced Composition Explorer (ACE) spacecraft (Stone et al., 1998) (http://www.srl.caltech.edu/ACE/ASC/level2/lv12DATA_MAG-SWEPAM.html) at L1 Lagrangian point along with the geomagnetic activity index (*Dst*) (http://wdc.kugi.kyoto-u.ac.jp/dst_final/index.html) during 17-18 March 2013 when one of the selected MCs crosses the spacecraft. Starting from the top, we plot the total IMF intensity (B), Y , Z components of IMF in Geocentric Solar Ecliptic (GSE) coordinate defined as B_y and B_z , solar wind plasma flow speed (V_{sw}), density (N_p), proton temperature (T_p), and plasma beta, computed based on protons, i.e., proton beta (β) with a 64-second time resolution and *Dst* with 1 hour time resolution. The dashed curves over-plotted on T_p represent the temperature (T_{ex}) expected from the correlation between V_{sw} and T_p (Lopez, 1987). The horizontal dashed line over-plotted on β stresses the distinct value, $\beta=1$.

A sudden enhancement of V_{sw} , N_p , T_p and B implies that an ICME arrives with an interplanetary (IP) shock at 05:30 UT on 17 March 2013 (marked by a dotted vertical line in Figure 3.1.) The observed shock velocity is 751 km/s. A sheath region with a high fluctuation of IMF vectors is present after the IP shock. The peak value of the IMF intensity and the minimum value of its z component (B_z) in this region are respectively 22.1 nT and -18.5 nT. After the sheath region, a decrease in T_p compared to T_{ex} , β with value less than 1, constant westward (negative) B_y and south to north (negative to positive) smooth rotation of B_z with strong magnetic field strength confirms that a small inclination bipolar (south-north) magnetic cloud (Gonzalez, Lee, and Tsurutani, 1990; Li and Luhmann, 2004) passes through L1. Moreover, the decrease in T_p compared to T_{ex} is only present close to the beginning and at the end of the MC. Within the identified boundaries, T_p is not below T_{ex} during some interval, although β is < 1 . However, the speed has the declining profile indicative of MC expansion; the B_y component shows the MC axis points to the west, while the B_z component shows rotation from south to north. Consistent with the Burlaga et al. (1981) definition the MC starts at 14:39 UT (marked by the red vertical line) and ends at 00:44 UT on 18 March (marked by the blue vertical line). We note that the rear boundary is well defined in this

case, indicated by the discontinuities in the total magnetic field and solar wind speed. However, it must be noted that frequently the MC boundaries are not well defined. The duration of the MC is about 10 hr, which is $\approx 48\%$ smaller than the average duration of solar cycle 24 MC at 1 AU, $\Delta t_{mc} = 19.19$ hr (Gopalswamy et al., 2015a). The peak field strength and the minimum value of B_z during MC interval are recorded as 13.4 nT and -10.6 nT, respectively. The ICME resulted in a classic double-dip, major geomagnetic storm (Kamide et al., 1998) due to southward IMF in the sheath, and MC. The minimum value of Dst is -100 nT during the sheath and -134 nT during the MC.

3.2.2 Identification and observation of ICME solar sources

To identify the solar source of an ICME, we use observations from different instruments on the Solar and Heliospheric Observatory (SOHO) and Solar Dynamic Observatory (SDO) missions. The Large Angle and Spectrometric Coronagraph (LASCO) telescope's C2 and C3 on board SOHO observe the CME near the Sun. The fields of view of C2 and C3 (Brueckner et al., 1995) are respectively 2 – 6 and 4 – 30 R_s measured in units of solar radius from the disk center of the Sun. We use the LASCO CME catalog (http://cdaw.gsfc.nasa.gov/CME_list/) (Yashiro et al., 2004; Gopalswamy et al., 2009) to identify the MC-associated CMEs. To analyze the structure of identified source CMEs, we use the observations from the Sun Earth Connection Coronal and Heliospheric Investigation (SECCHI, Howard et al., 2008) COR2 A & B on board the Solar Terrestrial Relations Observatory (STEREO) mission along with the LASCO images. We study the solar sources of MC-associated CMEs by using SDO's Atmospheric Imaging Assembly (AIA) (Lemen et al., 2012) images at 193 Å, Helioseismic Magnetic Imagers (HMI) (Scherrer et al., 2012) line-of-sight (LOS) magnetograms and the Space-Weather HMI AR Patch (SHARP) (Bobra et al., 2014) vector magnetograms.

We identify the CMEs associated with the ICMEs in question by following the procedure described in Zhang et al. (2007). As an example, below we provide a brief description of the procedure applied to identify the CME associated with the ICME observed on 17-18 March 2013. We consider the solar wind speed at shock arrival (757 km/s) as the transit speed of the CME-driven shock travels from the Sun to

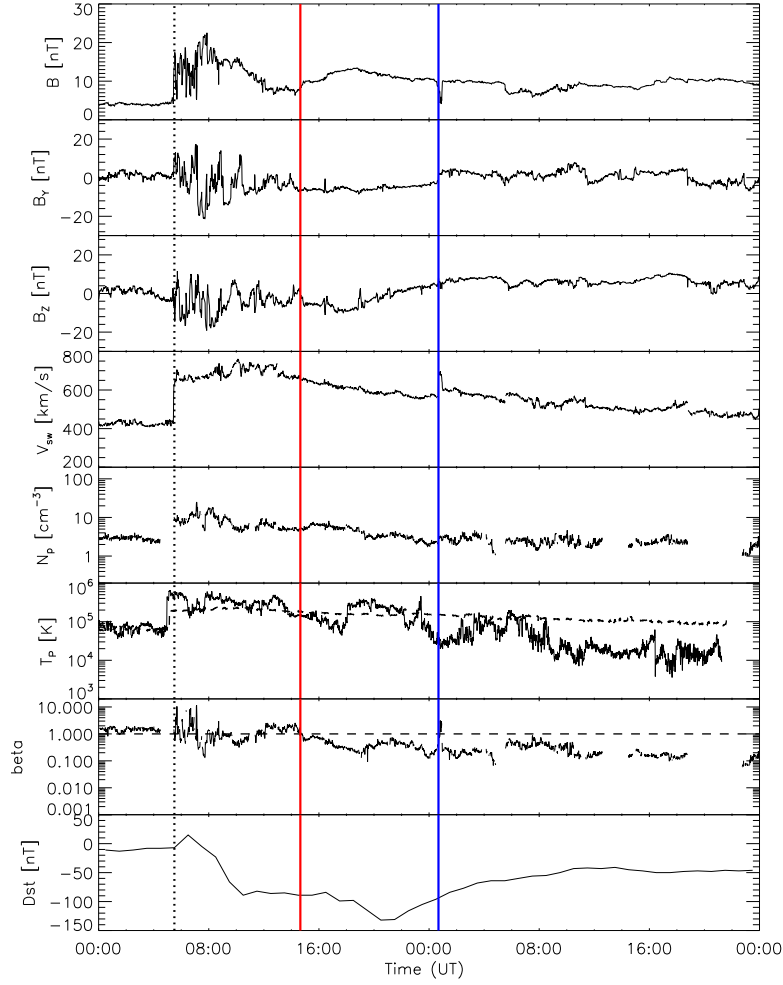


Figure 3.1: Solar wind data along with geomagnetic storm index (Dst) during 17-18 March 2013. The parameters plotted (from top to bottom) are the total IMF intensity (B in nT), y component of IMF (B_y in nT), z component of IMF (B_z in nT), solar wind plasma flow speed (V_{sw} in km/s), proton density (N_p in cm^{-3}), proton temperature (T_p in K), proton beta (beta) and Dst index in nT. The dashed curve over-plotted on T_p represents T_{ex} and the horizontal dashed line on beta points the value, beta=1. The black (dotted), red and blue vertical lines indicate the shock arrival, start and the end boundary of MC, respectively.

the Earth and estimate the transit time as ≈ 54 hrs, suggesting that the associated CME should start only after 00:00 UT of 15 March 2013. By searching the LASCO CME catalog for frontside wide CMEs during the transit time interval we find only one CME originating close to the disk center in the LASCO/C2 FOV at 07:12 UT on 15 March 2013. It has a high projected speed of 1063 km/s consistent with

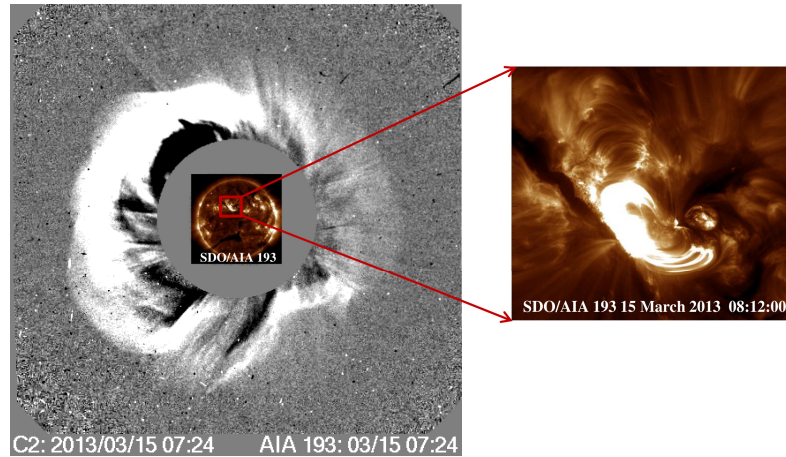


Figure 3.2: The 15 March 2013 CME in LASCO/C2 difference image (left) with PEA as a coronal signature shown in an SDO/AIA image at 193 Å (right).

the fast ICME. The CME is associated with an M1.1 GOES soft X-ray flare that initiated at 05:46 UT on 15 March. The CME leaves behind a PEA as an apparent coronal feature observed by SDO/AIA at 193 Å during the decay phase of the long duration flare. Thus we identify the source location of the CME as N11E12 which corresponds to the NOAA AR 11692. In Figure 3.2 we show the running difference image of the associated CME observed by LASCO/C2 along with the PEA in solar corona observed by SDO/AIA at 193 Å.

3.3 Methodology

3.3.1 Analysis of ICME data

To understand the structure and magnetic nature of ICME flux ropes, we use a constant- α (linear) force-free cylindrical flux rope model with self-similar expansion, which was proposed by Farrugia et al. (1992) and Farrugia et al. (1993) with a modification based on Shimazu and Vandas (2002). Following Marubashi and Lepping (2007), we perform the fitting of the model during the interval, when the magnetic field rotates smoothly in the Y-Z plane, proton temperature and proton beta decrease from their average values, He^{++}/H^+ value increases, proton number density decreases, and the fluctuation in the ratio of standard deviation to the mean magnetic field intensity (S_b/B) is relatively small. Figure 3.3 shows the solar wind data during 17-18 March 2013 with the cylindrical model fitting results. From top

to bottom we plot B , B_x , B_y , B_z , S_b/B , V_{sw} , N_p , T_p , beta, and vector plots of the magnetic field projected on X-Y, X-Z, and Y-Z plane in 30-min average. The vertical solid lines in the Figure denote the start and end times of the cloud. The red curves over-plotted on B , B_x , B_y , B_z and V_{sw} represent the fit. T_{ex} is over-plotted on T_p in a dashed curve. Table 3.1 lists the best fit parameters of the MC observed on 17-18 March 2013. The parameters are latitude (θ_{mc}) and longitude angles (ψ_{mc}) of the axial magnetic field, axial field strength (B_{0mc}), radius (R_{0mc}) of the fitted cylinder, handedness of the twisted field (D) of the cloud, and impact parameter (p) in Column 1-6. The impact parameter is the distance between the spacecraft trajectory and the MC axis normalized to the MC radius. Column 7 shows the relative error of the fitting (E_{rms}). The E_{rms} is the ratio of Δ and the maximum observed magnetic field intensity, B_{max} . Here Δ is the rms deviation between the observed magnetic field, $B(t_i)$, and the model magnetic field, $B^M(t_i)$ ($i = 1, \dots, N$).

Figure 3.4 depicts the geometry of the particular MC at the time of encounter with spacecraft. In this Figure arrow ‘A’ indicates the axis of the MC flux rope, arrow ‘S’ shows the direction of the poloidal magnetic field and arrow denoted by ‘S/C’ demonstrates the path of spacecraft. It is observed from the Figure that the spacecraft comes across the MC near its flank and far below from its axis.

Calculation of cloud’s magnetic parameters

In this section we compute MC unsigned flux and magnetic helicity (H_{mc}) using Lundquist’s constant- α force-free field solution in cylindrical coordinates (Lepping, Burlaga, and Jones, 1990). The solution provides axial magnetic field component, $B_{ax} = B_0 J_0(\alpha r)$, poloidal (azimuthal) magnetic field component, $B_{az} = DB_0 J_1(\alpha r)$ and radial field component, $B_r = 0$. Where B_0 is the axial magnetic field strength, $D = \pm 1$ is the flux rope handedness (plus for right handed and minus for left handed), J_n is the n^{th} order Bessel function and $\alpha = x_{01}/R_{0mc}$ is the twist per unit length, where $x_{01} = 2.4048$ is the location of the first zero of J_0 .

The magnetic flux is defined as

$$\phi = \int B dA \quad (3.1)$$

using cylindrical symmetry, $dA = 2\pi r dr$.

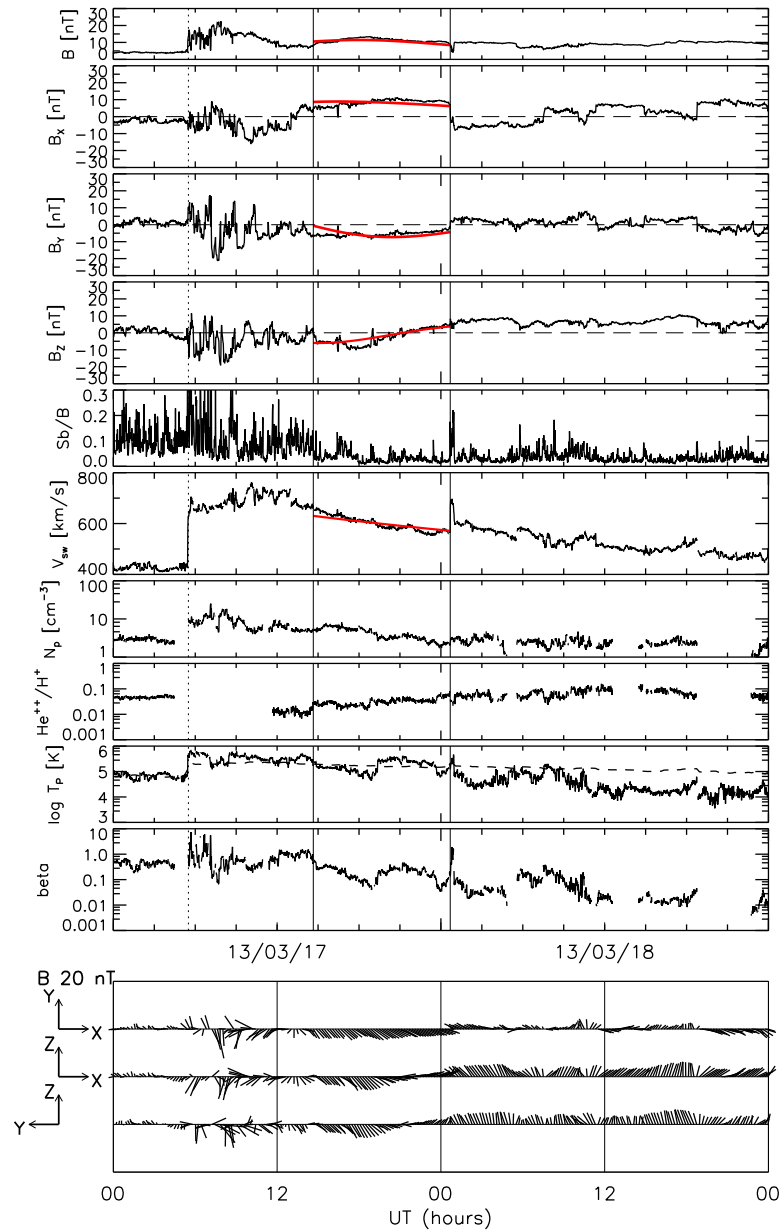


Figure 3.3: Results of the fitting with cylindrical flux rope model (red curve superimposed on the observed solar wind parameters) to the MC observed on 17-18 March 2013. The continuous vertical lines show the front and end boundary of the MC. The vertical dotted line indicates the time of shock arrival. The magnetic field vectors projected on the X-Y, X-Z, and Y-Z planes are shown at the bottom.

The axial and poloidal components of magnetic flux (ϕ_z & ϕ_p) in a cylindrical flux rope is given by (e.g., Leamon et al., 2004; Qiu et al., 2007),

$$\phi_z = 2\pi \int_0^{R_0} B_{ax} r dr = \frac{2\pi J_1(x_{01})}{x_{01}} B_0 R_0^2 \quad (3.2)$$

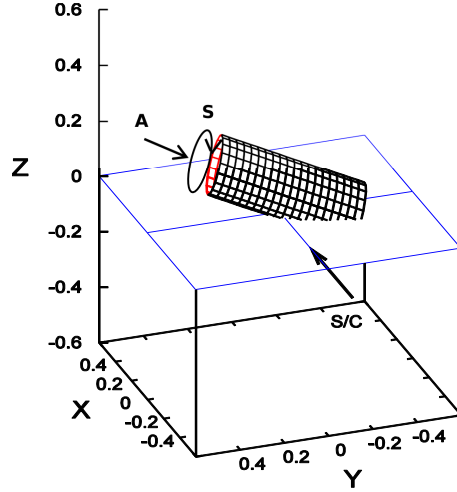


Figure 3.4: Geometry of the 17-18 March 2013 MC obtained from fitting data. Three directions indicated in Figure are axial field direction (A), direction of the poloidal magnetic field (S) and spacecraft trajectory (S/C).

and

$$\phi_p = L \int_0^{R_0} B_{az} r dr = \frac{L}{x_{01}} B_0 R_0, \quad (3.3)$$

where R_0 , B_0 and L is respectively the radius, axial magnetic field strength and length of cylindrical flux rope.

Within a volume V the magnetic helicity H of a field B is defined by,

$$H = \int_V \mathbf{A} \cdot \mathbf{B} dV, \quad (3.4)$$

where \mathbf{A} is the vector potential. This definition of helicity is meaningful only if the normal component of B (B_n) at any surface S surrounding the volume V is zero, i.e., $B_n = 0$. In case of $B_n \neq 0$, relative magnetic helicity (H_r) is derived by subtracting the reference magnetic field (B_{ref}) helicity from H (Berger and Field, 1984b). Thus, H_r is defined by,

$$H_r = \int_V \mathbf{A} \cdot \mathbf{B} dV - \int_V \mathbf{A}_{ref} \cdot \mathbf{B}_{ref} dV \quad (3.5)$$

Here H_r is gauge-invariant if $\mathbf{A} \times \hat{n} = \mathbf{A}_{ref} \times \hat{n}$ on S of V . For a cylindrical flux tube, B_{ref} can be chosen as $B_{ref} = B_z \hat{u}_z$ and $B = B_\theta \hat{u}_\phi + B_z \hat{u}_z$. Considering $\mathbf{A} = B/\alpha$, we compute the magnetic helicity of cylindrical flux rope (Berger, 2003; Dasso et al., 2003; Démoulin et al., 2002; DeVore, 2000) as,

$$H = 4\pi L \int_0^{R_0} A_\theta B_\theta r dr = \frac{4\pi B_0^2 L}{\alpha} \int_0^{R_0} J_1^2(\alpha r) r dr \approx 0.7 B_0^2 R_0^3 L \quad (3.6)$$

To derive the axial and poloidal components of MC flux (ϕ_{zmc} and ϕ_{pmc}) and the magnetic helicity (H_{mc}) of the MC we apply $B_0 = B_{0mc}$, $R_0 = R_{0mc}$ and $L = L_{mc}$ in Equation 3.2, 3.3 and 3.6. Here L_{mc} is the estimated length of the MC.

The largest uncertainty in calculating the flux and helicity of an MC arises from the MC flux rope length approximation. Larson et al. (1997) estimated the length of MC as 2.5 AU by measuring the travel time of suprathermal electrons moving along with the twisted magnetic field lines. The presence of bidirectional electrons in MCs observed at 1 AU suggests the possibility of MCs rooted on the Sun when they reach at 1 AU (Shodhan et al., 2000). We consider the MC a half torus that has a circular cross section as an approximation to the expanded flux rope, extending from Sun to Earth. Then the length of MC at 1 AU is π AU if the major axis length of the torus is 1 AU. We note that the length is only 21% higher than the statistical value (2.6 ± 0.3 AU) reported in Démoulin, Janvier, and Dasso (2016). In column 8 to 11 of Table 3.1, we show the twist density (α_{mc}) of the magnetic field in MC flux rope, ϕ_{zmc} , ϕ_{pmc} and H_{mc} corresponding to different L_{mc} s for the MC observed on 17-18 March 2013.

Table 3.1: The fitting parameters and derived quantities of the MC observed on 17-18 March 2013.

θ_{MC}	ψ_{MC}	B_{0mc}	R_{0mc}	D	p	E_{rms}	α_{mc}	ϕ_{zmc}	ϕ_{pmc}	H_{mc}				
($^{\circ}$)	($^{\circ}$)	(nT)	(AU)		(R_{0mc})		(Gm^{-1})	(10^{21} Mx)	(10^{21} Mx)	(10^{42} Mx ²)				
(1)	(2)	(3)	(4)	(5)	(6)	(7)	(8)	(9)	(10)	(11)				
								$\phi_{pmc}^{L2(b)}$	$\phi_{pmc}^{L2.5(c)}$	$\phi_{pmc}^{L\pi(d)}$	$H_{mc}^{L2(e)}$	$H_{mc}^{L2.5(f)}$	$H_{mc}^{L\pi(g)}$	
-24.4	247.8	20.30	0.12	$R^{(a)}$	0.87	0.23	0.14	0.82	4.37	5.46	6.86	4.47	5.58	7.01

(a) 'R' stands for Right handed rotation of magnetic field.

(b) ϕ_{pmc} derived using $L_{mc} = 2$ AU

(c) ϕ_{pmc} derived using $L_{mc} = 2.5$ AU

(d) ϕ_{pmc} derived using $L_{mc} = \pi$ AU

(e) H_{mc} derived using $L_{mc} = 2$ AU

(f) H_{pmc} derived using $L_{mc} = 2.5$ AU

(g) H_{mc} derived using $L_{mc} = \pi$ AU

3.3.2 Analysis of ICME associated solar sources

In this subsection, using geometrical parameters of erupted flux ropes along with the reconnected flux in their eruption regions we compute the magnetic properties of flux ropes near the Sun. The geometrical properties are obtained by forward modelling white-light CMEs using GCS model.

Deriving magnetic properties of associated CMEs

Gopalswamy et al. (2017b) showed that the magnetic properties of coronal flux ropes can be obtained by combining reconnection flux and geometric properties obtained from flux rope fits to white-light data. Gopalswamy et al. (2017b) used the Krall and St. Cyr (2006) flux rope model to obtain the geometrical properties of coronal flux ropes. Here we fit CMEs with the forward modeling technique, Graduated Cylindrical Shell (GCS) model developed by Thernisien, Howard, and Vourlidas (2006) because three views are available from STEREO and SOHO. Thus we get the half angular width (γ), aspect ratio (κ), height of the leading edge (h), tilt angle (λ) with respect to the equator and the propagation longitude (ψ) and latitude (θ) of CMEs. From these results, we calculate the radius (R_{0cme}) of CME's circular annulus at its leading edge point using the relation, $R_{0cme}/h = 1/(1+(1/\kappa))$ derived using Equation 1 in Thernisien, Howard, and Vourlidas (2006) and 3-D speed from the time evolution of CME leading edge. In Figure 3.6, we show an example of fitting the GCS model to a CME flux rope that is associated with the 17-18 March 2013 ICME using the green wire frame over-plotted on the white-light CME, observed by LASCO/C3, and SECCHI/COR2 A & B around the same time. The CME is a halo CME observed from LASCO/C2 coronagraph at 05:12 UT on 15 March 2013. It appears as a flux rope like structure at 08:08 UT in the field of view of SECCHI/COR2 A & B

We estimate the axial magnetic field strength (B_{0cme}) of CMEs from its poloidal flux component (ϕ_{pcme}) by taking $\phi_p = \phi_{pcme}$, $L = L_{cme}$ (length of CME flux rope from the photosphere) and $R_0 = R_{0cme}$ in Equation 3.3. Thus, B_{0cme} can be defined as,

$$B_{0cme} = \frac{\phi_{pcme} x_{01}}{L_{cme} R_{0cme}} \quad (3.7)$$

Here L_{cme} is estimated from GCS model and can be computed as, $L_{cme} = 2h_{leg} + y(h - h_{leg}/\cos\gamma)/2 - 2R_{\odot}$, where h_{leg} is the height of the legs of a CME flux rope computed using Equation 3 in Thernisien, Howard, and Vourlidas (2006), $r_{arc} = (h - h_{leg}/\cos\gamma)/2$ is the radius of the arc of a flux rope, $y = 2(\pi/2 + \gamma)$ is the arc angle in radians and R_{\odot} represents the solar radius. In Figure 3.5, the face-on view of the cross-section of a croissant flux rope structure is shown, where the dash-dot line indicates the axis of the flux rope. Longcope et al. (2007) demonstrated

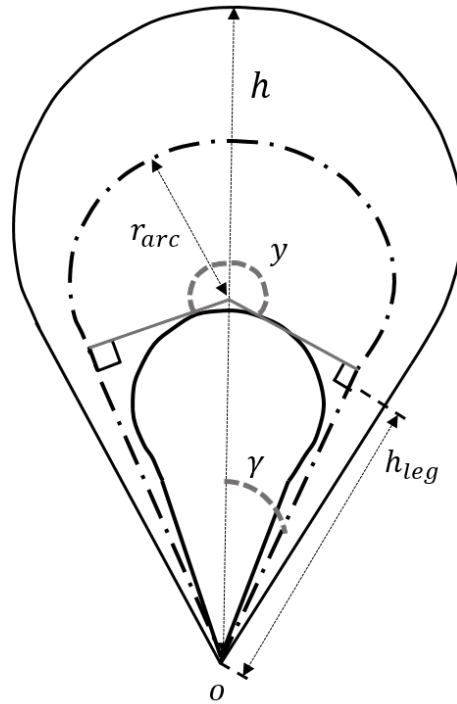


Figure 3.5: The face-on view of the cross-section of a croissant flux rope. The ‘o’ represents the center of the sun. The leading edge height, radius of the arc, arc angle, height of the leg, and half angular width are indicated using h , r_{arc} , y , h_{leg} , and γ .

that ϕ_{pcme} is approximately equal to the magnetic reconnection flux (ϕ_{RC}) in the low corona. Gopalswamy et al. (2017a) proposed a process to estimate the reconnection flux considering the half of the unsigned photospheric flux underlying the area occupied by the PEA (as discussed in the next section).

In Equation 3.6 we use $B_0 = B_{0cme}$, $R_0 = R_{0cme}$ and $L = L_{cme}$ to obtain the magnetic helicity (H_{cme}) of a CME flux rope. In Table 3.2 we present the GCS fitting results of 15 March 2013 CME along with R_{0cme} at $10 R_s$ ($R_{0cme}^{10R_s}$), L_{cme} and

3-D speed (V_{cme}^{3D}) of the CME estimated from the fitting.

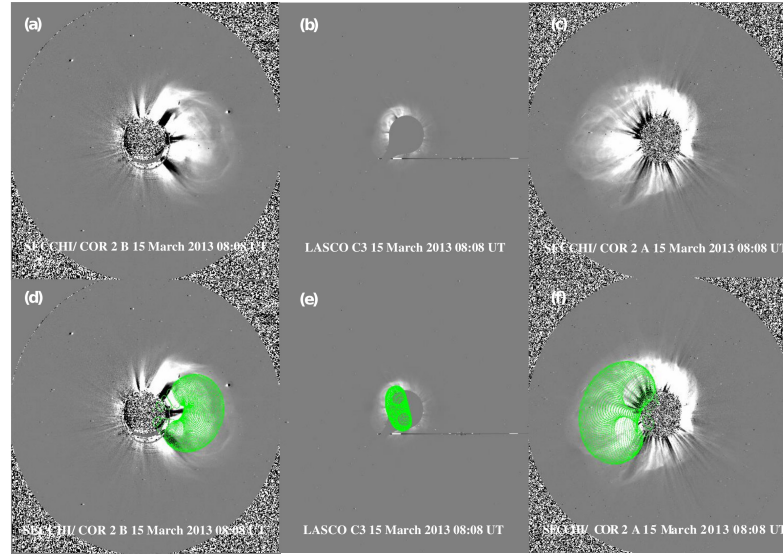


Figure 3.6: GCS model fitting on 15 March 2013 CME in LASCO/C3, SECCHI A & B data. (a), (b) and (c) are observed images of the CME by STEREO and LASCO. (d), (e) and (f) show the CME with the GCS wire frame overlaid on it.

The photospheric source active regions

To analyze the source active regions of ICMEs we consider the SDO/HMI LOS photospheric magnetograms together with the SDO/AIA 193 Å images and the solar X-ray imager aboard the Geostationary Operational Environmental Satellite (GOES) system (Hill et al., 2005), which spatially maps soft X-ray emission of solar corona. We calculate the reconnection flux at the decay phase of associated flares (when the post eruption arcades are almost matured) by using SDO/HMI LOS, AIA 193 Å data and GOES SXI data. We identify the post eruption arcade (PEA) regions in both AIA 193 Å and GOES SXI images, find the pixels associated with the area of arcades and overlay it on HMI LOS data. Considering B_{LOS} and the area of each of those pixels from HMI LOS data we derive the total reconnection flux (ϕ_{RC}) using the equation (Gopalswamy et al., 2017a),

$$\phi_{RC} = \frac{1}{2} \int_{PEA} |B_{LOS}| dA \quad (3.8)$$

To estimate the uncertainty in the arcade area measurement, we consider a range of arcade area (A_{PEA}). We derive the upper and lower limits of the range by

Table 3.2: An example of CME parameters determined by GCS model fitting on 15 March 2013 CME.

CME properties	Values
(1)	(2)
ψ_{cme} (Carrington coordinate)	68.82°
θ_{cme} (Carrington coordinate)	-6.15°
γ	25.16°
λ	-74.35°
κ	0.27
$R_{0cme}^{10R_s}$	2.13 R_s
L_{cme}	17.07 R_s
V_{cme}^{3D}	1321
	km/s

selecting the arcade footpoints in GOES SXI and AIA 193 Å images. The X-ray imager has a broader temperature response than the EUV image at a particular wavelength. In Figure 3.7(a) and (b), we show the estimated arcade footpoints in red and blue lines superposed on AIA 193 Å and GOES SXI images associated with 15 March 2013 eruption, respectively. In Figure 3.7(d) we overlay the footpoints derived from AIA 193 Å and GOES SXI images on the differential-rotation corrected HMI LOS magnetogram in their respective colors (time of available HMI data just at the beginning of the flare). In Figure 3.7(c) we show the ribbon structures by arrows in AIA 1600 Å image around 7:35 UT. Figure 3.7(e) shows the temporal evolution of GOES X-ray flare intensity. The solid vertical lines a, b, and d on the plot indicate the epochs of measuring arcade in AIA 193 Å, SXI, and HMI LOS magnetogram. The vertical line c indicates the time when a faded ribbon structure is shown in AIA 1600 Å image. The shaded interval between the dotted vertical line and the line, c shows an SDO data gap. Due to the absence of SDO/AIA observations during the impulsive phase of the co-produced flare, it is not possible to analyze ϕ_{RC} using flare ribbon method as in Kazachenko et al. (2017). In principle, one expects an overestimate of the area of the PEA (and hence ϕ_{RC}) if the ribbons start at a finite

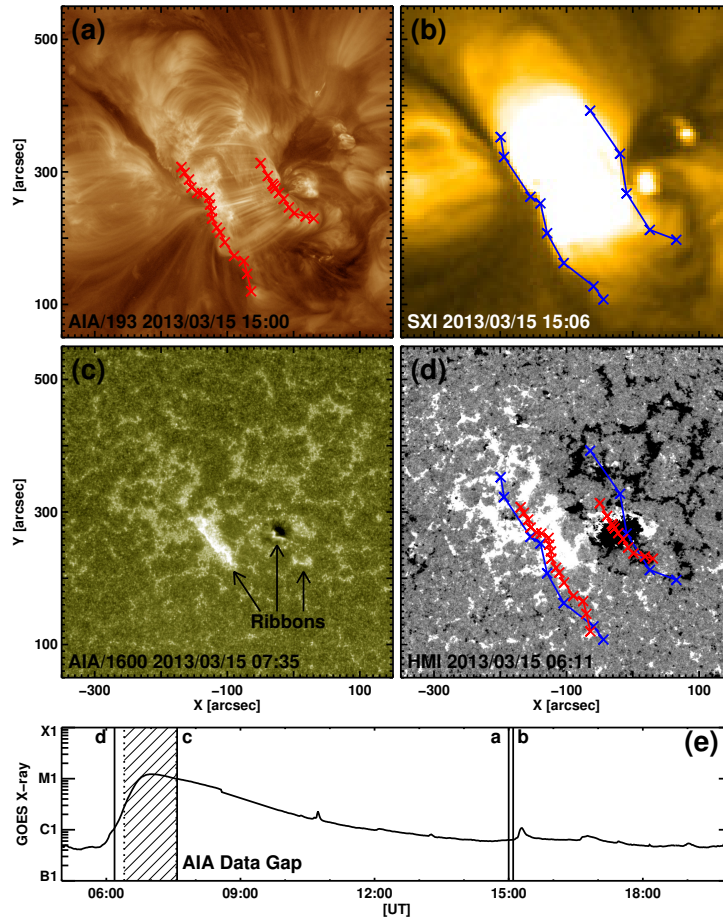


Figure 3.7: The post eruption arcade, flare ribbon, source magnetogram and flare evolution during 15 March 2013 eruption. (a) SDO/AIA 193 Å image of low corona showing post eruption arcade footpoints in red. (b) The PEA observed in GOES SXI and identified footpoints in blue. (c) Flare ribbon structure in SDO/AIA/ 1600 Å image. (d) HMI LOS photospheric magnetogram with overlaid arcade footpoints derived from both AIA and SXI data, and (e) GOES soft x-ray curve in the 1-8 Å band showing temporal evolution of the M1.1 flare associated with the eruption. The vertical lines marked by a, b, c and d are denoting the epochs when AIA 193 Å, SXI, AIA 1600 Å and HMI LOS data are taken. The shaded region between the dotted line and the vertical line, c defines SDO data gap. The ϕ_{RC} associated with AIA arcade is 4.10×10^{21} and with SXI arcade is 6.55×10^{21} Mx.

distance from the polarity inversion line (PIL). However, Gopalswamy et al. (2017a) considered this issue using events that had both ribbon and PEA data and found no evidence of overestimate. Another possible uncertainty in ϕ_{RC} is in identifying the boundaries of PEAs: the PEA is identified in the corona, but superposed on

the photosphere. This was also considered by Gopalswamy et al. (2017a) and found that the difference is not significant because ribbon and arcade methods give the same value. However, there may be other uncertainties when the arcade appears differently in EUV and X-ray images. This is explicitly shown in Figure 3.7: the AIA arcade has a smaller area than the SXI area giving a 37% lower ϕ_{RC} .

Using the reconnection flux limits, we derive a range of B_{0cme} at $10 R_S$ ($B_{0cme}^{10R_s}$) and H_{cme} . In Table 3.3, we show the upper and lower limits of A_{PEA} (A_{PEA}^u & A_{PEA}^l), ϕ_{RC} (ϕ_{RC}^u & ϕ_{RC}^l), $B_{0cme}^{10R_s}$ ($B_{0cme}^{10R_s^u}$ & $B_{0cme}^{10R_s^l}$), and H_{cme} (H_{cme}^u & H_{cme}^l) associated with the 15 March 2013 CME.

Table 3.3: Magnetic parameters of 15 March 2013 CME and its source AR derived using HMI LOS, AIA 193 Å and GOES SXI data.

A_{PEA}		ϕ_{RC}		$B_{0cme}^{10R_s}$		H_{cme}	
(10 ¹⁹ cm ²)		(10 ²¹ Mx)		(mG)		(10 ⁴² Mx ²)	
(1)		(2)		(3)		(4)	
A_{PEA}^l	A_{PEA}^u	ϕ_{RC}^l	ϕ_{RC}^u	$B_{0cme}^{10R_s^l}$	$B_{0cme}^{10R_s^u}$	H_{cme}^l	H_{cme}^u
9.63	20.0	4.1	6.55	55.3	88.4	8.5	21.6

3.4 Results and Discussion

We compare the magnetic flux and helicity of CMEs and their associated near-Earth interplanetary flux ropes, i.e., MCs and infer the origin of magnetic properties in CME flux ropes. In Table 3.4, we show the difference in helicity between the near-Sun and 1-AU flux ropes of the 15 March 2013 CME for $L_{mc} = 2, 2.5, \text{ and } \pi$ AU, respectively. For each approximate MC length, H_{mc} is less than H_{cme} . Also, it is observed that the ϕ_{pcme} of 15 March 2013 CME is comparable to ϕ_{pmc} , and much greater than ϕ_{zmc} . This suggests that the magnetic flux and helicity in flux ropes at 1 AU may be related to the magnetic reconnection at low corona. We find a minimum helicity difference in case of $L_{mc} = \pi$ AU with $H_{cme} = H_{cme}^l$. So, the lower bound of source region helicity is consistent with H_{mc} when MC length is π AU or the statistical value is 2.6 ± 0.3 AU considering the flux rope is still attached

to the Sun. A correspondence within 83% between the measured quantity of helicity at solar source and 1 AU is observed when the MC is estimated as a half torus with a total length of π AU. We notice a large helicity difference between H_{cme}^u and H_{mc} for each of the L_{mc} s.

Table 3.4: Comparison of magnetic helicity of 15 March 2013 CME and its interplanetary flux rope counterpart at 1 AU.

$(H_{cme}^l - H_{mc})/H_{cme}^l(\%)$			$(H_{cme}^u - H_{mc})/H_{cme}^u(\%)$		
(1)			(2)		
$L_{mc}=2$ AU	$L_{mc}=2.5$ AU	$L_{mc} = \pi$ AU	$L_{mc}=2$ AU	$L_{mc}=2.5$ AU	$L_{mc} = \pi$ AU
47.4	34.4	17.5	79.3	74.2	67.5

Table 3.5: Magnetic flux and helicity of CME and ICME flux ropes.

CME start (UT)	ϕ_{pcme} ($\times 10^{21}$ Mx)	H_{cme} ($\times 10^{42} Mx^2$)	ϕ_{zmc} ($\times 10^{21}$ Mx)	ϕ_{pmc} ($\times 10^{21}$ Mx)	H_{mc} ($\times 10^{42} Mx^2$)
(1)	(2)	(3)	(4)	(5)	(6)
2010/05/24 14:06	2.15	2.35	0.38	1.44	0.68
2011/05/25 13:25	1.09	0.38	0.21	0.80	0.21
2011/06/02 08:12	1.81	1.02	0.05	0.66	0.04
2012/02/10 20:00	2	2.18	0.14	0.72	0.13
2012/04/02 23:12	3.07	3.76	0.26	1.14	0.37
2012/11/09 15:12	2.47	2.43	0.16	1.18	0.24
2013/03/15 07:12	4.10	8.47	0.82	2.18	2.20
2013/04/11 07:24	3.72	6.29	1.14	2.72	3.85
2013/06/02 20:00	1.75	1.27	0.63	1.70	1.34
2013/07/09 15:12	3.50	7.75	1.48	2.83	5.19

Table 3.5 represents the magnetic flux and helicity of ten CMEs and associated MCs. In Column 1 we show the date and time (CME start) of first appearance of

the CME flux ropes in LASCO C2 field of view. Column 2 represents the CME poloidal flux (ϕ_{pcme}). The poloidal flux is equivalent to the reconnection flux (ϕ_{RC}^l) measured using AIA 193 Å at the associated solar sources. Column 3 shows the magnetic helicity (H_{cme}) of CME flux ropes where $H_{cme} = H_{cme}^l$. In Column 4, 5 and 6 we note the axial magnetic flux (ϕ_{zmc}), poloidal magnetic flux (ϕ_{pmc}) and helicity (H_{mc}) of MCs considering $L_{mc} = 1$ AU. We find a significant positive correlation with linear correlation coefficient r_p of 0.78 (99%) between ϕ_{pcme} and ϕ_{pmc} , and 0.69 (97.5%) between ϕ_{pcme} and ϕ_{zmc} , respectively. The correlation between H_{cme} and H_{mc} is also found to be high and significant with $r_p = 0.81$ (99%). The scatter plots of ϕ_{pcme} versus ϕ_{pmc} , and H_{cme} versus H_{mc} are shown in logarithmic scale in Figure 3.8(a) and 3.8(b), respectively. We perform a quantitative evaluation of flux and helicity relationship utilizing least-squares fits to the data pairs in logarithmic scale. The red dash lines over plotted on the plots represent the best fits to the data. The fit equations obtained for flux and helicity pairs are

$$\phi_{pmc} = 0.59\phi_{pcme}^{0.95}, \quad (3.9)$$

and

$$H_{mc} = 0.2H_{cme}^{1.1}, \quad (3.10)$$

respectively. The power-law index of Equation 3.9 and 3.10 are close to unity. When $L_{mc} = 2$ AU the ratio of ϕ_{pmc} and ϕ_{pcme} is around unity. With $L_{mc} = \pi$ AU as the upper limit, we obtain the contribution of ϕ_{pcme} ($= \phi_{RC}$) to ϕ_{pmc} as 54%. Whereas, for $L_{mc} = 2$ AU and π AU the H_{mc} is 40% and 66% of H_{cme} , respectively. These results can be summarised as $\phi_{RC} \propto \phi_{zmc}$, $\phi_{RC} \approx \phi_{pmc}$, and $H_{cme} \approx H_{mc}$. Also, the events analysed here have values of ϕ_{RC} greater than ϕ_{zmc} by at least a factor of 4. The relationship found between the magnetic flux of CMEs and MCs in our study is similar to that established by Qiu et al. (2007) and Gopalswamy et al. (2017a). Our results conform to the fact that helical magnetic structures of CMEs are primarily formed due to magnetic reconnection at their eruptive sources in low corona. A good correspondence in poloidal flux and helicity between CMEs and MCs where poloidal flux of CMEs is equivalent to the reconnection flux suggests that magnetic properties are transported to CMEs in the course of low-corona magnetic reconnection at the associated sources. As magnetic reconnection between CMEs

and ambient interplanetary magnetic fields is capable of removing MC helicity from MC front as well as back (Wang et al., 2018; Dasso et al., 2006), our estimated helicity values are expected to be the lower limits.

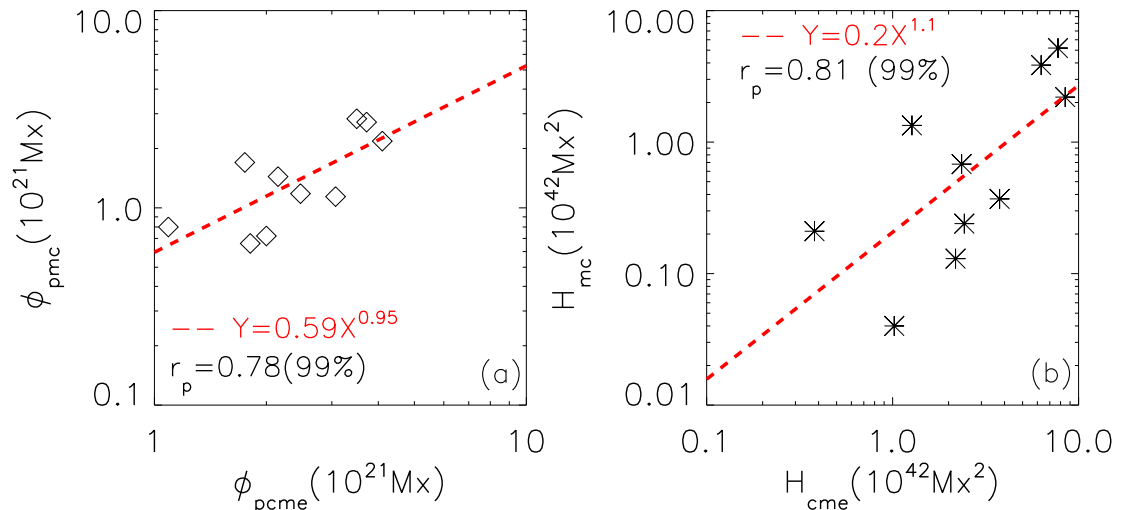


Figure 3.8: Scatter plots between (a) poloidal flux of CME flux ropes, ϕ_{pcme} and their associated MCs, ϕ_{mc} , and (b) helicity of CMEs (H_{cme}) and MCs (H_{mc}). The red dash over plotted lines represent the least-squares fits to the data. The fit equations along with the r_p values are mentioned on the plots.

Along with this study we measure the mean of global twist density (α_{AR}) (Leka and Skumanich, 1999) using HMI SHARP vector magnetograms just before the eruptions. To calculate this parameter we consider pixels with vertical magnetic field intensity greater than 100 G ($|B_z| > 100 \text{G}$) and the horizontal magnetic field strength greater than 200 G ($|B_h| > 200 \text{G}$) (e.g., Tiwari et al., 2015). Thus, we remove the noisy pixels and those which do not belong to ARs. Using α_{AR} , we calculate the overall global twist of ARs as $\alpha_{AR}L_{AR}$, where L_{AR} is approximated as the length of semi-circular loop with a radius of half of the distance between positive and negative flux weighted centers of ARs. For each of the L_{mc} s, we obtain that the MC twists are an order of two greater than that of the ARs. With $L_{mc} = \pi \text{AU}$ the MC average twist is found to be a factor of 115 greater than that of the ARs associated with the selected events in our study. This result matches well with what Leamon et al. (2004) found in their study of AR and MC twist with $L_{mc} = 2.5 \text{AU}$. This implies that the global twist of AR fails to estimate the twist imparted

due to reconnection. We also observe that the chirality of ICME flux ropes is quite consistent with that of their source regions. This confirms that magnetic helicity is approximately conserved during low-corona magnetic reconnection (Berger, 2005).

3.5 Summary and Conclusions

The main purpose of our study is to compare the magnetic flux and magnetic helicity of ICME flux ropes at 1 AU and those of their solar sources with the aim of understanding the origin of the magnetic properties of flux ropes. For this study, we select ten events with near-Sun and 1-AU flux rope configurations. We compute the poloidal magnetic flux and helicity of near-Sun flux ropes, i.e., CMEs using their source region reconnection flux and physical parameters such as radius of their cross-sections and total lengths. The magnetic properties of 1-AU flux ropes, i.e., MCs are obtained using a force-free cylindrical model fit to in situ data. We find a significant correspondence in the magnetic properties of MCs and their associated solar sources. We obtain that the flux of MCs is highly relevant to the low-corona magnetic reconnection. Assuming MC as a half torus with a total length of π AU the magnetic helicity of MCs is found to be broadly consistent with that of CMEs.

Our results are consistent with the scenario that low-corona magnetic reconnection forms helical magnetic flux ropes immediately before their expulsion. Thus, during the course of magnetic reconnection, the magnetic flux and helicity are likely transferred to the eruptive flux ropes. Extracting the magnetic information of CMEs at their sources and 1 AU is challenging because 1) flux rope fitting results of MCs and CMEs are not always perfect for each events, 2) solar wind data are only available at the localized position of the satellite and 3) a major uncertainty exists in estimating MC lengths as well as CME flux rope lengths. However, with better multi-vantage point observations this study may eventually lead to better estimates and predictions of the magnetic properties of ICME flux ropes at 1 AU and help us ascertaining their geo-effectiveness in advance.

Chapter 4

Flux erosion of CMEs during their interplanetary propagation

Chapter Summary

Magnetic clouds (MCs) are flux-rope magnetic structures forming a subset of interplanetary coronal mass ejections (ICMEs) which have significant space weather impacts. The geoeffectiveness of MCs depends on their properties which evolve during their interplanetary passage. Based on an analysis of observations spanning two solar cycles this chapter establishes that MCs interacting with the ambient solar wind magnetic field (i.e., heliospheric open flux) lose a substantial amount of their initial magnetic flux via magnetic reconnection, which in some cases, reduce their geoeffectiveness. We find a linear correlation between the eroded flux of MCs and solar open flux which is consistent with the scenario that MC erosion is mediated via the local heliospheric magnetic field draping around an MC during its interplanetary propagation. The solar open flux is governed by the sunspot cycle. This work therefore uncovers a hitherto unknown pathway for solar cycle modulation of the properties of MCs.

4.1 Introduction

Coronal mass ejections (CMEs) are magnetised plasma structures expelled sporadically from the Sun and travel toward the heliosphere as interplanetary coronal

mass ejections (ICMEs). If an ICME has a smoothly rotating strong magnetic field and a low proton temperature (Burlaga, Hundhausen, and Zhao, 1981; Klein and Burlaga, 1982) it is categorised as a magnetic cloud (MC). The twisted flux ropes of MCs (Goldstein, 1983; Burlaga, 1988; Lepping, Burlaga, and Jones, 1990) carry a significant amount of solar magnetic flux and helicity (Pal et al., 2017). While propagating through the interplanetary medium, the presence of a relative motion between an MC and the ambient plasma would result in a draping of the ambient interplanetary magnetic field (IMF) over the MC (Gosling and McComas, 1987). Such draping has been directly observed (e.g., Crooker et al., 1985) as well as modeled (e.g., Alksne and Webster, 1970). If the magnetic field orientation of the MC is opposite to that of the draped IMF, the process of magnetic reconnection (henceforth reconnection) is initiated (McComas et al., 1988). Due to this reconnection a part of the MC's magnetic flux is eroded away and an asymmetry is generated in its azimuthal magnetic flux that accumulates along the spacecraft trajectory. This fact has been established by observations (Dasso et al., 2006; Dasso et al., 2007; Möstl et al., 2008; Ruffenach et al., 2012; Ruffenach et al., 2015) as well as by using global MHD simulations (Schmidt and Cargill, 2003; Taubenschuss et al., 2010). Lavraud et al. (2014) showed that erosion of an MC's magnetic flux may reduce its geoeffectiveness by a significant amount.

Figure 4.1 shows an idealized schematic diagram of the draping of a purely radial ambient IMF about a fast moving MC and the MC's cross-section in a plane perpendicular to the ecliptic plane. The imbalance in the MC's accumulated azimuthal flux arises due to the reconnection at the MC's front.

An approximate understanding of the erosion of the magnetic flux of MCs due to reconnection with the IMF can be obtained with recourse to the Sweet-Parker model (Parker, 1957; Sweet, 1958). In the diffusion region (a small-scale region surrounding the reconnection site) Cassak and Shay (2007) showed that the reconnection rate scales as $E_{rec} \sim V_1 B_1 \sim V_2 B_2$, where V and B are the plasma flow speed and magnetic field intensity, respectively, and the subscripts '1' and '2' refer to either side of the inflow region. For steady state reconnection E_{rec} is uniform at the reconnection region, where E_{rec} defines the rate of magnetic flux that is transferred from the inflow to the dissipation region (Nakamura et al., 2018). This

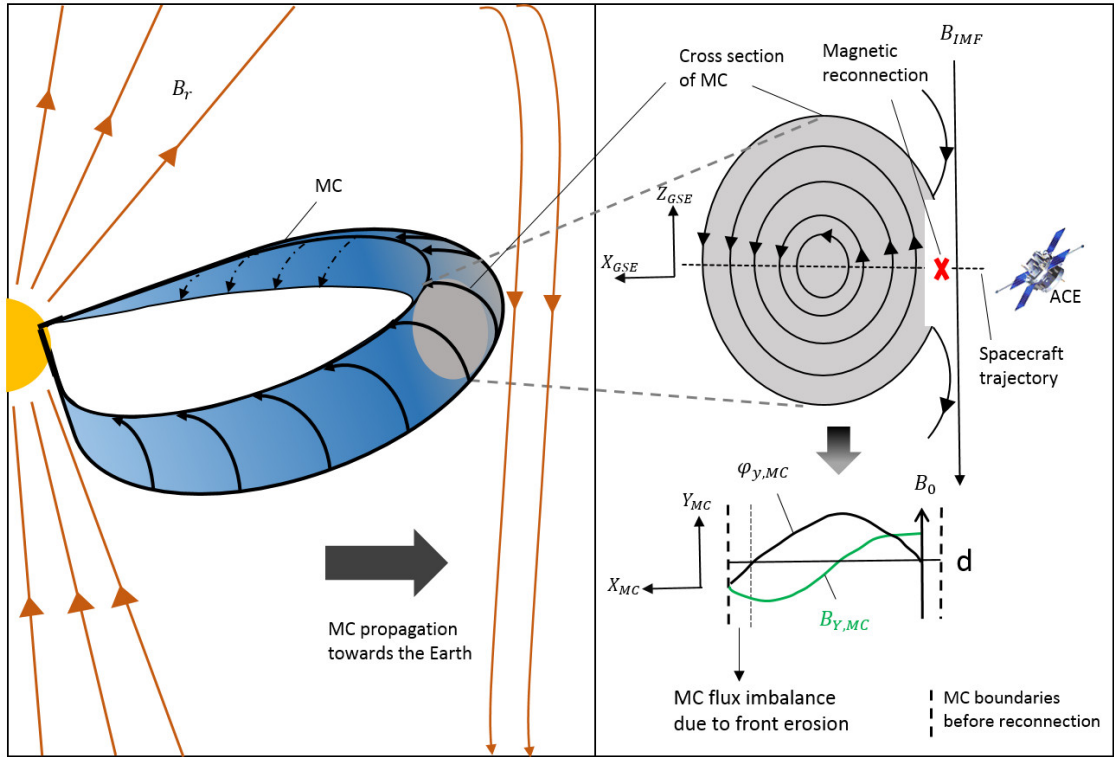


Figure 4.1: An idealized schematic of the ambient IMF draping about an MC propagating radially outward from the Sun towards the Earth (left), the MC's magnetic structure in a plane perpendicular to the ecliptic plane (right-top) and the expected variation in the MC's accumulated azimuthal flux due to its reconnection with the draped ambient IMF (right-bottom)

transferred magnetic flux determines the amount of flux erosion (F_{er}) and one expects that F_{er} would scale linearly with the background IMF field strength (Cassak and Shay, 2007).

The local Alfvén speed (V_A) in the plasma near the reconnection site governs the reconnection rate (Parker, 1973; Birn et al., 2001; Cassak and Shay, 2007). As V_A decreases with the increasing heliospheric distance, the reconnection rate is expected to be higher closer to the Sun and in the inner heliosphere (e.g., Lavraud and Borovsky, 2008). Dasso et al. (2007) found an extended coherent magnetic region just behind an MC and interpreted that this region is formed due to the reconnection process which started ≈ 54 hrs before the MC was observed. Lavraud et al. (2014) suggested that about 47% to 67% of the MC erosion is expected to occur within the orbit of Mercury (≈ 0.39 AU from the Sun). Ruffenach et al. (2015)

found no correlation between the eroded amount of magnetic flux and the ambient solar wind properties observed in situ at 1 AU. The lack of correlation suggests that most of the reconnection is expected to occur during the MC's passage through the inner heliosphere and not at 1 AU.

Large scale open magnetic field originating from the solar corona extends out into the heliosphere and shapes the IMF. Utilizing the observed solar photospheric magnetic field information as boundary condition the heliospheric magnetic field can be reconstructed following the simplest assumption that the solar corona is current-free (Schatten, Wilcox, and Ness, 1969). This approach is known as Potential Field Source Surface extrapolation (PFSS). In the outer radial boundary of the PFSS model the field lines are constrained to be radial which is consistent with the observations of the coronal hole foot-points (Wang, Hawley, and Sheeley, 1996). The open magnetic flux (ϕ_{open}) derived using the Sun's open magnetic field lines can be used to estimate the radial IMF intensity at any heliocentric distance from the Sun as the *Ulysses* spacecraft measurements show a latitudinal and longitudinal uniformity of the IMF's radial component (Smith and Balogh, 2008; Balogh et al., 1995; Erdős and Balogh, 2014). Therefore, the radial magnetic field intensity ($|B_r|$) can be expressed as $|B_r| = |\phi_{open}|/4\pi r^2$ at a heliocentric distance r ($r \gg R_\odot$). If θ_{HG} and ϕ_{HG} are the heliographic latitude and longitude, respectively, then the open magnetic flux can be derived by integrating $|B_r(R_{ss}, \theta_{HG}, \phi_{HG})|$ over the surface of a sphere concentric to the Sun with radius R_{ss} , known as source surface. Using ϕ_{open} , several studies have estimated B_r at $r = 1$ AU and compared it with the in situ near-Earth radial IMF intensity. The studies found a good correspondence between the estimated and observed values (Wang and Sheeley, 1988; Wang and Sheeley, 1995; Wang, Lean, and Sheeley, 2000; Yeates et al., 2010; Wang and Sheeley, 2015).

The present study aims to establish a connection between the MC's eroded magnetic flux and the IMF intensity. For achieving this we explore the relationship between annual averages of MC's eroded flux and the ϕ_{open} over two solar cycles. We present a distribution of the amount of eroded magnetic flux of MCs. Also, we perform a statistical analysis to investigate the geoeffectiveness of eroded MCs. We describe the data and their sources in section 4.2 and present our analysis methodology in section 4.3. Results are presented in section 4.4 followed by discussion and

conclusions in section 4.5 and section 4.6, respectively.

4.2 Instrumentation and overview of data

We use 64s average level 2 (verified) data of merged interplanetary magnetic field and solar wind parameters (http://www.srl.caltech.edu/ACE/ASC/level2/lv12DATA_MAG-SWEPAM.html) from the Advanced Composition Explorer (ACE) (Stone et al., 1998) spacecraft’s Solar wind Electron, Proton and Alpha Monitor (SWEPAM) (McComas et al., 1998) and Magnetic Field Experiment (MAG) (Smith et al., 1998) instruments. The selected data is in Geocentric Solar Ecliptic (GSE) coordinate system and available since the year 1998. In GSE coordinate system \hat{x}_{GSE} points toward the Sun, \hat{z}_{GSE} points towards the north pole (of the ecliptic) and \hat{y}_{GSE} completes the right-handed system. To obtain the geomagnetic response of MC we use the geomagnetic activity index (Dst) available at the World Data Center, Kyoto (<http://wdc.kugi.kyoto-u.ac.jp/dst/dir/index.html>) in a temporal resolution of 1 hour.

We obtain the radial magnetic field data from synoptic magnetograms (<http://hmi.stanford.edu/data/synoptic.html>) collected by the Michelson Doppler Imager (MDI) (Scherrer et al., 1995) onboard the Solar and Heliospheric Observatory (SOHO) (Domingo, Fleck, and Poland, 1995) and the Helioseismic and Magnetic Imager (HMI) (Scherrer et al., 2012) onboard the Solar Dynamics Observatory (SDO) (Pesnell, Thompson, and Chamberlin, 2012). The data from MDI and HMI is collected for a period of 1998-April 2010 and May 2010-2018, respectively. We utilize the radial magnetic field data to extrapolate the coronal magnetic field till the source surface at $r = R_{ss} = 2.5R_{\odot}$ using a global PFSS extrapolation model.

4.2.1 MC events and criteria for selection

In general, MCs are identified following the criteria defined by Burlaga, Hundhausen, and Zhao (1981) which are (1) throughout an MC interval the magnetic field intensity enhances (compared to the ambient solar wind), (2) smooth rotation in magnetic field direction through a large angle exists, (3) the proton temperature falls below the expected solar wind temperature (Lopez and Freeman, 1986),

and (4) the plasma β parameter is less than 1. For solar cycle 23 (1998-2007) we consider 37 MCs from a list of 109 MCs selected by Ruffenach et al. (2015). The study categorized the MCs as Q1 (both the front and rear boundaries of MCs are well determined), Q2 (any one of the two boundaries is identified without ambiguity) and Q3 (both the boundaries are difficult to identify). Of them, we select only Q1 and Q2 type MCs for our study as the fitting of flux ropes to the MCs is impacted by incorrect boundary selection. The events during 2008-2014 are obtained from the MC list published by Gopalswamy et al. (2015b) and the events of 2015-2018 are selected from the Richardson and Cane (2010) ICME catalogue (<http://www.srl.caltech.edu/ACE/ASC/DATA/level3/icmetable2.htm>) after manually identifying each of their boundaries. Thus, we select a total number of 35 events during solar cycle 24. Note that, each of the events selected here is consistent with Burlaga, Hundhausen, and Zhao (1981)'s definition of MCs. For none of the events, the spacecraft crosses the MC flux ropes parallel to the legs. This is because those cases lead an azimuthal flux asymmetry which may be misinterpreted as a result of erosion (Ruffenach et al., 2015). Also, there exist uncertainties in fitting parameters (e.g., Marubashi and Lepping, 2007; Lepping, Berdichevsky, and Ferguson, 2003) while those MCs are fit with the cylindrical flux rope model. Janvier, Démoulin, and Dasso (2013) introduced a location angle (λ) measured from the plane $(\hat{y}_{GSE}, \hat{z}_{GSE})$ towards the MC axis. It is a proxy for the spacecraft crossing distance from the MC nose. The λ evolves monotonically along the MC flux rope with $\lambda = -90^\circ$ in one leg, $\lambda = 0^\circ$ at its nose, and $\lambda = 90^\circ$ in the other leg. Ruffenach et al. (2015) estimated that errors in the azimuthal flux imbalance is less than 10% if λ holds a value between $\pm 45^\circ$. Thus we study only those MCs which cross the spacecraft trajectory sufficiently close to their apex by selecting $\lambda < |45^\circ|$.

4.3 Analysis methodology

Several case studies (Dasso et al., 2006; Dasso et al., 2007) show the presence of unbalanced azimuthal magnetic flux in MCs although MCs maintain a classical characteristic. Since the outer part of an MC is mainly affected by reconnection and the azimuthal flux is much greater than the axial flux in there (Ruffenach et al.,

2015), the asymmetry is mainly observed in the MC's azimuthal magnetic flux. To estimate this asymmetry we employ the "direct method" developed by Dasso et al. (2006).

4.3.1 Measurement of MC's eroded magnetic flux

The direct method uses the principle of magnetic flux conservation ($\nabla \cdot \mathbf{B} = 0$) across the plane formed by the spacecraft trajectory and MC axis to determine and analyse the MC's accumulated azimuthal magnetic flux. The MC axis orientation is defined by a latitude angle θ (the angle between MC's axis and the ecliptic plane) varying from -90° to 90° and a longitude angle ϕ (the angle between the projection of MC's axis on the ecliptic plane and the Earth-Sun direction) varying from 0° to 360° . Using θ and ϕ , we rotate the observed MC from GSE to the local MC coordinate defined by Dasso et al. (2006) and derive \mathbf{B}_{cloud} and \mathbf{V}_{cloud} from \mathbf{B}_{GSE} and \mathbf{V}_{GSE} . To obtain θ and ϕ we use a constant- α force-free flux rope model (Burlaga, 1988; Marubashi, 1986) to least-square fit the observed MCs. The model follows the equation $\nabla \times \mathbf{B} = \alpha \mathbf{B}$, where α is a constant and allows self-similar expansion of an MC. The Lundquist's solution to the equation (Lepping, Burlaga, and Jones, 1990) provides the modeled magnetic field vectors in the cylindrical coordinate system. After performing a series of iterations through proper adjustment of model parameters based on minimizing the difference (E_{rms}) between modeled and observed magnetic field vectors, a final set of best-fit parameters including θ and ϕ are ascertained (e.g., Marubashi and Lepping, 2007; Marubashi et al., 2012).

If θ , ϕ and the time of MC front (t_{front}) and rear boundaries (t_{rear}) are known, the accumulated azimuthal magnetic flux per unit length ($\frac{\phi_y(t_1, t_2)}{L}$) can be measured using

$$\frac{\phi_y(t_1, t_2)}{L} = \int_{t_1}^{t_2} B_{y,cloud}(t) V_{x,cloud} dt, \quad (4.1)$$

where L is the total length of the MC axis till 1 AU, $B_{y,cloud}$ and $V_{x,cloud}$ are the MC's magnetic field and velocity components computed in the local cloud coordinate system, respectively. The times t_1 and t_2 represent generic times defining the boundaries of the integral. The normalized perpendicular distance between spacecraft trajectory and MC axis is called the impact parameter (Y_0). The accumulated azimuthal flux is more precisely estimated when Y_0 is low. In Figure 4.2 we plot the

time evolution of $B_{y,cloud}$ (blue curve) along with ϕ_y/L (red curve) of two MCs during their passage through the spacecraft. Figure 4.2a shows an MC that is eroded at the front edge. The parameter ϕ_y/L is calculated considering $t_1 = t_{front}$ and $t_2 = t_{rear}$. Due to erosion its accumulated azimuthal flux shows an excess at its rear. The total azimuthal flux per unit length (ϕ_{az}) that was originally present in that MC (before erosion) is estimated by the unsigned value of $\phi_y(t_{center}, t_{rear})/L$. Here t_{center} (shown in dashed-dotted black vertical lines in Figures 4.2a and 4.2b) is the time when $B_{y,cloud}$ changes its sign and results in a maximum value of unsigned ϕ_y/L . The time t_{center} is the time when closest approach of the spacecraft to the MC axis is achieved. The eroded azimuthal flux (per unit length) of the MC is represented by the absolute value of ϕ_y/L at t_{rear} . The second MC (Figure 4.2b) is eroded at its rear and shows a flux imbalance at its front. Here ϕ_y/L is calculated considering $t_1 = t_{rear}$ and $t_2 = t_{front}$. For this case ϕ_{az} is estimated by the unsigned value of $\phi_y(t_{center}, t_{front})/L$. The eroded flux of the MC is defined by the absolute value of ϕ_y/L at t_{front} . We next define ϕ_{erod} as the eroded flux normalized to ϕ_{az} . The dashed-dotted green vertical lines show the estimated rear (Figure 4.2a) and front (Figure 4.2b) boundaries of the remaining flux-rope when it is observed in situ.

In Columns 4-7 of Table 4.1, we show the values of θ , ϕ , Y_0 , and E_{rms} obtained by least-square fit to the in situ MCs, respectively. The start and end times of associated MCs are mentioned in column 2 and 3. Column 1 contains the event number.

4.3.2 Estimation of the Sun's open flux

Understanding the origin of the Sun's open magnetic flux requires a knowledge of low coronal magnetic field structures, which are, in general, evaluated through extrapolation techniques. The simpler approach to extrapolate a magnetic field in the force-free corona is to assume the magnetic field to be potential (i.e., $\nabla \times \mathbf{B} = 0$). We follow the procedure formulated by Schatten, Wilcox, and Ness (1969) and Altschuler and Newkirk (1969) to reconstruct the solar coronal magnetic field. Extrapolation of the PFSS magnetic field is done using a finite-difference method similar to that of Ballegooijen, Priest, and Mackay (2000) with the help of a module

Table 4.1: 72 MCs with their start and end times, θ , ϕ , Y_0 , E_{rms} , ϕ_{az} , eroded flux and erosion positions. ‘F’ and ‘B’ denote the erosion at front and rear MC boundaries, respectively.

Event no.	Start time (UT)	End time (UT)	θ ($^\circ$)	ϕ ($^\circ$)	Y_0	E_{rms}	ϕ_{az} ($\times 10^{21}$ Mx)	eroded flux ($\times 10^{21}$ Mx)	Position
1	1998/03/04 14:41:00	1998/03/06 05:39:00	22.28	99.91	0.21	0.23	1.92	0.21	B
2	1998/05/02 12:08:00	1998/05/03 17:01:00	-77.63	156.65	0.90	0.31	0.75	0.13	F
3	1998/08/20 07:20:00	1998/08/21 20:22:00	-9.52	297.94	-0.02	0.35	2.12	0.07	F
4	1998/09/25 02:17:00	1998/09/26 10:01:00	30.82	122.3	0.2	0.4	4.99	3.81	B
5	1998/11/09 03:44:00	1998/11/10 02:34:00	-69.73	201.29	0.53	0.28	1.82	0.27	B
6	1999/04/16 18:45:00	1999/04/17 20:42:00	-42.66	127.48	0.28	0.3	2.84	1.09	F
7	1999/08/09 10:19:00	1999/08/10 18:38:00	81.28	158	0.33	0.33	1.36	0.24	B
8	1999/09/21 20:26:00	1999/09/22 11:33:00	11.08	56.08	0.81	0.42	0.53	0.15	F
9	2000/02/12 17:28:00	2000/02/13 00:29:00	-60.05	221.13	0.89	0.26	0.55	0.42	F
10	2000/02/21 14:45:00	2000/02/22 14:44:00	69.18	26.23	-0.57	0.29	1.8	0.34	F
11	2000/07/28 20:03:00	2000/07/29 10:19:00	-17.31	247.19	-0.8	0.35	0.82	0.51	F
12	2000/09/17 23:24:00	2000/09/18 15:28:00	39.82	220.55	-0.88	0.26	3.05	1.6	F
13	2000/10/13 17:38:00	2000/10/14 19:07:00	-52.18	85.53	-0.34	0.36	1.53	0.4	B
14	2001/03/19 19:01:00	2001/03/22 00:01:00	-69.42	141.02	0.09	0.3	5.45	0.87	F
15	2001/04/04 18:05:00	2001/04/05 08:24:00	30.52	297.06	-0.77	0.26	1.27	0.78	B
16	2001/04/22 00:12:00	2001/04/23 02:00:00	-47.4	314.49	0.47	0.19	1.22	0.05	F
17	2001/07/10 10:30:00	2001/07/12 02:57:00	-15.32	245.35	-0.26	0.43	1.52	0.51	B
18	2002/05/19 03:21:00	2002/05/20 03:35:00	10.16	236.05	-0.94	0.16	1.36	0.93	F
19	2002/08/02 07:09:00	2002/08/02 21:35:00	-12.73	310.54	0.85	0.16	0.7	0.25	F
20	2002/09/30 21:25:00	2002/10/02 03:08:00	-5.68	111.75	-0.06	0.35	3.02	0.7	F
21	2003/03/20 12:32:00	2003/03/20 22:51:00	-87.25	42.68	0.73	0.21	0.76	0.16	B
22	2003/11/20 11:39:00	2003/11/21 01:16:00	-64.17	156.6	0.31	0.18	4.29	0.46	B
23	2004/04/04 02:25:00	2004/04/05 19:30:00	75.76	290.95	-0.4	0.43	3.96	2.01	F
24	2004/07/24 11:52:00	2004/07/25 15:08:00	-38.7	88.49	-0.25	0.27	4.89	0.35	F
25	2004/07/27 01:38:00	2004/07/27 15:25:00	-16.58	115.43	0.11	0.25	2.74	0.01	F
26	2004/08/29 18:58:00	2004/08/30 21:55:00	-22.38	102.2	0.57	0.21	1.74	0.46	F
27	2004/11/09 20:30:00	2004/11/10 18:49:00	-34.96	228.91	-0.05	0.43	5.57	0.11	B
28	2005/05/15 05:32:00	2005/05/16 04:33:00	44.98	158.17	0.46	0.22	6.1	2.1	B
29	2005/06/15 05:16:00	2005/06/16 08:33:00	25.26	58.9	0.2	0.42	1.68	0.43	F
30	2005/07/17 15:17:00	2005/07/18 02:35:00	-19.06	101.53	0.53	0.23	0.82	0.1	B
31	2006/02/05 19:02:00	2006/02/06 10:45:00	-16.7	125.86	0.41	0.36	0.68	0.25	F
32	2006/04/13 15:25:00	2006/04/14 10:02:00	14.51	293.44	0.11	0.27	2.36	0.18	F
33	2006/09/30 08:51:00	2006/09/30 19:47:00	26.49	249.59	-0.37	0.5	0.91	0.24	F
34	2007/01/14 11:50:00	2007/01/15 07:12:00	12.06	254.88	-0.62	0.28	0.75	0.17	B
35	2007/05/21 22:23:00	2007/05/22 13:41:00	37.56	34	-0.07	0.27	0.98	0.1	B
36	2008/09/17 04:01:00	2008/09/18 08:00:00	72.03	26.78	0.44	0.34	0.9	0.01	F
37	2008/12/17 01:58:00	2008/12/17 17:35:00	-7.65	309.89	0.64	0.21	0.33	0.08	F
38	2009/02/04 02:29:00	2009/02/04 17:58:00	-54.83	124.9	0.13	0.45	1	0.19	B
39	2009/06/27 15:17:00	2009/06/28 12:00:00	74.05	236.38	-0.06	0.44	0.97	0.22	F
40	2009/07/21 01:47:00	2009/07/21 22:16:00	-1.45	90.64	0.27	0.35	0.54	0.16	B
41	2009/09/30 07:51:00	2009/09/30 20:45:00	11.54	308.35	0.2	0.2	0.32	0.01	B
42	2010/01/01 23:00:00	2010/01/03 00:00:00	45.52	53.37	-0.25	0.32	0.53	0	B
43	2010/02/07 18:55:00	2010/02/08 23:32:00	30.23	223.57	0.24	0.38	0.67	0.17	B
44	2010/05/28 21:00:00	2010/05/29 18:00:00	-62.76	323.96	0.39	0.28	1.2	0.09	F
45	2011/12/25 03:00:00	2011/12/25 17:06:00	8.32	262.64	0.7	0.26	0.24	0.05	F
46	2012/02/15 01:26:00	2012/02/16 05:34:00	-17	257.4	0.34	0.37	1.2	0.47	B
47	2012/04/06 09:34:00	2012/04/07 00:34:00	13.93	88.13	-0.66	0.27	0.53	0.07	F
48	2012/05/16 16:43:00	2012/05/17 19:38:00	27.61	289.98	-0.27	0.3	1.24	0.27	F
49	2012/07/09 00:43:00	2012/07/10 01:55:00	-45.22	9.02	0.43	0.29	1.15	0.09	F
50	2012/08/12 19:42:00	2012/08/13 08:00:00	-5.47	235.35	-0.77	0.34	0.38	0.19	B
51	2012/10/08 18:25:00	2012/10/09 14:41:00	-58.08	207.66	0.47	0.36	1.47	0.35	B
52	2012/10/12 20:00:00	2012/10/13 15:00:00	-77.89	129.1	0.28	0.32	1.18	0.11	B
53	2012/11/01 01:00:00	2012/11/02 07:00:00	-82.42	22.52	0.21	0.32	1.65	0.08	B
54	2012/11/13 09:00:00	2012/11/14 05:00:00	-5.68	64.75	-0.38	0.28	1.69	0.14	F
55	2013/01/17 17:07:00	2013/01/18 11:55:00	16.09	316.28	-0.55	0.32	1.01	0.08	B
56	2013/01/19 01:00:00	2013/01/19 18:00:00	-50.23	180.16	0.78	0.22	0.28	0.09	F
57	2013/04/14 16:45:00	2013/04/15 21:30:00	47.36	157.25	-0.85	0.17	1.16	0.63	F
58	2013/06/06 15:00:00	2013/06/07 19:00:00	-68.36	130.02	0.25	0.3	2.06	0.25	F
59	2013/06/28 02:00:00	2013/06/29 15:00:00	-64.23	328.58	0.17	0.3	2.06	0.03	B
60	2013/07/05 19:28:00	2013/07/07 14:30:00	-59.96	315.01	-0.08	0.28	2.29	0.31	B
61	2013/07/13 06:00:00	2013/07/15 00:18:00	-22.28	289.31	0	0.24	2.88	0.01	F
62	2013/10/02 23:16:00	2013/10/03 16:50:00	60.51	111.13	-0.93	0.22	0.8	0.67	F
63	2013/12/01 12:58:00	2013/12/02 22:45:00	-45.17	195.9	0.89	0.43	1.17	0.44	B
64	2013/12/25 04:53:00	2013/12/25 18:01:00	-58.73	118.81	-0.57	0.33	0.56	0.2	F
65	2014/04/05 23:00:00	2014/04/06 20:00:00	-52.71	322.52	0.88	0.22	0.89	0.51	B
66	2014/06/29 23:05:00	2014/06/30 12:21:00	51.8	114.29	0	0.39	0.61	0.2	B
67	2014/08/19 16:48:00	2014/08/21 07:01:00	63.44	352.54	0.04	0.35	3.17	0.02	B
68	2015/05/10 13:34:00	2015/05/11 03:27:00	-45.98	78.12	-0.45	0.32	0.62	0.1	F
69	2016/10/13 10:08:00	2016/10/14 13:04:00	-15.41	71.53	0.36	0.19	2.74	0.02	F
70	2016/11/09 19:54:00	2016/11/10 07:55:00	71.04	89.75	-0.03	0.44	0.86	0.18	F
71	2018/03/09 22:57:00	2018/03/10 22:36:00	-20.11	296.66	0.48	0.31	2.02	1.02	F
72	2018/07/10 12:01:00	2018/07/11 03:36:00	72.77	5.03	0.83	0.2	0.4	0.02	B

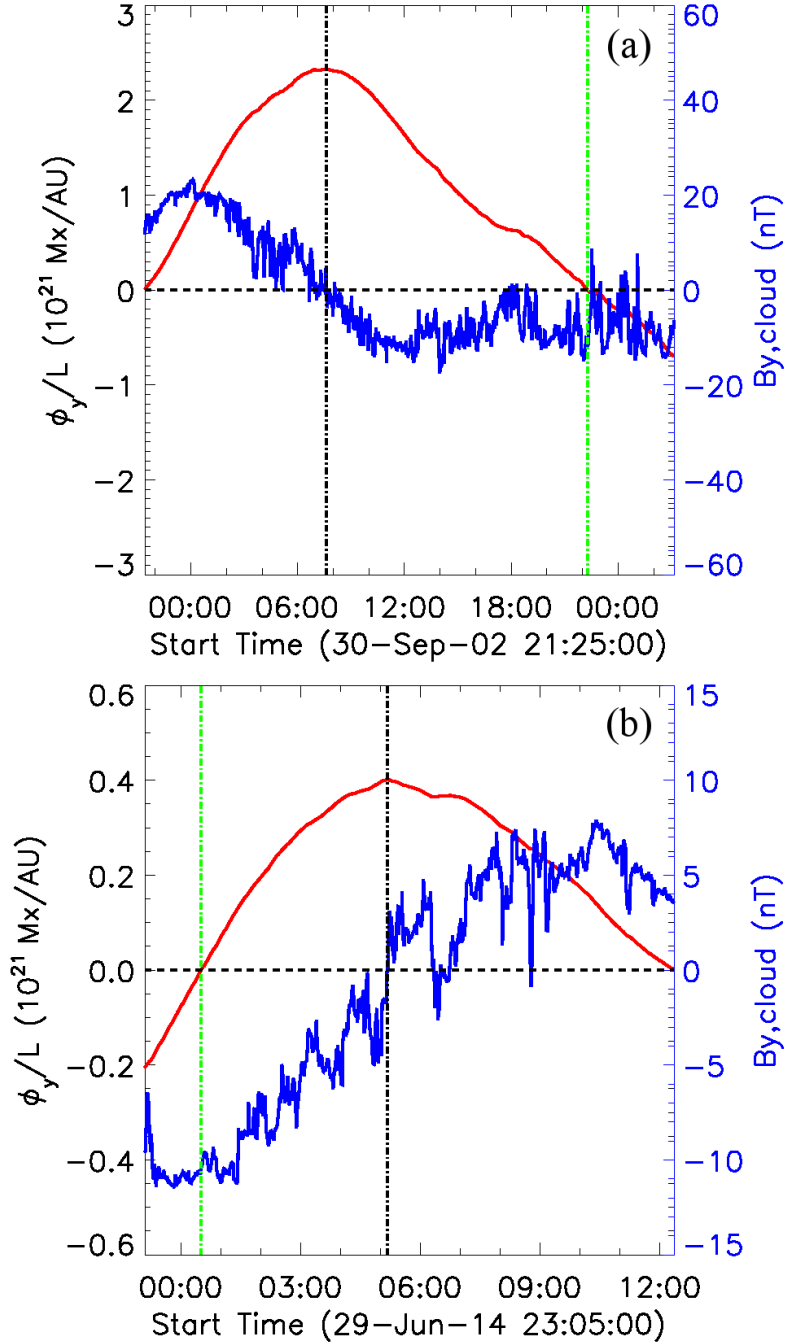


Figure 4.2: Plots depicting $B_{y,cloud}$ (blue) and ϕ_y/L (red) variations of two MCs during their passage past the spacecraft. The black and green vertical dashed-dotted lines represent t_{center} and the zero crossing of ϕ_y/L curves, respectively. (a) For an event where the flux erosion is at the MC-front. Here $\phi_{az} = 3.02 \times 10^{21}$ Mx/AU and eroded flux = 6.98×10^{20} Mx/AU. (b) For an event where the flux erosion is at MC-rear. Here $\phi_{az} = 6.06 \times 10^{20}$ Mx/AU and eroded flux = 2.04×10^{20} Mx/AU.

developed by Yeates (2018). The PFSS model produces a magnetic field distribution in the solar corona starting from $r = R_\odot$ to $R_{ss} = 2.5R_\odot$ by utilizing the observed photospheric magnetic field at the lower boundary (R_\odot). In this study we use photospheric magnetic field distribution observed by MDI and HMI to perform the PFSS extrapolation up to the source surface and compute the unsigned open flux ($|\phi_{open}|$). We obtain a strong positive correlation (with linear correlation coefficient, $r_p = 0.89$ at 99.99% confidence level) between the yearly averaged IMF intensity observed in situ at 1 AU and $|\phi_{open}|$. Therefore, $|\phi_{open}|$ can be used as a proxy of the IMF intensity.

4.4 Analysis and Results

By applying the direct method to all the selected MCs we derive ϕ_{az} , ϕ_{erod} , and the position of the flux imbalance (front or back) for each of the MCs. In Figure 4.4(a) we demonstrate the effect of MC's erosion on its geoeffectiveness by plotting MC's remaining azimuthal flux ($\phi_{az} - \text{eroded flux}$) versus its geomagnetic response (quantified by Dst_m – the minimum value of Dst during an MC's passage). The correlation between the remaining flux and Dst_m ($r_p = -0.7$ at 99.99% confidence) is slightly lower than the correlation between total flux and Dst_m ($r_p = -0.76$ at 99.99% confidence) if all events are considered. However, it is to be noted that the impact of MC's azimuthal flux erosion on its geomagnetic response is expected only if $B_{z,GSE}$ has a negative value at the reconnection site and the MC's azimuthal field component corresponds to $B_{z,GSE}$ (i.e., $\theta, \lambda \sim 0^\circ$) near the Earth (i.e., at 1 AU). Our sample has 9 MCs (depicted by red dots in Figure 4.4(a)) which have negative $B_{z,GSE}$ at their reconnection sites and $|\theta|, |\lambda| \leq 30^\circ$ (i.e., close to the above conditions, while still providing reasonable sample size). For these events the correlation between the remaining flux of MCs and Dst_m is higher ($r_p = -0.95$ at 99.99% confidence) compared to that between ϕ_{az} and Dst_m ($r_p = -0.88$ at 99.99% confidence). This reveals the impact of flux erosion on the geoeffectiveness of MCs.

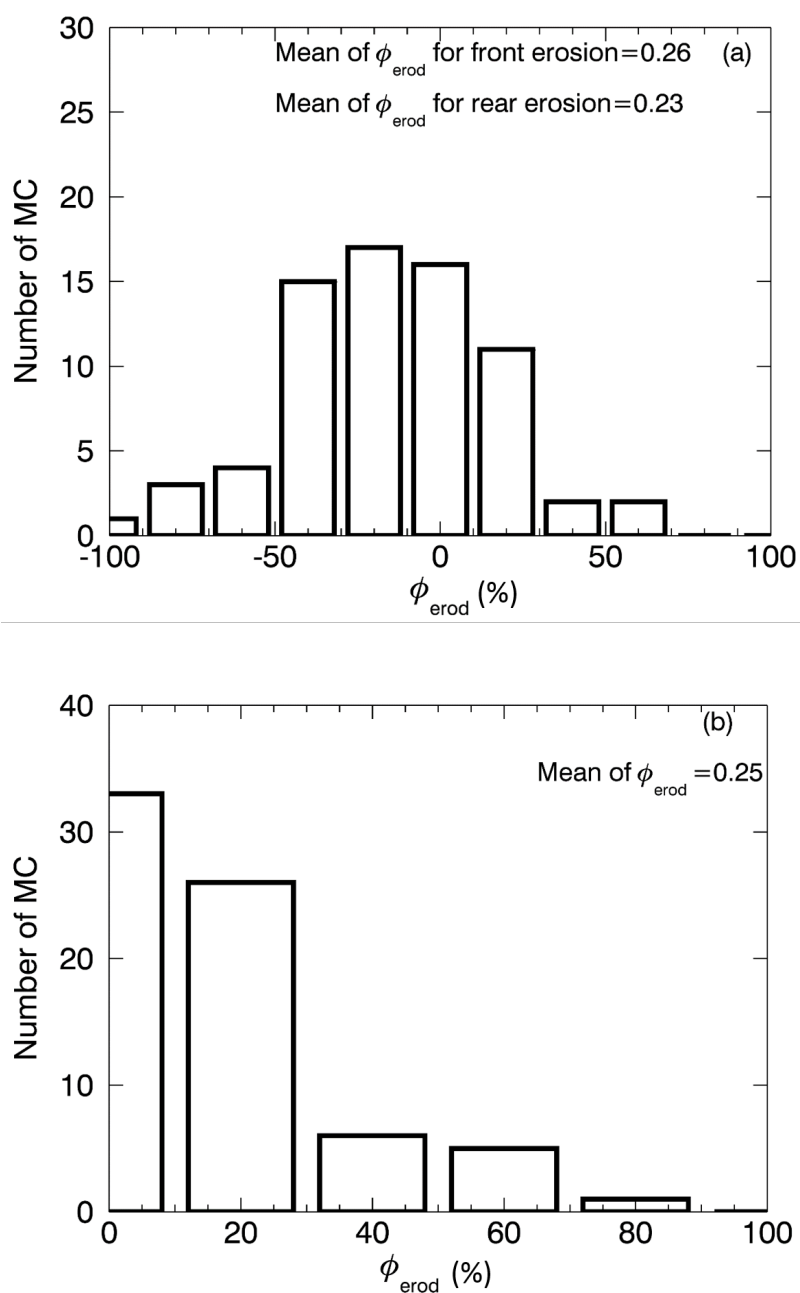


Figure 4.3: (a) Distribution of MCs as a function of ϕ_{erod} (%). The ϕ_{erod} (%) ranges from -100 to 0% if the erosion occurs at MC's front and 0 to 100% for the erosion at MC's rear. The mean of ϕ_{erod} for front and rear erosion are mentioned in the plot. (b) Distribution of MCs as a function of ϕ_{erod} (%) irrespective of the erosion position. The mean value of ϕ_{erod} for the distribution is mentioned in the plot.

4.4.1 Distribution of the MC's eroded azimuthal magnetic flux

In Figure 4.3a, we show a distribution of ϕ_{erod} . The negative (positive) value of ϕ_{erod} represents the erosion at the MC front (rear) boundary. We notice that out of 72, 40 MCs show the flux imbalance at rear with an average value of $\phi_{erod} \sim 0.26$ and 32 MCs show flux imbalance at front with an average $\phi_{erod} \sim 0.23$. The average eroded flux irrespective of the erosion position during solar cycle 23 and 24 are found to be 0.276 and 0.22, respectively. Our result matches well with the value of normalized average eroded flux found by Ruffenach et al. (2015) for the events during solar cycle 23. MCs showing flux imbalance at the front or rear boundaries are named as MC_F and MC_R , respectively. We plot the distribution of ϕ_{erod} irrespective of the erosion position in Figure 4.3b. We find that in an average, about 25% of MC's total azimuthal flux is eroded either at its front or rear boundaries.

4.4.2 Comparison between the Sun's unsigned open flux and MC flux erosion

In Table 4.2, we show the number of total MCs (column 2), MC_R (column 3), MC_F (column 4), annual averages of ϕ_{erod} (column 5), and unsigned ϕ_{open} (column 6) with their standard deviations corresponding to each year mentioned in column 1.

The erosion of magnetic flux in an MC depends on the rate of reconnection between the magnetic field of the MC and IMF. As it is stated before that the reconnection rate scales with the IMF intensity, a correlation is expected between ϕ_{erod} and the prevailing IMF strength whose proxy is the unsigned ϕ_{open} . We define the yearly average of the normalized eroded azimuthal flux ($\bar{\phi}_{erod}$) by averaging over ϕ_{erod} with the total number of events (N_{MC}) in each year. In Figure 4.4b, we plot $\bar{\phi}_{erod}$ and the yearly average of unsigned ϕ_{open} ($|\bar{\phi}_{open}|$) in solid red and dashed black curves, respectively, along with error bars over the period encompassing solar cycle 23 and 24. The error bars are calculated by estimating, $\frac{\sigma}{\sqrt{N_{event}}}$, where σ is the standard deviation and N_{event} represents number of MC events for the eroded flux and number of PFSS extrapolations for the calculation of the open flux in each year.

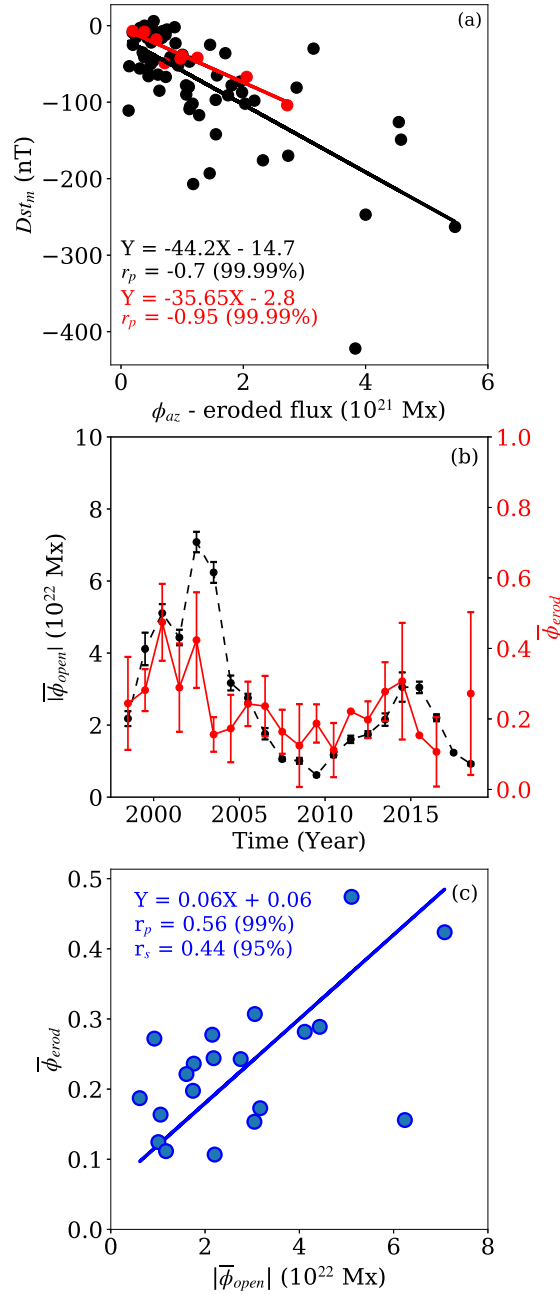


Figure 4.4: (a) Scatter plot between the remaining flux of MCs and their geoeffectiveness as quantified by the minimum Dst index (Dst_m). Least-squares fit considering all events (red and black dots) and the correlation are shown in black. For a subset of events (red dots only) as described in the text, the corresponding least-squares fit and correlation are depicted in red. (b) $\bar{\phi}_{erod}$ and $|\bar{\phi}_{open}|$ plotted against each year for solar cycle 23 and 24 in continuous red and dashed black curves, respectively. Vertical lines in corresponding colors represent the error bars for $\bar{\phi}_{erod}$ and $|\bar{\phi}_{open}|$. (c) Scatter plot of $|\bar{\phi}_{open}|$ versus $\bar{\phi}_{erod}$. The over plotted blue solid line shows the least-squares fit to the data points. The correlation is mentioned in blue.

Table 4.2: Total number of MCs, MC_R , MC_F in each year, annual average of normalised eroded flux ($\bar{\phi}_{erod}$), and unsigned ϕ_{open} ($\bar{\phi}_{open}$) along with their standard deviations over the two solar cycles (1998-2018).

Year	N_{MC}	MC_R	MC_F	$\bar{\phi}_{erod}$	$\bar{\phi}_{open}$
	#	#	#		($\times 10^{22}$ Mx)
(1)	(2)	(3)	(4)	(5)	(6)
1998	5	2	3	0.24±0.13	2.18±0.21
1999	3	2	1	0.28±0.06	4.12±0.45
2000	5	4	1	0.47±0.11	5.11±0.25
2001	4	2	2	0.29±0.13	4.43±0.22
2002	3	3	0	0.42±0.14	7.08±0.28
2003	2	0	2	0.16±0.05	6.24±0.29
2004	5	4	1	0.17±0.10	3.17±0.21
2005	3	1	2	0.24±0.06	2.76±0.11
2006	3	3	0	0.24±0.09	1.76±0.16
2007	2	0	2	0.16±0.06	1.06±0.05
2008	2	2	0	0.12±0.12	1.01±0.08
2009	4	1	3	0.19±0.05	0.61±0.04
2010	3	1	2	0.11±0.08	1.17±0.06
2011	1	1	0	0.22±0.00	1.60±0.10
2012	9	4	5	0.20±0.05	1.74±0.09
2013	10	6	4	0.28±0.08	2.15±0.17
2014	3	0	3	0.31±0.17	3.06±0.41
2015	1	1	0	0.15±0.00	3.05±0.16
2016	2	2	0	0.11±0.10	2.20±0.10
2017	0	0	0	–	1.23±0.03
2018	2	1	1	0.27±0.23	0.92±0.05

A correlation study is performed between $\bar{\phi}_{erod}$ and $|\bar{\phi}_{open}|$. We obtain a Pearson correlation coefficient (r_p) of 0.56 and a Spearman's rank correlation coefficient

(r_s) of 0.44, at 99% and 95% confidence levels, respectively. To confirm our result we compute r_p including the parameters' error bar information and find the value of r_p as 0.51 ± 0.03 at 98% confidence level. In Figure 4.4c, we show a scatter plot between $\bar{\phi}_{erod}$ and $|\bar{\phi}_{open}|$. The observed correspondence between the eroded flux and the Sun's open flux indicates an underlying linear relationship between the reconnection rate and the IMF intensity. To relate these two parameters, we perform a least-squares fit to $|\bar{\phi}_{open}|$ versus $\bar{\phi}_{erod}$ which gives the following equation

$$\bar{\phi}_{erod} = 0.06|\bar{\phi}_{open}| + 0.06, \quad (4.2)$$

where $|\bar{\phi}_{open}|$ is in units of $10^{22} Mx$. The solid blue line over plotted on the scatter plot represents the least-squares fitting.

4.5 Discussion

To establish a correspondence between MC's eroded flux and the IMF intensity, we study the dependency of the MC's eroded flux on the Sun's open flux over two solar cycles. We find that about 56% of the total MCs studied here are eroded at their front, whereas 44% are eroded at their back. A numerical simulation of reconnection between an MC and solar wind performed by Schmidt and Cargill (2003) shows an enhancement in reconnection with the increasing relative speed of the MC compared to the solar wind. If an MC is followed and compressed by a fast solar wind, reconnection may occur at the MC's rear boundary. Such high speed solar wind primarily originates from polar coronal holes and may extend towards low latitudes (Fenrich and Luhmann, 1998). Also, MCs can be compressed by co-rotating interaction regions whose formation is related to the presence of coronal holes (Rouillard et al., 2010). In our study we obtain the orientation of an MC axis by fitting the observed MC using a force free cylindrical flux rope model. The model is impacted by several factors, such as, incorrect boundary selection (Lepping, Berdichevsky, and Ferguson, 2003), non circular MC cross section (Savani et al., 2011b; Savani et al., 2011a) and high impact parameter values (Démoulin, Dasso, and Janvier, 2013; Riley et al., 2004). Ruffenach et al. (2015) showed that the flux rope fitting method has a tendency of deriving a consistently lower value of eroded flux because the model is based on axisymmetric geometry. Also, a high impact

parameter lowers the total azimuthal magnetic flux that causes an overestimation of the normalized eroded flux. The imbalance in MC azimuthal flux accumulated along the spacecraft path may occur due to various other reasons. When a high-speed CME propagates from Sun to Earth it undergoes strong deceleration (Jones et al., 2007). If a cool, dense filament material is located at the base of the CME, the momentum of the filament results in its forward movement through the decelerating CME. Thus, the protruding filament drives flow leading to a sideways transport of the CME's poloidal field. This can generate an azimuthal flux imbalance in the CME flux rope by the time the CME reaches the Earth. Manchester et al. (2014) explained such flux imbalances through simulation of a three-part structure CME observed on 20 January 2005. In such cases, the eroded magnetic flux amount does not depend on the rate of reconnection between the MC and the IMF. This may also contribute to a lower correlation between the amount of eroded MC flux and ϕ_{open} . Nonetheless, we find the correlation to be significant and the underlying relationship between ϕ_{erod} and ϕ_{open} to be linear.

4.6 Conclusions

We establish a relationship between the azimuthal magnetic flux erosion of MCs and the Sun's unsigned open flux that regulates the IMF intensity. Utilizing the direct method we investigate 72 MCs spanning solar cycles 23 and 24 to estimate the magnetic flux imbalance and erosion. We find that on average 28% and 22% of the total azimuthal magnetic flux of MCs of solar cycle 23 and 24, respectively, are eroded during their propagation through the inner heliosphere. The reconnection causing this erosion may occur on either side of the MC boundaries and peel off an almost similar amount of magnetic flux. We compare the annual averages of solar open flux to the average fraction of the eroded magnetic flux of MCs over the past 21 years (from 1998 to 2018) and find a significant positive correlation with an underlying linear relationship. Since the solar open flux is strongly correlated with the IMF intensity, this is suggestive of the latter's role in MC flux erosion.

We note that the solar open flux is governed by the emergence and redistribution of active region magnetic fields on the Sun's surface due to surface flux transport

processes – a crucial component of the solar dynamo mechanism (Bhowmik and Nandy, 2018). Given that the solar wind dispersed open flux determines the ambient heliospheric magnetic field (IMF), the latter’s solar cycle modulation provides a novel pathway via which the large-scale solar cycle can govern flux erosion and thus possibly the geoeffectiveness of interplanetary magnetic clouds.

Chapter 5

An approach for forecasting the magnetic profiles of Earth-directed CMEs

Chapter Summary

The Earth's magnetosphere gets magnetically connected and exposed to the heliospheric environment when it reconnects with the solar transient events like coronal mass ejections (CMEs). Reconnection is favoured when a CME arrives at Earth with a prolonged southward magnetic field component. Thus, prediction of an Earth-directed CME's magnetic profile is important in estimating its geomagnetic response. In this chapter we present an approach for forecasting the magnetic vectors within the Earth directed segments of CMEs. The configuration of a flux-rope CME is approximated as a radially expanding force-free cylindrical structure. Combining near-Sun geometrical, magnetic and kinetic properties of CMEs with the force-free model we predict the magnetic vectors of CME associated magnetic clouds (MCs). Our predicted magnetic profile of MCs matches well with in situ observations. Utilising this approach, prediction of CME's geoeffectiveness – one of the most challenging tasks in forecasting space weather – can be achieved.

5.1 Introduction

Understanding space weather and its variability becomes more important as we rely more and more on the space-borne technology and interconnected power-grids which are sensitive to space weather transients (e.g., Schrijver et al., 2015). Coronal mass ejections (CMEs) are one of the strongest drivers of space weather events. Their flux rope structures can be observed in white-light coronagraphs at near-Sun regime. Near the Earth, in situ measurements of solar wind parameters are used to investigate the flux rope configuration of CMEs. When the twisted magnetic structure of CMEs contain southward magnetic field components, the CMEs reconnect with the Earth's magnetosphere and lead to an injection of energised solar wind particles into the Earth's atmosphere. CMEs having prolonged and strong southward magnetic fields cause ring current enhancement and result in geomagnetic storms (Tsurutani et al., 1988; Gonzalez, Tsurutani, and De Gonzalez, 1999). Therefore, prior knowledge of the magnetic properties of Earth-directed CMEs could facilitate predictions of their geoeffectiveness.

CMEs expand during their interplanetary propagation (Burlaga et al., 1981; Burlaga, 1991). A study by Démoulin and Dasso (2009) demonstrates that the rapid decrease of solar wind pressure with increasing distance from the Sun is the main driver of the radial expansion of CMEs. The influence of flux-rope CME's internal over-pressure, twist and radial distribution in its expansion is negligible. The deflection of CMEs changes their latitudes, longitudes and causes severe rotations (Vourlidas et al., 2011) of their axes. It is a common phenomenon that occurs in presence of magnetic forces at solar corona (Isavnin, Vourlidas, and Kilpua, 2014; Kay, Opher, and Evans, 2015). During the interplanetary propagation, CME deflection may take place because of the interactions with background solar wind magnetic fields (Wang et al., 2004) and preceding or following CMEs (Wang et al., 2004; Wang et al., 2014). Often deflection causes a CME to impact the Earth and rotation changes its magnetic field orientation leading the CME to become geoeffective. The distortion of CME's geometrical structure can be observed in coronagraphs. However, the influence of distortion on CME's magnetic structure is hard to estimate because the CME flux ropes appear as dark cavities in coronagraphs. One of the common approaches to estimate CME's magnetic vectors is to use solar observations

as input to three-dimensional magnetohydrodynamic (MHD) models (Manchester et al., 2004). However, such models are computationally expensive (Manchester, Holst, and Lavraud, 2014). Using analytical and semi-analytical models which approximate CMEs as force-free cylindrical flux-ropes, several studies have performed predictions of the magnetic structure of CMEs (Savani et al., 2015; Kay and Gopalswamy, 2017; Sarkar, Gopalswamy, and Srivastava, 2020). The major drawback of the model by Savani et al. (2015) is that it does not consider the expanding nature of CMEs. Both the models of Savani et al. (2015) and Kay and Gopalswamy (2017) consider CME’s axial magnetic field intensity, arrival speed and time as free parameters. The models infer the initial orientations of CME axis and the handedness of CME’s helical magnetic fields using only the “Bothmer-Schwenn” scheme (Bothmer and Schwenn, 1998) that fails to provide correct estimations when the overlying magnetic field arcades are present at CME sources. The INterplanetary Flux ROpe Simulator (INFROS) by Sarkar, Gopalswamy, and Srivastava (2020) incorporates the expansion of CMEs, measure their axial magnetic field intensity and derive the handedness and foot points of CMEs using extreme ultraviolet (EUV), H-alpha and magnetogram observations of their sources. However, the model does not evaluate the radial expansion speed, propagation speed and radial extent of CME associated magnetic clouds (MCs) while the MCs cross spacecraft at 1 AU.

In this chapter we present an approach for approximating magnetic field vectors inside Earth-directed MCs long before they reach the Earth using their near-Sun observations. We use an analytical model – a constant α force-free cylindrical model to model flux-rope CMEs. The model is constrained by the near-Sun observations of CME kinematics, geometrical and magnetic properties. Our model involves prior estimation of an MC’s arrival speed and time, its radial expanding nature and derives MC’s propagation speed and radial extent while it crosses a spacecraft.

We organise this chapter as follows. In Section 5.2 we describe the model that we use to configure CME flux ropes, and explain procedures of estimating the model inputs. In Section 5.3 we validate our model using in situ observed MC events. The results are discussed in Section 5.4 and we conclude our chapter in Section 5.5.

5.2 Methodology: Modeling of MCs using near-Sun observations

5.2.1 Model description

To examine the configuration of MCs we assume that MC flux ropes are force free (Goldstein, 1983), i.e., $\mathbf{J} = \alpha\mathbf{B}$, where \mathbf{J} and \mathbf{B} represent the current density and magnetic field vector, respectively. The parameter α is a constant force free factor. With this variable α the model was first used by Marubashi (1986) to fit two MCs. Later a study by Burlaga (1988) showed that α can be considered as constant to describe a magnetic cloud in first order. For constant α the solutions of the force-free model in cylindrical co-ordinates are obtained by Lundquist (1951), where the axial (B_{ax}), azimuthal (B_{az}), and radial (B_{rad}) magnetic field components are given by,

$$B_{ax} = B_0 J_0(\alpha\rho), \quad (5.1)$$

$$B_{az} = HB_0 J_1(\alpha\rho), \quad (5.2)$$

and

$$B_\rho = 0, \quad (5.3)$$

respectively. In Equation 5.2 H represents the chirality of cylindrical flux ropes. The right and left-handed chirality of flux ropes are indicated by $H = 1$ and $H = -1$, respectively. The axial magnetic field intensity of flux ropes is represented by B_0 . The zeroth and first order Bessel functions of first kind are shown by J_0 and J_1 , respectively. The parameter ρ is the radial distance from MC axis, and α is related to flux rope size. The value of α is chosen so that $\alpha R_{MC} = 2.41$, where 2.41 is the first zero of J_0 and R_{MC} is the radius of MC. The field configuration described in Equation 5.1 and 5.2 are static. Burlaga et al. (1981) and Burlaga (1991) indicated the expanding nature of MCs causing smooth decrease in solar wind speed and low solar wind proton temperature during their intervals. Démoulin et al. (2008) and Démoulin and Dasso (2009) performed theoretical studies on the expansion of MCs. The studies concluded that MCs expand self-similarly resulting in a linear radial velocity profile of MCs and the rate of MC expansion is proportional to the MC radius. The expansion of MC was first modeled by Osherovich, Farrugia, and

Burlaga (1993) later followed by other studies, including, Marubashi (1997), Hidalgo (2003), and Vandas et al. (2006), and Marubashi and Lepping (2007). These models are intended to fit the velocity magnitude profile of MCs. It is assumed that in an asymptotic limit, a flux rope expands radially with a speed

$$V_{exp} = \frac{\rho}{t + t_0}, \quad (5.4)$$

where the force free field configuration is maintained at any instant of time t (Shimazu and Vandas, 2002; Vandas et al., 2006; Vandas, Romashets, and Geranios, 2015). In a self-similar expansion, the t_0 in Equation 5.4 represents the time by which the expansion of flux rope has proceeded before it comes into contact with the spacecraft. If a self-similarly expanding MC changes its radius from its initial value $R_{MC}(0)$ to $R_{MC}(t)$ by the time t , the $R_{MC}(t)$ can be represented as $R_{MC}(t) = R_{MC}(0)(1 + \frac{t}{t_0})$. Thus, for an expanding flux rope, α and B_0 become time-dependent and are expressed as $\alpha = \frac{\alpha_0}{(1 + \frac{t}{t_0})}$ and $B_0 = \frac{B'_0}{(1 + \frac{t}{t_0})^2}$, where $\alpha_0 = 2.41/R_{MC}(0)$ and B'_0 is the axial magnetic field intensity when the MC first encounters with the spacecraft. Considering the expansion of MCs along radial and axial directions Equation 5.1 & 5.2 are modified as

$$B_{ax} = \frac{B'_0 J_0(\frac{\alpha_0}{(1 + \frac{t}{t_0})} \rho)}{(1 + \frac{t}{t_0})^2}, \quad (5.5)$$

$$B_{az} = H \frac{B'_0 J_1(\frac{\alpha_0}{(1 + \frac{t}{t_0})} \rho)}{(1 + \frac{t}{t_0})^2}, \quad (5.6)$$

where the force free condition is preserved throughout the propagation of MCs. Knowledge of the perpendicular distance (p) between an MC axis and the location of a spacecraft performing in situ measurements of the MC is necessary to obtain ρ . Figure 5.1 shows a cylindrical MC flux rope and its expanding cross-section. The MC expands with a velocity V_{exp} and its axis propagates with a speed V_p . In flux rope frame of reference it is assumed that the spacecraft propagates with the speed V_p . At the in-bound and out-bound regions of MCs the V_{exp} is added to and subtracted from the ambient solar wind speed, respectively, to obtain V_p (Vandas, Romashets, and Geranios, 2015). For $0 < p < R_{MC}$ the $\rho(t) = \sqrt{p^2 + (D^2(t) - V_p(t) \times t)}$, where $D(t) = \sqrt{R_{MC}^2(t) - p^2}$. Thus at $t = 0$, when an MC first encounters a spacecraft the $\rho(0) = R_{MC}(0)$. Figure 5.1 is shown

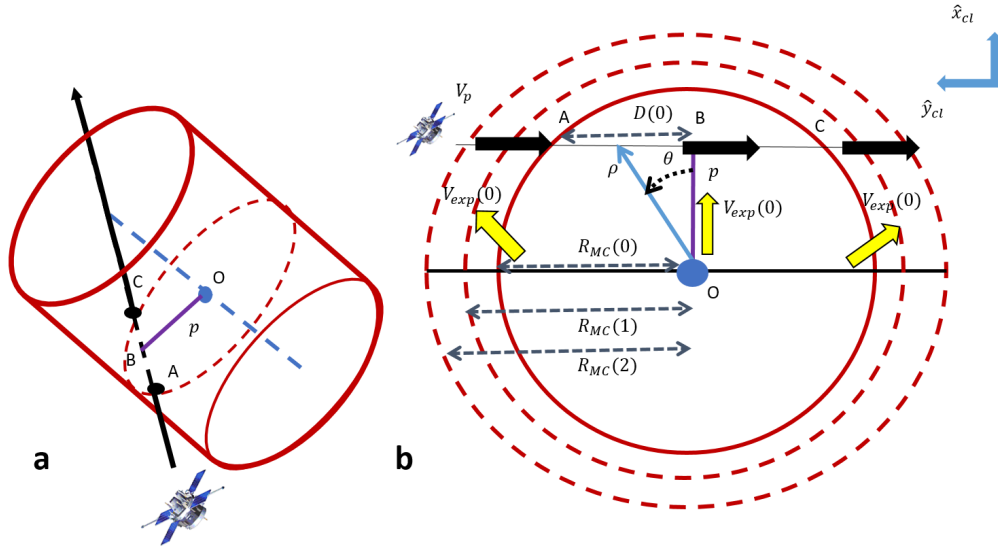


Figure 5.1: (a) A cylindrical structure of an MC where its cross sectoral circumference and axis are shown in red dash circle and blue dash line, respectively. In the flux rope frame of reference the spacecraft traversing path (‘AC’) is shown by black line and the perpendicular distance (‘OB’) between the MC axis and ‘AC’ is indicated by a purple line. (b) The expanding circular cross section of a cylindrical MC. ‘O’ is the centre of the cross section. At $t = 0$ the MC’s cross sectoral circumference is denoted by a red circle. The MC’s radial expansion with a speed V_{exp} is in the direction of the yellow arrows and the spacecraft propagates with a speed V_p towards the path indicated by black arrows.

in flux rope frame of reference where the spacecraft traverses through the MC with a speed V_p and p represents the perpendicular distance between the MC axis and the spacecraft path. The schematic shown in Figure 5.1(a) represents the crossing of a spacecraft through an MC via a path ‘AC’ indicated by black dash line. The MC axis is shown in blue dash line and the circumference of the MC cross-section is indicated by a red dash circle. The centre of the MC is pointed by ‘O’, and ‘OB’ represents the length p . In Figure 5.1(b) the expanding MC cross-section is shown. At $t = 0$, the circle made of solid red line represents the MC cross-section circumference where the distance ‘AB’ is equivalent to $D(0)$. We consider $V_{exp}(0)$ as the

average expansion speed of MCs observed during solar cycle 24 (Gopalswamy et al., 2015a) and estimate the t_0 value from $t_0 = V_{exp}(0)/R_{MC}(0)$. Lepping et al. (2008) analysed 53 MCs of standard profiles and obtained their expansion speed using two different methods namely the “scalar” method and “vector determination”. They found the most probable values of expansion speed to be around 30 km/s which is very near to the average expansion speed (25 km/s) used in our study.

To obtain the model parameters specifically p , R_{MC0} , B'_0 and H the near-Sun observations of MC associated CME flux ropes are utilized. Usually, the significant deflection and rotation of CMEs occur near the Sun, within $10R_\odot$ (Kay and Opher, 2015; Lynch et al., 2009). It is assumed that the propagation direction, axis orientation, and chirality of CMEs obtained at $10R_\odot$ remain unchanged throughout their Sun-Earth propagation. Whereas, due to self-similar expansion (Subramanian et al., 2014; Vršnak et al., 2019) in the course of interplanetary propagation, the radius and magnetic field intensity of CMEs are assumed to evolve from their initial values approximated at $10R_\odot$. In the following sections we discuss the procedures used in determination of model parameters.

5.2.2 Estimates of the geometrical properties of flux ropes

At $10R_\odot$, we estimate CME’s three-dimensional morphology and propagation direction by fitting the geometrical structure of CMEs using graduated cylindrical shell (GCS) model (Thernisien, 2011). The CMEs are observed in C2 & C3 coronagraphs of Large Angle and Spectrometric Coronagraph (LASCO) telescope on board the Solar and Heliospheric Observatory (SOHO) and COR2 A & B of Sun Earth Connection Coronal and Heliospheric Investigation (SECCHI) on board the Solar Terrestrial Relations Observatory (STEREO). By fitting the CMEs with GCS model, we obtain the latitude (θ_{HG}) and longitude (ϕ_{HG}) of the apex of CMEs in Stonyhurst heliographic coordinates, the *tilt* of the axis of flux rope CMEs, aspect ratio (κ), height ($height_l$) of the CME leading edges and the angle (AW) formed between the two legs of CME flux ropes. The uncertainty in determining *tilt* using GCS is $\pm 10^\circ$ (Thernisien, Vourlidis, and Howard, 2009). Sarkar, Gopalswamy, and Srivastava (2020) considered uncertainties of $\pm 10^\circ$ in θ_{HG} & ϕ_{HG} determinations and $\pm 10\%$ in obtaining κ . Using θ_{HG} , ϕ_{HG} , and *tilt* we formulate the flux rope axis

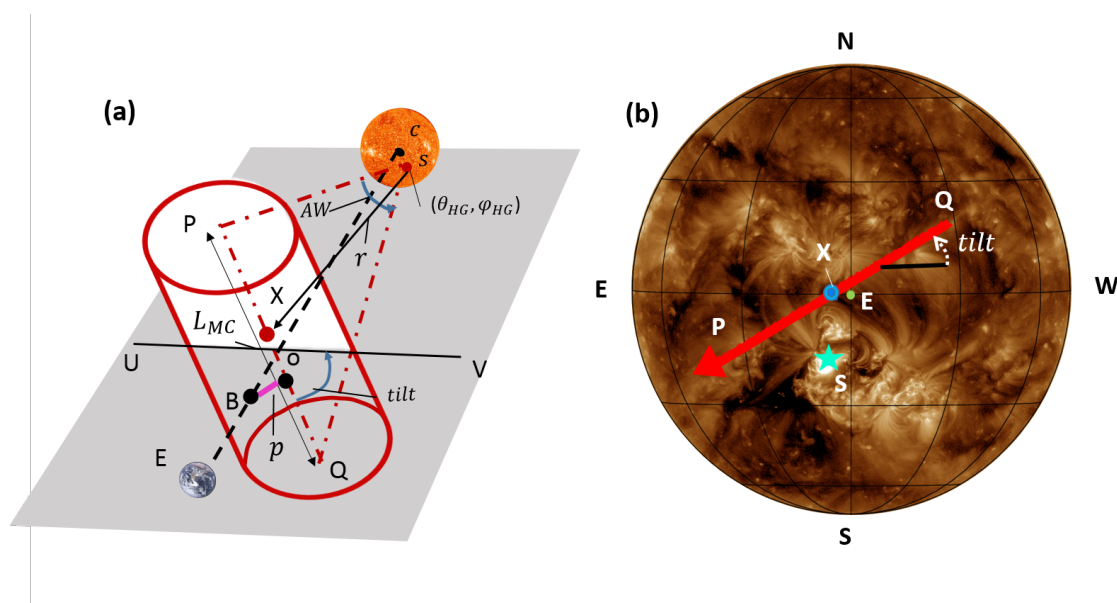


Figure 5.2: (a) A schematic of MC flux rope (red curve), and the position of the Sun and the Earth 'E'. The AW , $tilt$, Sun-center 'C' and CME source location 'S' on solar disk are mentioned on the figure. The flux rope axis is shown in red dash-dotted line. The equatorial plane is denoted by grey. The Sun-Earth line 'CE' is shown by black dashed line. The heliocentric distance r and L_{MC} are indicated by the lines 'SX' and 'PQ', respectively. The perpendicular distance p is denoted by the line 'OB'. The line 'UV' is perpendicular to 'CE'. (b) A South-East directed MC axis ('PQ') shown in red line projected on the solar disk. Its apex is denoted by 'X'. The MC's solar source ('S') is indicated by a star and the projected location of the Earth ('E') on the solar disk is denoted by a green circle. The axis has a positive $tilt$ with respect to the East-West line.

and considering the Earth's location as $(\theta_{HG}, \phi_{HG}) = (0, 0)$ we define p as

$$p = \frac{|\theta_{HG} - \phi_{HG} \tan(\text{tilt})|}{\sqrt{1 + \tan^2(\text{tilt})}}. \quad (5.7)$$

Using κ that constrains the flux rope expansion, $R_{MC}(0)$ can be determined by

$$R_{MC}(0) = \frac{\text{height}_{MC}}{1 + 1/\kappa}, \quad (5.8)$$

where height_{MC} is the leading-edge height of MCs reaching at the Earth. Thus, it is equivalent to the Sun-Earth distance. The length (L_{MC}) of the flux rope axis at any heliocentric distance (r) is obtained using AW by the formula $L_{MC} = (AW \times r)$, where AW is in radian. In Figure 5.2(a), we show a schematic of cylindrical flux rope with the Sun, Earth and spacecraft positions. The CME source location ('s'), apex ('X'), tilt, angular width (AW), heliocentric distance (r), L_{MC} and p are indicated on the Figure. The centre of the Sun and Earth are denoted by 'c' and 'E', respectively. Figure 5.2(b) shows a South-East directed MC flux rope axis 'PQ' projected on the solar disk with a positive tilt measured anti-clockwise from the East-West direction. The Earth's location $(\theta_{HG}, \phi_{HG}) = (0, 0)$ projected on the solar disk is noted by 'E'.

5.2.3 Estimation of flux-rope's near-Sun magnetic properties

The magnetic type of a flux rope can be determined using its chirality – right-handed or left-handed twist of the flux rope's helical magnetic field component, and the direction of its axial magnetic field. Based on these two properties, CME flux ropes are classified into eight different types (Bothmer and Schwenn, 1998; Mulligan, Russell, and Luhmann, 1998). Four of them have low-inclination and other four have high-inclination flux rope axes. These eight types of flux ropes include all possible axial field orientations having right-handed and left-handed chirality of flux-rope helical fields. A sketch representing eight types of flux ropes are shown in Figure 5.3.

Determination of flux rope chirality

To estimate the handedness of flux ropes we analyse the Helioseismic Magnetic Imagers (HMI) line-of-sight (LOS) magnetograms, Atmospheric Imaging Assembly (AIA) images on board Solar Dynamic Observatory (SDO) and H- α images of the flux ropes' solar sources for observing their early evolution. The chirality of solar sources indicate the chirality of the associated flux ropes as magnetic helicity is a conserved quantity even though magnetic reconnection is present (Berger, 2005). The chirality is inferred using the proxies discussed in Palmerio et al. (2017). Such proxies are discussed below.

- **Magnetic tongue** (Fuentes et al., 2000; Luoni et al., 2011): It is a vertical

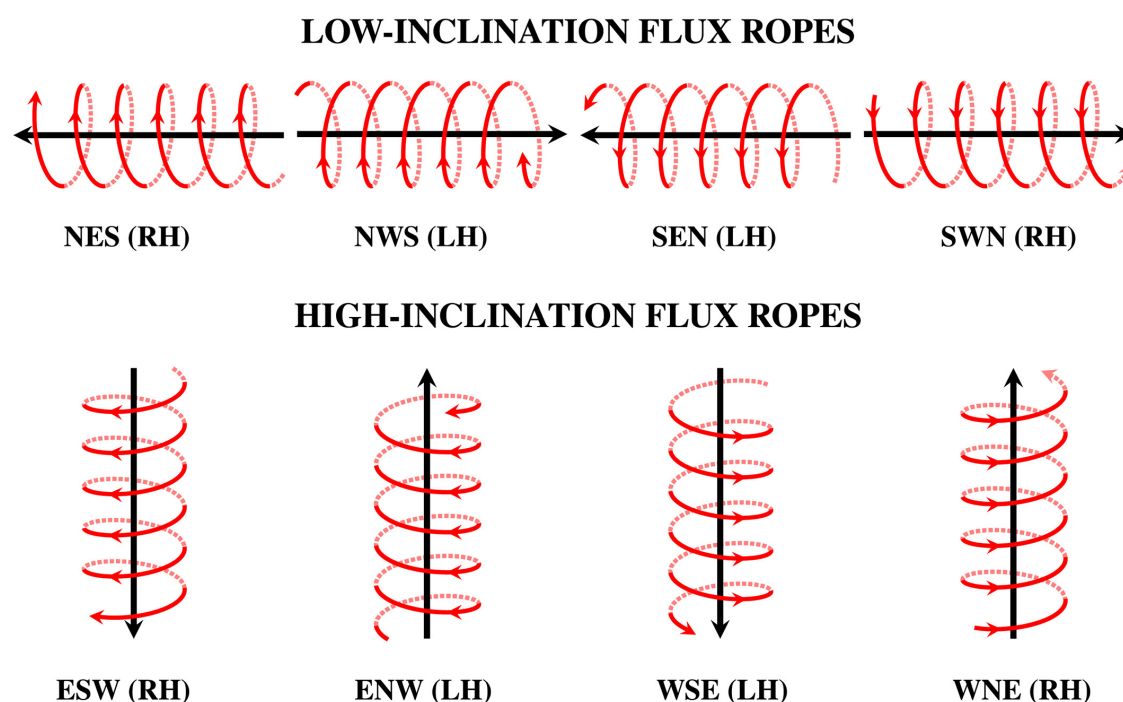


Figure 5.3: A sketch representing eight types of flux ropes. For each type, the helical and axial field lines are shown in red and black, respectively. Each letter of the name of the type of flux ropes corresponds to one of four directions, i.e., North, South, East, West, and RH and LH denote right-handed and left-handed chirality, respectively. The first and last letters indicate the helical field directions and the letter in between indicates the flux rope's axial field direction. The image is adapted from Palmerio et al. (2018)

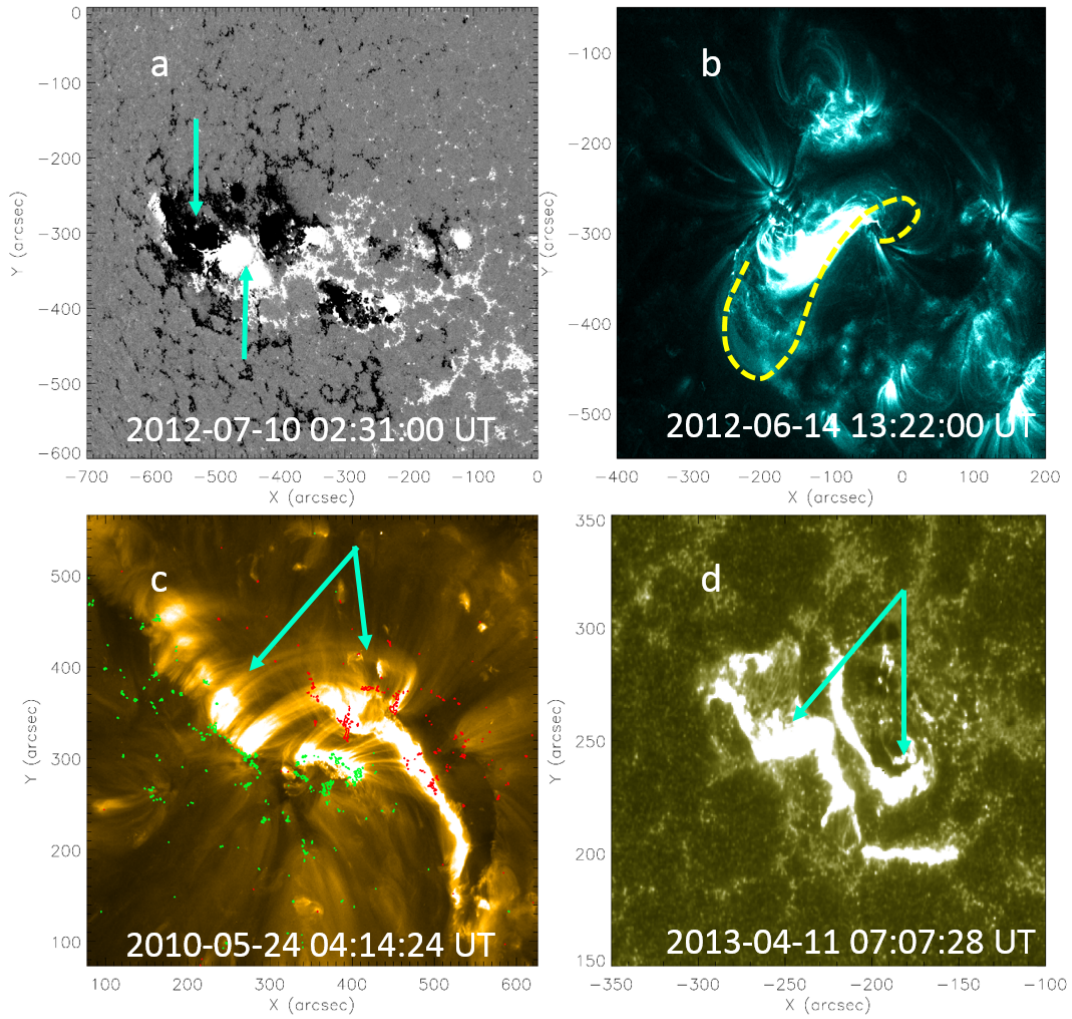


Figure 5.4: Magnetogram and EUV proxies for determining chirality of CME flux ropes. (a) Magnetic tongue configuration (indicated using blue arrows on an SDO/HMI LOS magnetogram) associated with a right-handed flux tube. (b) A forward ‘S’-shaped sigmoid structure (indicated by yellow dashed line on the SDO/AIA 131 Å image) representing a positive twist of associated flux rope. (c) A left-handed skew of overlying coronal loops (pointed by blue arrows on the SDO/AIA 171 Å image) denoting a negative twist of corresponding flux rope. The red and green contours over-plotted on the image refer to negative and positive magnetic field regions with LOS magnetic field intensity $B_{LOS} > \pm 150$ G, respectively. (d) Reverse ‘J’-shaped ribbons pointed by blue arrows on the observed SDO/AIA 1600 Å image. The ribbon structures denote a negative twist of associated flux rope.

projection of the azimuthal component of emerging flux tubes (Ω -loop). The right-handed chirality of flux tubes is indicated by the extension of leading magnetic polarities under the southern edge of trailing magnetic polarities and the left-handed twist is shown by the extension of trailing polarities under the southern edge of leading ones. An example of magnetic tongue observed in an SDO/HMI line-of-sight (LOS) magnetogram is shown in Figure 5.4(a) which indicates a positive twist of the associated flux tube. The magnetic tongue structure is indicated using blue arrows on the Figure.

- **Dextral and sinistral natures of filament structures** (Martin and McAllister, 1996; Martin, 2003): These structures are revealed by the bearing of the legs of filaments, filament barb orientations with respect to their axis, and the fibril orientations in filament channels as observed in H- α images (Martin, Bilimoria, and Tracadas, 1994; Martin, 1998). The dextral and sinistral filaments represent the negative and positive chirality of associated CME flux ropes, respectively.
- **EUUV sigmoids**: These are S-shaped EUV configurations created by the field lines threading the flux-rope associated quasi-separatrix layers (Titov and Démoulin, 1999). A forward (reverse) sigmoid structure is formed due to positive (negative) chirality of magnetic fields. Figure 5.4(b) shows a forward sigmoid structure (indicated using yellow dashed line) on an SDO/AIA 131 Å image,
- **Skew of coronal arcades overlying the neutral lines or filament axes** (McAllister et al., 1995; Martin and McAllister, 1997). It represents the acute angle between the overlying coronal loops and filament axes or the associated polarity inversion lines (PILs). If coronal loops cross over filament channels in sense of a left-handed (right-handed) screw, the loops are characterised as left-hand skewed (right-hand skewed) that indicate the negative (positive) chirality of associated flux ropes (Martin, 1998). The loops are well-observed in EUV wavelengths. Figure 5.4(c) shows a left-hand skewed coronal arcade (indicated using blue arrows) in SDO/AIA 171 Å. It indicates a negative twist of associated flux rope. The green and red contours over-plotted on

the image represent positive and negative magnetic field regions with LOS magnetic field intensity $B_{LOS} > \pm 150$ G, respectively.

- **Structure of flare-ribbons**(Démoulin, Priest, and Lonie, 1996): Flare ribbons are one of the observational signatures of energy release during solar flares. A flare ribbon looks like a reverse (forward) ‘J’ if the corresponding flux rope is left-handed (right-handed). In Figure 5.4(d) a reverse ‘J’-shaped ribbon is shown on an SDO/AIA 1600 Å image. The ribbon structures indicate negative twist of the resulting flux rope. The blue arrows on this Figure show the ribbon structures.
- **Hemispheric helicity rule** (Bothmer and Schwenn, 1998; Pevtsov and Balasubramanian, 2003): It indicates negative (positive) helicity of magnetic structures originated at Sun’s northern (southern) hemisphere.

Determination of axial magnetic field orientation

The flux-rope axis orientations roughly follow the associated PILs (Marubashi et al., 2015) or post-eruption arcades (PEAs; Yurchyshyn, 2008) unless flux ropes undergo significant rotations in the lower corona during their early evolution due to interactions with overlying skewed coronal loops (Lynch et al., 2009). Here we consider the *tilt* measured at $10 R_{\odot}$ using GCS to define the flux rope’s orientation. One may consider that the difference between the flux rope orientations obtained using on-disk observations and GCS *tilt* is about $\pm 30^{\circ}$ (Sarkar, Gopalswamy, and Srivastava, 2020). We further confirm flux rope directions by finding the flux rope footpoints on solar surface using EUV images and magnetograms. The foot points are determined by coronal dimming regions formed during the flux-rope rise times (Mandrini et al., 2005). In Figure 5.5(a) we indicate flux rope foot points by yellow circles on the EUV difference image obtained using observations from SDO/AIA 211 Å. The LOS magnetogram with LOS magnetic field intensity $B_{LOS} > \pm 150$ G is over-plotted on the EUV difference image using red (negative magnetic field region) and green (positive magnetic field region) contours.

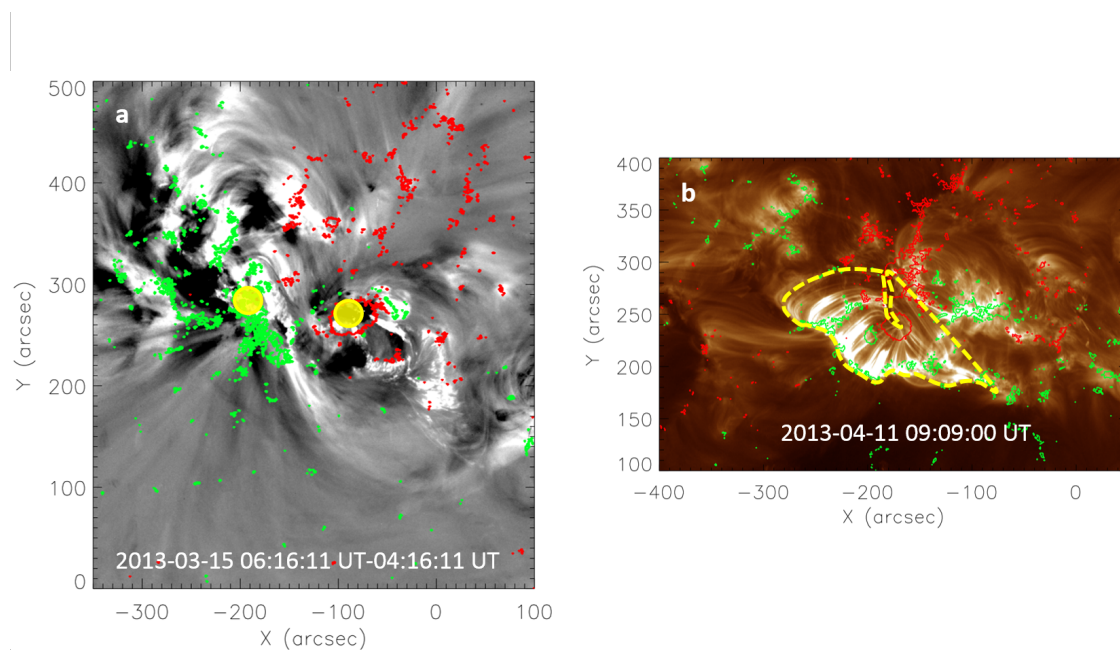


Figure 5.5: (a) An EUV base difference image obtained using SDO/AIA 211 Å observations. The regions rounded by yellow circles denote flux rope foot points. (b) An observation of a PEA in SDO/AIA 193 Å. The PEA foot points are indicated by yellow dotted lines. In both the images, the associated LOS magnetograms with LOS magnetic field intensity $B_{LOS} > \pm 150$ G are over-plotted using green (positive magnetic field) and red (negative magnetic field) contours.

Measuring the axial magnetic field intensity (B'_0) of flux ropes

In Chapter 2 and 3, we discuss the process of estimating the axial magnetic field strength (B_{CME}) of CMEs where they are approximated as cylindrical force-free flux ropes and the magnetic reconnection plays a dominant role in the formation of CME flux ropes. Here we follow the same procedure that requires CME's source-region reconnection flux (F_{rec}) which is equivalent to the poloidal or azimuthal flux (F_{pcme}) of CME flux rope (Longcope et al., 2007; Qiu et al., 2007), the length (L_{CME}) & radius (R_{CME}) of CME to determine its axial magnetic field intensity. The reconnection flux F_{rec} is obtained using Post eruption arcade (PEA) method discussed in Gopalswamy et al. (2017a) and Gopalswamy et al. (2017b). The poloidal flux of CMEs is conserved during their interplanetary propagation (Qiu et al., 2007; Hu et al., 2014; Gopalswamy et al., 2017a) unless they significantly reconnect with ambient interplanetary magnetic fields (IMFs). Thus, B'_0 is estimated using,

$$B'_0 = B_{CME} \times \frac{R_{CME}^2}{R_{MC}^2(0)}. \quad (5.9)$$

In Figure 5.5(b) a PEA region is indicated by yellow dashed line on SDO/AIA 193 Å image where the positive and negative magnetic field regions are shown by green and red contours, respectively.

5.2.4 Estimation of the arrival time and speed of CMEs

A reliable prediction of the arrival time (t_{ar}) and speed (V_{ar}) of CMEs are necessary in determining the profile of MCs. Enhancing the accuracy in predicting t_{ar} and V_{ar} is beyond the scope of this study. Thus, t_{ar} and V_{ar} are estimated utilizing the pre-existing drag-based ensemble model (DBEM; Dumbović et al., 2018) – an upgraded version of a simple kinematic drag based model (DBM; Vršnak et al., 2013) established using the concept of aerodynamic drag on interplanetary propagation of CMEs. The model DBEM produces possible distributions of V_{ar} and t_{ar} by employing ensemble modeling of CME propagation. It assumes CME to be a cone structure with semicircle leading edge spanning over its angular width where the structure flattens with the CME's interplanetary evolution (Žic, Vršnak, and Temmer, 2015). It considers solar wind speed (V_{sw}) and drag parameter (γ) to be constant beyond the distance $15 R_{\odot}$. This is because beyond $15 R_{\odot}$ CMEs propagate through an

isotropic solar wind having a constant velocity. Also, the rate of the fall-off of solar wind density is similar to the rate of the self-similar expansion of CMEs (Vršnak et al., 2013; Žic, Vršnak, and Temmer, 2015). To perform a near-real time prediction of ICME's arrival, DBEM is available at Hvar Observatory website as an online tool (<http://phyk039240.uni-graz.at:8080/DBEMv2/dbem.php>) which is a product of European Space Agency (ESA) space situational awareness (SSA). The inputs to the model are the speed, half angular width, propagation longitude of CMEs observed at a particular time and specific solar distance along with the radial speed of solar wind and drag parameter including their uncertainties. The CME's latitude information is not necessary for DBEM because DBEM is a two dimensional model operated in solar ecliptic plane.

We prepare an ensemble of n measurements of a single CME, and m number of V_{sw} & γ using their uncertainty ranges. Thus, a total number of $n.m^2$ input sets are prepared for analysis. After performing $n.m^2$ number of runs the DBEM produces distributions of $n.m^2$ number of V_{ar} and t_{ar} which vary from $V_{ar,l}$ to $V_{ar,u}$ and $t_{ar,l}$ to $t_{ar,u}$, respectively. We use Stereoscopic CME Analysis Tool (StereoCAT; LaSota, 2013) developed by Community Coordinated Modeling Center (CCMC) to obtain the three-dimensional speed, projected angular width, propagation longitude of CMEs at a distance $R_d > 15R_{\odot}$ and the time when CMEs reach at the distance R_d . The StereoCAT tool does not capture the volumetric structure of a CME but it is based on the triangulation of CME's transient features manually observed in two separate coronagraph field of views. In a basic two-time-point measurement mode of StereoCAT, a CME's leading edge is tracked in two different times using two different (STEREO/SECCHI or/and SOHO/LASCO coronagraphs) view points. Following the algorithm described in Mays et al. (2015) CME's triangulated 3D speed is estimated using its leading-edge height-time information. To prepare an ensemble of CME measurements, the height of the leading edge of CME is repeatedly tracked (say, k times) in two separate coronagraph view points during two different times. Thus, $n = K^2$ set of 3D CME speed, longitude, and projected angular width are obtained. For simplicity we use constant values of V_{sw} and γ for all CMEs as considered by Dumbović et al. (2018). The study considered the V_{sw} and γ as equal to 350 ± 50 km/s and $0.1 \pm 0.05 \times 10^{-7}$ km $^{-1}$, respectively. The average V_{sw} is chosen

as 350 km/s because of the weak solar activity of cycle 24 (McComas et al., 2013) and the value of γ is derived empirically in previous studies by Vršnak et al. (2013) and Vršnak et al. (2014). It is noticed that choosing $\gamma = 0.1 \times 10^7 \text{ km}^{-1}$ provides a good agreement between the results obtained using complex numerical 3D MHD model – WSA-ENLIL+Cone model (Odstroil, Riley, and Zhao, 2004) and DBM (Vršnak et al., 2014).

5.2.5 Coordinate conversion of magnetic field vectors

At 1 AU, the inclination angle (θ_{MC}) of MCs is considered to be equivalent to the *tilt* of associated CMEs and the azimuthal angle (ϕ_{MC}) of MCs are determined using CME propagation longitudes (ϕ_{HG}) obtained at $10 R_{\odot}$. In order to express B_{az} , B_{ax} and B_{ρ} in Geocentric Solar Ecliptic (GSE) coordinate system (a Cartesian coordinate system where \hat{z} is perpendicular to the Sun-Earth plane, and \hat{x} is parallel to the Sun-Earth line and positive toward the Sun) that is majorly used to represent the magnetic field vectors of ICMEs at 1 AU, we transform the field vectors from local cylindrical to Cartesian coordinate system. At first B_{az} , B_{ax} , and B_{ρ} are converted to $B_{x,cl}$, $B_{y,cl}$ and $B_{z,cl}$ which are in local Cartesian coordinate (\hat{x}_{cl} , \hat{y}_{cl} , \hat{z}_{cl}) system originating at MC axis. Finally, using θ_{MC} & ϕ_{MC} , the magnetic field vectors $B_{x,cl}$, $B_{y,cl}$ and $B_{z,cl}$ are transformed to B_x , B_y and B_z .

5.3 Results: Model validation using observed MC events

As a proof of concept we validate our model by investigating ten different Earth-directed MCs appearing as flux ropes at near-Sun region, having clearly identified solar sources and in situ magnetic profiles. At near-Earth region (L1 Lagrangian point) MCs are observed using Magnetic Field Experiment (MAG) instrument of the Advanced Composition Explorer (ACE) spacecraft. The events are selected from the Richardson & Cane ICME catalog (Richardson and Cane, 2010, <http://www.srl.caltech.edu/ACE/ASC/DATA/level3/icmetable2.html>) keeping in mind that at 1 AU they maintain the MC properties suggested by Burlaga et

al. (1981) throughout their interval and their associated CMEs appear as isolated magnetic structures in near-Sun observations.

5.3.1 Preparation of model inputs

We manually identify each of the MC associated CMEs and locate their solar sources utilizing their coronal signatures. Using GCS model we obtain CME's geometrical parameters, such as, θ_{HG} , ϕ_{HG} , AW , $tilt$, and κ at $10 R_{\odot}$ and tabulate them in Column 5-9 of Table 5.1, respectively. We define CME initiation time (CME_{start}) as the moment when the CMEs are first identified at SOHO/LASCO C2 field of view. In Column 1 and 2 the event numbers (Ev no.) and CME_{start} are mentioned, respectively. Column 3 and 4 contain the start (MC_{start}) and end time (MC_{end}) of MCs adapted from the Richardson & Cane ICME catalog.

Utilizing ambient solar wind speed, drag parameter, CME's extrapolated 3D velocity, longitude and projected angular width measured at $21.5 R_{\odot}$ as input to DBEM, we estimate the arrival time t_{ar} ($t_{ar,l} \leq t_{ar} \leq t_{ar,u}$) and speed V_{ar} ($V_{ar,l} \leq V_{ar} \leq V_{ar,u}$) of MCs. The arrival time t_{ar} has the smallest deviation (Δt_{ar}) from its real value. In Column 2, 3, 4 and 5 of Table 5.2 we provide the deprojected speed (V_{CME}) of CMEs at $21.5 R_{\odot}$ with uncertainties, t_{ar} , V_{ar} , and Δt_{ar} , respectively. The corresponding event numbers are given in Column 1. We believe that the high values of Δt_{ar} obtained for the cases of event 5 and 8 are resulted from the overestimation of CME velocities. Therefore, for these cases we use the observed V_{ar} and t_{ar} as input to the model.

To determine flux-rope types, we obtain their chirality, axis orientations and axial magnetic field directions. The multi-wavelength proxies discussed in Section 5.2.3 are examined for all MCs to infer their chirality. In Table 5.3 we summarise the near-Sun flux rope magnetic properties where Column 2 shows the chirality ('+1' stands for right-handedness and '-1' represents left-handedness) of flux ropes inferred using the proxies – magnetic tongue, filament natures, sigmoids, skew of coronal loops, flare ribbons, and hemispheric helicity rule. Next, we find the flux-rope axis inclinations using the $tilt$ of CMEs and direction of MC axial fields derived by observing the coronal dimming regions in EUV difference images combined with the magnetograms. Finally, the axial magnetic field intensity of the associated

Table 5.1: Near-Sun observations of the geometrical parameters of CME flux ropes, their initiation time (CME_{start}), and associated MCs' start (MC_{start}) and end times (MC_{end}).

Ev no.	CME_{start} (UT)	MC_{start} (UT)	MC_{end} (UT)	θ_{HG} ($^{\circ}$)	ϕ_{HG} ($^{\circ}$)	$tilt$ ($^{\circ}$)	AW ($^{\circ}$)	κ
(1)	(2)	(3)	(4)	(5)	(6)	(7)	(8)	(9)
1	2010/05/24 14:06:00	2010/05/28 20:46:00	2010/05/29 16:27:00	0	5.3	-53.3	36	0.27
2	2011/06/02 08:12:00	2011/06/05 01:50:00	2011/06/05 09:21:00	-7.8	-11.8	55.3	34	0.15
3	2012/02/10 20:00:00	2012/02/14 20:24:00	2012/02/16 05:34:00	28	-23	-68.8	50	0.30
4	2012/06/14 14:12:00	2012/06/16 22:00:00	2012/06/17 14:00:00	0	-5	30.7	76	0.30
5	2012/07/12 16:48:00	2012/07/15 06:00:00	2012/07/17 05:00:00	-8	14	53.1	60	0.66
6	2012/11/09 15:12:00	2012/11/13 09:44:00	2012/11/14 02:49:00	2.8	-4	-2	36	0.20
7	2013/03/15 07:12:00	2013/03/17 14:00:00	2013/03/18 00:45:00	-6.5	-10	-74.4	51	0.27
8	2013/04/11 07:24:00	2013/04/14 16:41:00	2013/04/15 20:49:00	-5.5	-15	68.2	74	0.24
9	2013/06/02 20:00:00	2013/06/06 14:42:00	2013/06/07 15:20:00	-1.7	7	75.5	36	0.21
10	2013/07/09 15:12:00	2013/07/13 04:39:00	2013/07/15 00:00:00	2	3	-37.5	36	0.36

CMEs are derived using F_{pcme} and flux rope geometrical parameters. The Column 3 and 4 of Table 5.3 correspond to the flux rope type $type_{ns}$ and F_{pcme} of near-Sun flux ropes, respectively.

Table 5.2: A table containing the predicted arrival time t_{ar} , speed V_{ar} of MCs and the difference Δt_{ar} between the actual arrival time and the predicted values.

Ev no.	V_{CME} (km/s)	t_{ar} (UT)	V_{ar} (Km/s)	Δt_{ar} (Hr)
(1)	(2)	(3)	(4)	(5)
1	489±28	2010-05-28 12:19:05	465	8.5
2	934±546	2011-06-04 14:52:16	650	10.96
3	675±51	2012-02-14 07:42:02	446	12.7
4	1165±19	2012-06-16 16:07:34	669	5.87
5	1353±90	2012-07-14 14:25:02	765	15.6
6	558±35	2012-11-13 00:25:36	469	9.3
7	1237±164	2013-03-17 06:38:13	749	7.6
8	1171±59	2013-04-13 08:39:59	710	32
9	440±57	2013-06-06 13:35:04	426	1.11
10	505±25	2013-07-13 02:48:49	465	1.84

5.3.2 Model outputs

Using the near-Sun CME observations as input to the constant- α force-free cylindrical flux rope model that expands self-similarly in radial directions we estimate the magnetic field vectors of the associated MCs intersecting the spacecraft at 1 AU. To incorporate the ambiguities involved in measurements of propagation direction, inclination, and size of CMEs we utilize the uncertainty range of those parameters as input to our model. We prepare ten different random input sets of each MC where the input parameter values are within $\pm 10^\circ$ of measured propagation direction and *tilt*, and $\pm 10\%$ of estimated κ value. The magnetic field vectors are derived using each of the input sets. Thus, we obtain ten different magnetic profiles for every event and measure the rms differences between observed and predicted magnetic vectors. The normalised rms difference (Δ_{rms}) is calculated using the ratio of δB and B_{max}^o , where B_{max}^o is the maximum observed magnetic field intensity and δB

Table 5.3: Magnetic properties of CME flux ropes as derived using on disk observations.

Ev no.	Chirality	$type_{ns}$	F_{pcme} ($\times 10^{21}$ Mx)
(1)	(2)	(3)	(4)
1	-1	NWS	2.15
2	1	WNE	1.81
3	1	ESW	2
4	1	NES	8.45
5	1	ESW	14.10
6	1	NES	2.47
7	1	ESW	4.10
8	-1	ENW	3.72
9	-1	WSE	1.75
10	-1	NWS	3.50

is defined by,

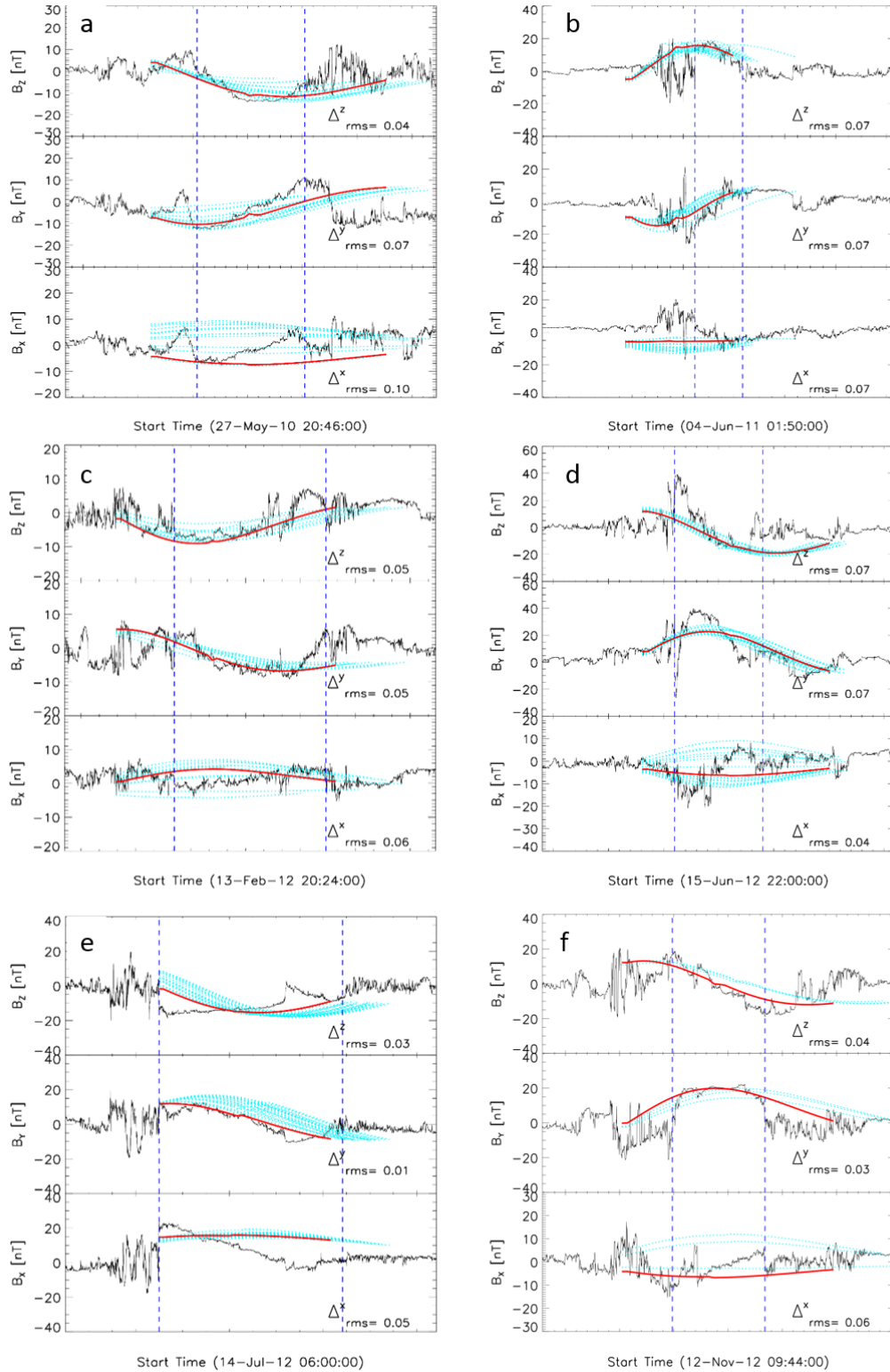
$$\delta B = \sqrt{\frac{\sum_i (\mathbf{B}^o(\mathbf{t}_i) - \mathbf{B}^p(\mathbf{t}_i))^2}{N}}. \quad (5.10)$$

Here $\mathbf{B}^o(\mathbf{t}_i)$ and $\mathbf{B}^p(\mathbf{t}_i)$ are the observed and predicted magnetic field vectors, respectively, and $i = 1, 2, 3 \dots N$ with N being the total number of data points corresponding to magnetic vectors. We report θ_{MC} , ϕ_{MC} and impact parameter corresponding to those predicted profiles having minimum value of Δ_{rms} . The Δ_{rms} is estimated for B_x , B_y and B_z , separately and represented by Δ_{rms}^x , Δ_{rms}^y and Δ_{rms}^z , respectively. In Figure 5.6 we display the predicted magnetic vectors obtained from the model along with the in situ data measured at L1 by ACE/MAG instrument for ten MCs. The observed solar wind magnetic field vectors are shown in black whereas the red curves over plotted on them during MC intervals (indicated by dashed blue vertical lines) represent the predicted fields having minimum value of Δ_{rms} . The uncertainties in predictions resulted from errors in input estimations are shown using sky blue dotted curves. The latitude, longitude, normalised impact parameter $Y_0 = \frac{p}{R_{MC}(0)}$ corresponding to the minimum value of Δ_{rms} , i.e., Δ_{rms}^m of

Table 5.4: Predicted MC parameters, its comparison with observed magnetic vectors, and the type of MCs as observed by in situ observations.

Ev no.	θ_{MC}^m ($^\circ$)	ϕ_{MC}^m ($^\circ$)	Y_0^m	Δ_{rms}^m	$\bar{\Delta}_{rms}$	$type_{ne}$	C_{or}
(1)	(2)	(3)	(4)	(5)	(6)	(7)	(8)
1	-61.73	276.61	0.52	0.14	0.17±0.03	NWS	<i>y</i>
2	47.74	299.56	-0.53	0.16	0.18±0.02	WNE	<i>y</i>
3	-60.91	302.65	-0.34	0.10	0.13±0.01	ESW	<i>y</i>
4	-31.16	87.15	-0.19	0.11	0.12±0.006	NES	<i>y</i>
5	-62.64	150.33	0.86	0.06	0.09±0.01	ESW	<i>y</i>
6	5.13	82.28	0.09	0.07	0.18±0.09	NES	<i>y</i>
7	-74.49	298.24	0.86	0.20	0.38±0.13	SWN	<i>n</i>
8	78.17	295.48	-0.49	0.08	0.13±0.02	ENW	<i>y</i>
9	-72.40	102.17	0.52	0.10	0.12±0.02	WSE	<i>y</i>
10	-34.45	262.84	-0.54	0.08	0.09±0.02	NWS	<i>y</i>

individual cases are denoted by θ_{MC}^m , ϕ_{MC}^m and Y_0^m , respectively. The $\bar{\Delta}_{rms}$ represents the average value of Δ_{rms} for each cases along with standard deviations. We mention the values of θ_{MC}^m , ϕ_{MC}^m , Y_0^m , Δ_{rms}^m and $\bar{\Delta}_{rms}$ of ten MCs in Column 2, 3, 4, 5 and 6 of Table 5.4, respectively. The magnetic type of the MCs ($type_{ne}$) as observed by ACE are noted in Column 7. To compare the magnetic field orientation in predicted and observed flux ropes at 1 AU, we utilise the parameter C_{or} in Column 8. Here ‘*y*’ and ‘*n*’ indicate a match and mismatch in field line orientation of near-Sun and near-Earth flux ropes, respectively. The event numbers (Ev no.) are mentioned in Column 1.



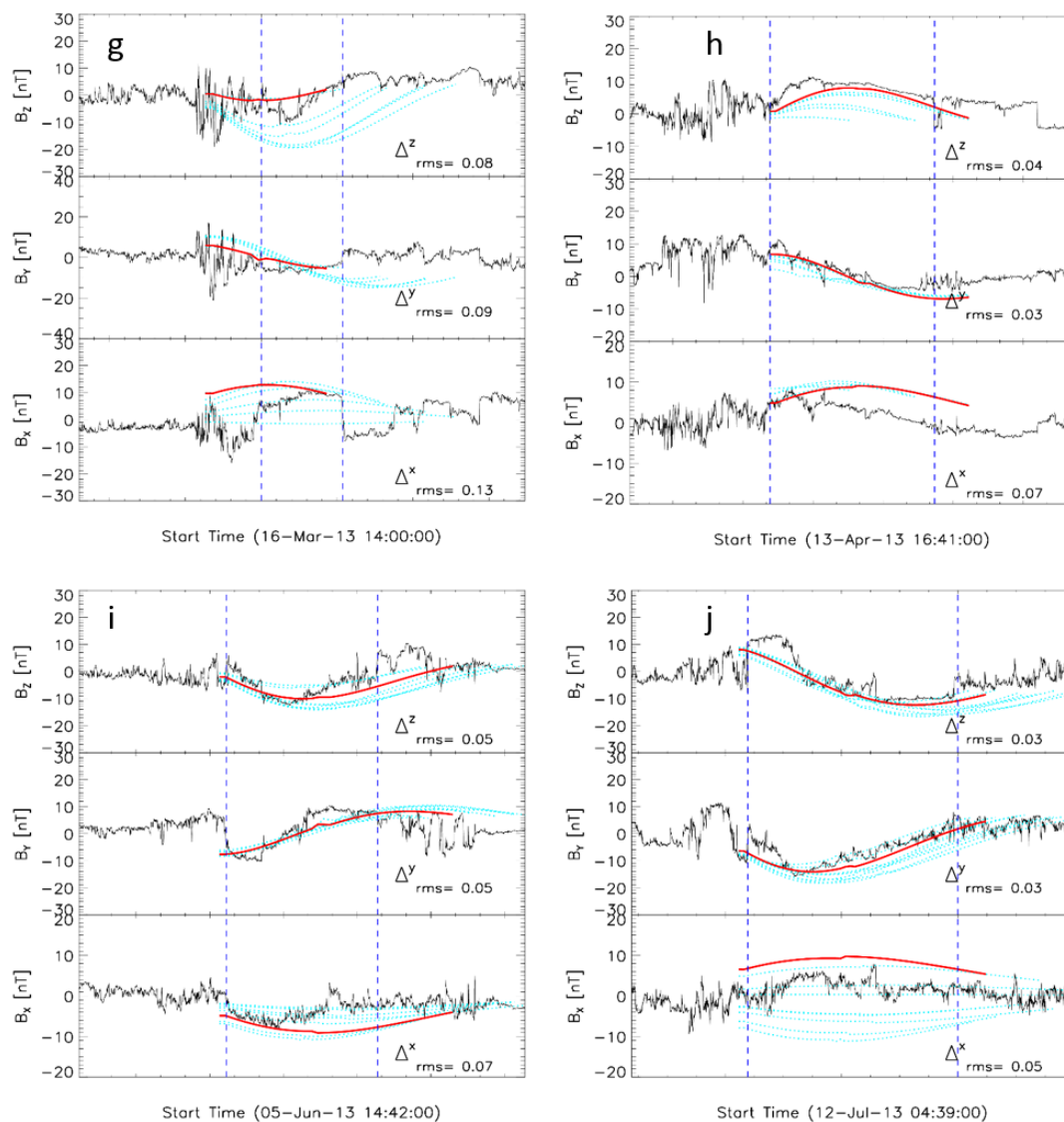


Figure 5.6: Magnetic vectors of ten MCs as observed by ACE spacecraft. The red curves represent the predicted magnetic vectors having best match with observed magnetic vectors. The sky blue dotted curves show uncertainty in predictions. The blue vertical lines over-plotted on the images denote the start and end time of MCs as noted by Richardson & Cane ICME catalog. The rms differences Δ_{rms}^x , Δ_{rms}^y , and Δ_{rms}^z between observed and predicted magnetic vectors B_x , B_y and B_z are mentioned on the plot.

5.4 Discussion

We present an approach for forecasting the magnetic profiles of MCs assuming self-similar radial expansion where the MC's arrival at Earth is predicted based on the concept of MHD drag. Our model performs better than the previous analytical and semi-analytical models because we constrain it totally using near-Sun observations and by estimating MC's radial expansion speed profile, we determine their radial extents too. Gopalswamy et al. (2015a) obtained the median as well as average values of the radial expansion speed of 65 MCs belonging to solar cycle 24 as about 25 km/s. As the events used to validate our model are of same solar cycle (cycle 24), for simplicity, we consider a constant average radial expansion speed of 25 km/s for each of the MCs.

Sarkar, Gopalswamy, and Srivastava (2020) noted that MC's B_y and B_z components are not sensitive to small variations in its propagation direction and tilt. In our study we also observe that for most of the cases the uncertainty in CME's direction of propagation and tilt leads to a significant variation in predicted B_x , not in B_y and B_z . The inaccuracy in predicting magnetic vectors inside an MC increases when the MC axis is almost parallel to the Sun-Earth line.

Using DBEM, Dumbović et al. (2018) estimated the arrival time and speed of 25 CMEs and obtained the mean absolute error (MAE) as 14.3 hours. In our study we find that the MAE of Event no. 5 and 8 are greater than 14.3 hours. Significant differences between observed and predicted arrival time and speed for these events may result possibly from model limitations and overestimation of associated CME initial speeds (Dumbović et al., 2018). Mays et al. (2015) suggested that the speed of fast CMEs are overestimated due to limited number of their measurement points. The overestimated CME speed results observed under-forecast of transit times and over-forecast of arrival speed. Therefore, for these two events we consider their observed arrival time and speed rather than their predicted values.

From Table 5.4 we note that the values of Δ_{rms}^m and $\bar{\Delta}_{rms}$ corresponding to Event no. 7 are $\sim 80\%$ higher than their average values obtained using nine other events. Also, the ' n ' in Column 8 corresponding to this event indicates a mismatch in the orientation of field lines inside the predicated and observed flux ropes. Pal et al. (2017) obtained the θ_{MC} of the event as -24° by least-square fitting the event

with an expanding cylindrical flux rope, whereas using GCS method we measure the tilt of the event associated CME at $10 R_{\odot}$ to be -74° . This is consistent with the fact that interaction with the surrounding solar wind stream may cause variations in the axis orientation of MCs while it propagates from $10 R_{\odot}$ to 1 AU. Heinemann et al. (2019) observed such interaction between CME and high speed streams (HSS) emanating from the coronal holes changing the CME properties en route through the heliosphere. Such interaction may deform, kink or rotate CME flux ropes (Riley and Crooker, 2004; Isavnin, Vourlidas, and Kilpua, 2013; Yurchyshyn, 2008; Sahade, Cécere, and Krause, 2020). From the Heliophysics Feature Catalogue (HFC; Bonnin et al., 2013) which extracts solar and heliophysics feature information from images using automated recognition codes, we find the presence of a coronal hole on the southern hemisphere of the Sun during the Sun-Earth propagation of the CME associated with Event no. 7. Also, we find the average speed of ambient solar wind during the MC's Sun-Earth propagation as 500 km/s which is greater than the average speed of background solar wind in normal conditions. Thus, we infer that the CME's interaction with the HSS coming from a coronal hole located on the solar southern hemisphere may have rotated the CME and transformed it from a high-inclination to low-inclination flux rope.

This is to note that several assumption and simplification made our approach for predicting MC magnetic field vector computationally strong as well as weak as this approach is unable to capture the detail magnetic nature of complicated space weather events. Therefore, a statistical investigation is required to understand the capability of this model in accurately predicting the magnetic field vectors of CMEs.

5.5 Conclusions

In this chapter we develop a methodology to predict the magnetic vectors of MCs near Earth using an analytical model completely constrained by near-Sun observations. The analytical model used here is a linear force-free model in cylindrical coordinate system. The model includes estimates of MC's axial magnetic field intensity, orientation, radial expansion profile to derive MC's propagation speed and radial extent. Additionally, we predict the arrival time and speed of MCs using a

drag based model that utilizes the deprojected speed of CMEs, ambient solar wind velocity and drag parameter. To validate our model we analyse ten events having clearly identified flux rope characteristics at near-Sun and near-Earth observations. Our results show a good match between predicted and observed magnetic profiles of MCs. The pre-existing semi-analytical and analytical models do not incorporate MC's arrival information. Therefore, the MC's arrival time, speed and radial extent are considered as free parameters in those models. Although the INFROS model considers MC's expanding nature and can predict the strength of axial magnetic field, it does not involve estimates of MC arrival time, propagation speed and predict radial extent. In this context, we conclude that our methodology leads to a substantial improvement in predicting the space weather relevant parameters of Earth directed MCs.

Chapter 6

Concluding remarks

The principal ambition of this dissertation is to investigate and thereby improve the current understanding of the origin and evolution of the properties of the dominant driver of space weather - coronal mass ejections (CMEs) – and to predict their geoeffectiveness. The thesis begins with an overview of space weather, its origin, drivers and potential impacts on Earth and space-reliant technologies. The geoeffective properties of CMEs are examined thoroughly in order to have a proper understanding of their influence on the Earth’s magnetosphere. By analysing CMEs using remote-sensing and in situ observations together with an analytical model, we explore the origin of CME properties and their distortions during interplanetary propagation. Our attempt to predict the geoeffectiveness of CMEs has significant implications for forecasting space weather.

The geoeffective properties of CMEs are primarily analysed within the Sun-Earth domain to investigate their sources and understand their evolution. Utilizing properties of near-Sun CMEs, prediction of their magnetic structures is performed. In Chapter 2 and 3 we analyse the geoeffective properties of CMEs in the context of kinetic and magnetic properties of their sources. At the corona, we derive the magnetic information of CMEs using CME-associated post-eruption arcades (PEAs). We observe a good correspondence between CME kinematics and flare reconnection flux derived using PEAs. It suggests that being a proxy for the energy associated with eruptions, the reconnection flux drives the CME kinematics. A significant correlation found between the magnetic pressure of CMEs and their kinetic energy is evident from the fact that the rapid expansion of CME occurs due

to the higher magnetic pressure of CME flux rope relative to that of the background magnetic field. By comparing the magnetic properties of CMEs and their interplanetary counterparts, we suggest that CMEs are primarily formed due to low-coronal magnetic reconnection at their solar sources and reconnection primarily transfers magnetic properties such as magnetic flux and helicity to CME flux ropes. During interplanetary propagation, CMEs may lose their initial magnetic flux via magnetic reconnection, which in some cases reduce their geoeffectiveness. The Sun's unsigned open flux that regulates the IMF intensity is found to be significantly correlated with the eroded flux of CMEs. Thus, Chapter 4 provides a novel connection between the solar cycle variation of the heliospheric open flux and space weather in the vicinity of solar system planets. Finally in Chapter 5, we present an approach for forecasting magnetic vectors within Earth-directed segment of CMEs using an analytical model completely constrained by near-Sun observations. Our suggested model estimates the radial extent of CMEs while crossing the Earth utilizing a velocity expansion profile. Thus, we attempt to predict CME's southward magnetic field component, i.e. B_z in order to forecast its geoeffectiveness.

To determine CME's near-Sun magnetic field intensity in Chapter 5, we utilise the FRED technique described in Section 2.2.1. To estimate the ambient solar wind magnetic field intensity in Chapter 4, we extrapolate the coronal field assuming the magnetic field to be potential. It is to be noted that extracting quantitative information of solar coronal magnetic field utilizing observations is pretty much challenging because the corona is optically thin. To determine the internal magnetic structure of CMEs that are not accompanied by flare ribbons or PEAs, coronal polarimetric measurements (Gibson, Rachmeler, and White, 2017) and the measurement of Faraday rotation of distant radio sources like pulsars (Howard et al., 2016) may be used. For coronal polarimetric measurements, capturing weak coronal signals is necessary. To measure the Faraday rotation, a constant radio source needs to be located behind the Sun. Through these measurements, a continuous probing of coronal field that is necessary for systematic space weather forecasting may be achieved. We anticipate that the availability of routine coronal field observations (DKIST and Aditya-L1 mission) would significantly add to the quantitative tools and methodologies explored in this thesis and positively impact our ability to un-

derstand the origin of space weather events.

In order to predict CMEs kinematics and properties in the near-Earth space environment accurately, the deflection and rotation of CME flux-ropes during their interplanetary propagation need to be observed. Observations of solar wind plasma and magnetic field at various locations in the interplanetary medium is now possible using recently launched satellites like Parker Solar Probe (PSP; Fox et al., 2016) that is to venture up to $\sim 9 R_{\odot}$ from the Sun, BepiColombo (Benkhoff et al., 2010) that is launched in Mercury’s orbit, and Solar Orbiter (SolO; Farrugia et al., 1992) that can reach as close as $\sim 60 R_{\odot}$ from the Sun center with 25° inclination to the solar ecliptic plane. We anticipate that simultaneous, multi-viewpoint observations of the propagation dynamics of an interplanetary flux rope would add critical constraints to predictive models and thus improve them.

For reliable model-based predictions of CME arrival time and speed, their intrinsic magnetic driving and their interaction with the ambient solar wind during the heliospheric propagation of CMEs need to be understood and quantified. Models – such as the 3D magneto-hydrodynamic (MHD) heliospheric model (Odstrcil, 2003) – which are properly constrained and data driven – may be used in this context.

With concurrent developments in modelling and multi-vantage point observations of the Sun-Earth domain becoming available, we are hopeful of rapid strides in our understanding of planetary space environments, and in our ability to forecast space weather.

Bibliography

- Al-Haddad, N. et al. (Sept. 2011). “On the Internal Structure of the Magnetic Field in Magnetic Clouds and Interplanetary Coronal Mass Ejections: Writhe versus Twist”. In: *The Astrophysical Journal* 738, L18, p. L18.
- Alfvén, Hannes (1942). “Existence of electromagnetic-hydrodynamic waves”. In: *Nature* 150.3805, pp. 405–406.
- Alksne, Alberta Y and David L Webster (1970). “Magnetic and electric fields in the magnetosheath”. In: *Planetary and Space Science* 18.8, pp. 1203–1212.
- Allen, Joe et al. (1989). “Effects of the March 1989 solar activity”. In: *Eos, Transactions American Geophysical Union* 70.46, pp. 1479–1488.
- Altschuler, Martin D. and Gordon Newkirk (1969). “Magnetic fields and the structure of the solar corona”. In: *Solar Physics* 9.1, pp. 131–149.
- Andrews, Micahel D (2001). “LASCO and EIT observations of the Bastille Day 2000 solar storm”. In: *Solar Physics* 204.1-2, pp. 179–196.
- Antiochos, SK, CR DeVore, and JA Klimchuk (1999). “A model for solar coronal mass ejections”. In: *The Astrophysical Journal* 510.1, p. 485.
- Antiochos, Spiro K, JL Burch, and Robert L Carovillano (1999). *Sun-Earth Plasma Connections*. Wiley Online Library.
- Antunes, Alex, Arnaud Thernisien, and Amos Yahil (2009). “Hybrid Reconstruction to Derive 3D Height–Time Evolution for Coronal Mass Ejections”. In: *Solar Physics* 259.1-2, p. 199.
- Asgari-Targhi, M. et al. (2013). “The spatial and temporal dependence of coronal heating by Alfvén wave turbulence”. In: *The Astrophysical Journal* 773.2, p. 111.
- Babcock, HW (1961). “The Topology of the Sun’s Magnetic Field and the 22-YEAR Cycle.” In: *The Astrophysical Journal* 133, p. 572.

- Ballegooijen, A. A. van, E. R. Priest, and D. H. Mackay (2000). “Mean Field Model for the Formation of Filament Channels on the Sun”. In: *Astrophys. J.* 539.2, pp. 983–994.
- Balogh, A. et al. (May 1995). “The Heliospheric Magnetic Field Over the South Polar Region of the Sun”. In: *Science* 268, pp. 1007–1010.
- Batchelor, GK (1967). *An Introduction to Fluid Dynamics*, Cam.
- Bein, BM et al. (2011). “Impulsive acceleration of coronal mass ejections. I. Statistics and coronal mass ejection source region characteristics”. In: *The Astrophysical Journal* 738.2, p. 191.
- Benkhoff, Johannes et al. (2010). “BepiColombo—Comprehensive exploration of Mercury: Mission overview and science goals”. In: *Planetary and Space Science* 58.1-2, pp. 2–20.
- Berger, M. A. (Apr. 2003). “Topological quantities in magnetohydrodynamics”. In: *Advances in Nonlinear Dynamics*. Ed. by A. Ferriz-Mas and M. Núñez. CRC Press, pp. 345–374.
- Berger, Mitchell A (1984). “Rigorous new limits on magnetic helicity dissipation in the solar corona”. In: *Geophysical & Astrophysical Fluid Dynamics* 30.1-2, pp. 79–104.
- (1999). “Introduction to magnetic helicity”. In: *Plasma Physics and Controlled Fusion* 41.12B, B167.
- Berger, Mitchell A. (Jan. 2005). “Magnetic Helicity Conservation”. In: *Highlights of Astronomy* 13, p. 85.
- Berger, Mitchell A. and George B. Field (1984a). “The topological properties of magnetic helicity”. In: *Journal of Fluid Mechanics* 147, 133–148.
- Berger, Mitchell A and George B Field (1984b). “The topological properties of magnetic helicity”. In: *Journal of Fluid Mechanics* 147, pp. 133–148.
- Bhowmik, Prantika and Dibyendu Nandy (2018). “Prediction of the strength and timing of sunspot cycle 25 reveal decadal-scale space environmental conditions”. In: *Nature Communications* 9, 5209, p. 5209.
- Biermann, Ludwig (1965). “The Plasma in Interplanetary Space”. In: *Proceedings of the Plasma Space Science Symposium*. Springer, pp. 91–98.

- Birn, J. et al. (Mar. 2001). “Geospace Environmental Modeling (GEM) magnetic reconnection challenge”. In: *Journal of Geophysical Research (Space Physics)* 106, pp. 3715–3720.
- Blanco-Cano, X et al. (2016). “Interplanetary shocks and foreshocks observed by STEREO during 2007–2010”. In: *Journal of Geophysical Research (Space Physics)* 121.2, pp. 992–1008.
- Bobra, M. G. et al. (Sept. 2014). “The Helioseismic and Magnetic Imager (HMI) Vector Magnetic Field Pipeline: SHARPs - Space-Weather HMI Active Region Patches”. In: *Solar Physics* 289, pp. 3549–3578.
- Bonnin, Xavier et al. (2013). “The Heliophysics Feature Catalogue, a tool for the study of solar features”. In: *Proceedings of the International Astronomical Union* 8, pp. 512–514.
- Borgazzi, A et al. (2009). “Dynamics of coronal mass ejections in the interplanetary medium”. In: *Astronomy & Astrophysics* 498.3, pp. 885–889.
- Bosman, E. et al. (Nov. 2012). “Three-Dimensional Properties of Coronal Mass Ejections from STEREO/SECCHI Observations”. In: *Solar Physics* 281, pp. 167–185.
- Bothmer, V. and R. Schwenn (1998). “The structure and origin of magnetic clouds in the solar wind”. In: *Annales Geophysicae* 16.1, pp. 1–24.
- Brueckner, G. E. et al. (Dec. 1995). “The Large Angle Spectroscopic Coronagraph (LASCO)”. In: *Solar Physics* 162, pp. 357–402.
- Burkepile, J. T. et al. (2004). “Role of projection effects on solar coronal mass ejection properties: 1. A study of CMEs associated with limb activity”. In: *Journal of Geophysical Research (Space Physics)* 109.A3.
- Burlaga, L. et al. (Aug. 1981). “Magnetic loop behind an interplanetary shock - Voyager, Helios, and IMP 8 observations”. In: *Journal of Geophysical Research (Space Physics)* 86, pp. 6673–6684.
- Burlaga, L et al. (1981). “Magnetic loop behind an interplanetary shock: Voyager, Helios, and IMP 8 observations”. In: *Journal of Geophysical Research (Space Physics)* 86.A8, pp. 6673–6684.
- Burlaga, L. F. (July 1988). “Magnetic clouds and force-free fields with constant alpha”. In: *Journal of Geophysical Research (Space Physics)* 93, pp. 7217–7224.

- Burlaga, L. F., A. J. Hundhausen, and X.-P. Zhao (Oct. 1981). “The coronal and interplanetary current sheet in early 1976”. In: *Journal of Geophysical Research (Space Physics)* 86, pp. 8893–8898.
- Burlaga, LF (1988). “Magnetic clouds and force-free fields with constant alpha”. In: *Journal of Geophysical Research (Space Physics)* 93.A7, pp. 7217–7224.
- (1991). “Intermittent turbulence in the solar wind”. In: *Journal of Geophysical Research (Space Physics)* 96.A4, pp. 5847–5851.
- Burton, R. K., R. L. McPherron, and C. T. Russell (Nov. 1975). “An empirical relationship between interplanetary conditions and Dst”. In: *Journal of Geophysical Research* 80.31, p. 4204.
- Cade III, William B and Christina Chan-Park (2015). “The origin of “Space Weather””. In: *Space Weather* 13.2, pp. 99–103.
- Cane, HV and IG Richardson (2003). “Interplanetary coronal mass ejections in the near-Earth solar wind during 1996–2002”. In: *Journal of Geophysical Research (Space Physics)* 108.A4.
- Cargill, Peter J (2004). “On the aerodynamic drag force acting on interplanetary coronal mass ejections”. In: *Solar Physics* 221.1, pp. 135–149.
- Cargill, PJ et al. (1996). “Magnetohydrodynamic simulations of the motion of magnetic flux tubes through a magnetized plasma”. In: *Journal of Geophysical Research (Space Physics)* 101.A3, pp. 4855–4870.
- Carrington, Richard Christopher (1859). “On certain phenomena in the motions of solar spots”. In: *Monthly Notices of the Royal Astronomical Society* 19, pp. 81–84.
- Cassak, P. A. and M. A. Shay (Oct. 2007). “Scaling of asymmetric magnetic reconnection: General theory and collisional simulations”. In: *Physics of Plasmas* 14.10, 102114, p. 102114.
- Chen, J. and V. Kunkel (July 2010). “Temporal and Physical Connection Between Coronal Mass Ejections and Flares”. In: *The Astrophysical Journal* 717, pp. 1105–1122.
- Chen, James (1989). “Effects of toroidal forces in current loops embedded in a background plasma”. In: *The Astrophysical Journal* 338, pp. 453–470.

- Cheng, C. Z. et al. (Oct. 2003). “Flux Rope Acceleration and Enhanced Magnetic Reconnection Rate”. In: *The Astrophysical Journal* 596, pp. 1341–1346.
- Cho, K.-S. et al. (Dec. 2003). “A statistical comparison of interplanetary shock and CME propagation models”. In: *Journal of Geophysical Research (Space Physics)* 108, 1445, p. 1445.
- Cho, K.-S. et al. (May 2013). “Comparison of Helicity Signs in Interplanetary CMEs and Their Solar Source Regions”. In: *Solar Physics* 284, pp. 105–127.
- Choudhuri, Arnab Rai (1998). *The Physics of Fluids and Plasmas: An Introduction for Astrophysicists*. Cambridge University Press.
- (2003). “On the connection between mean field dynamo theory and flux tubes”. In: *Solar Physics* 215.1, pp. 31–55.
- Cranmer, Steven R (2009). “Coronal holes”. In: *Living Reviews in Solar Physics* 6.1, p. 3.
- Crooker, NU et al. (1985). “Magnetic field draping against the dayside magnetopause”. In: *Journal of Geophysical Research (Space Physics)* 90.A4, pp. 3505–3510.
- Dasso, S. et al. (Oct. 2003). “Magnetic helicity analysis of an interplanetary twisted flux tube”. In: *Journal of Geophysical Research (Space Physics)* 108, 1362, p. 1362.
- Dasso, S. et al. (Aug. 2006). “A new model-independent method to compute magnetic helicity in magnetic clouds”. In: *Astron. Astrophys.* 455, pp. 349–359.
- Dasso, S. et al. (Aug. 2007). “Progressive Transformation of a Flux Rope to an ICME. Comparative Analysis Using the Direct and Fitted Expansion Methods”. In: *Solar Physics* 244, pp. 115–137.
- Dasso, Sergio et al. (2005). “Linking coronal to heliospheric magnetic helicity: A new model-independent technique to compute helicity in magnetic clouds”. In: *Solar Wind 11/SOHO 16, Connecting Sun and Heliosphere*. Ed. by H. Lacoste B. Fleck T.H. Zurbuchen. Noordwijk, The Netherlands : ESA Publications Division, ESTEC, 2005, p. 605.
- Démoulin, P., S. Dasso, and M. Janvier (2013). “Does spacecraft trajectory strongly affect detection of magnetic clouds?” In: *Astron. Astrophys.* 550, A3, A3.

- Démoulin, P., M. Janvier, and S. Dasso (Feb. 2016). “Magnetic Flux and Helicity of Magnetic Clouds”. In: *Solar Physics* 291, pp. 531–557.
- Démoulin, P, E Pariat, and MA Berger (2006). “Basic properties of mutual magnetic helicity”. In: *Solar Physics* 233.1, pp. 3–27.
- Démoulin, P, ER Priest, and DP Lonie (1996). “Three-dimensional magnetic reconnection without null points: 2. Application to twisted flux tubes”. In: *Journal of Geophysical Research (Space Physics)* 101.A4, pp. 7631–7646.
- Démoulin, P. et al. (Feb. 2002). “What is the source of the magnetic helicity shed by CMEs? The long-term helicity budget of AR 7978”. In: *Astronomy & Astrophysics* 382, pp. 650–665.
- Démoulin, Pascal and S Dasso (2009). “Causes and consequences of magnetic cloud expansion”. In: *Astronomy & Astrophysics* 498.2, pp. 551–566.
- Démoulin, Pascal et al. (2008). “Expected in situ velocities from a hierarchical model for expanding interplanetary coronal mass ejections”. In: *Solar Physics* 250.2, pp. 347–374.
- Deng, Minda and Brian T Welsch (2017). “The roles of reconnected flux and overlying fields in CME speeds”. In: *Solar Physics* 292.1, p. 17.
- DeVore, C. R. (Aug. 2000). “Magnetic Helicity Generation by Solar Differential Rotation”. In: *The Astrophysical Journal* 539, pp. 944–953.
- Domingo, V., B. Fleck, and A. I. Poland (Dec. 1995). “The SOHO Mission: an Overview”. In: *Solar Physics* 162, pp. 1–37.
- Downs, Cooper et al. (2016). “Closed-field coronal heating driven by wave turbulence”. In: *The Astrophysical Journal* 832.2, p. 180.
- Driel-Gesztelyi, Lidia van and Lucie May Green (2015). “Evolution of active regions”. In: *Living Reviews in Solar Physics* 12.1, p. 1.
- Dumbović, M. et al. (Feb. 2018). “The Drag-based Ensemble Model (DBEM) for Coronal Mass Ejection Propagation”. In: *The Astrophysical Journal* 854, 180, p. 180.
- Dumbović, Mateja et al. (2018). “The drag-based ensemble model (DBEM) for coronal mass ejection propagation”. In: *The Astrophysical Journal* 854.2, p. 180.
- Dungey, James W (1961). “Interplanetary magnetic field and the auroral zones”. In: *Physical Review Letters* 6.2, p. 47.

- Eastwood, JP et al. (2017). “The scientific foundations of forecasting magnetospheric space weather”. In: *Space Science Reviews* 212.3-4, pp. 1221–1252.
- Echer, E, WD Gonzalez, and MV Alves (2006). “On the geomagnetic effects of solar wind interplanetary magnetic structures”. In: *Space Weather* 4.6, pp. 1–11.
- Elsasser, Walter M (1956). “Hydromagnetic dynamo theory”. In: *Reviews of modern Physics* 28.2, p. 135.
- Engvold, Oddbjørn (2015). “Description and classification of prominences”. In: *Solar prominences*. Springer, pp. 31–60.
- Erdős, G. and A. Balogh (Jan. 2014). “Magnetic Flux Density in the Heliosphere through Several Solar Cycles”. In: *Astrophys. J.* 781, 50, p. 50.
- Fainshtein, V. G., T. E. Popova, and L. K. Kashapova (Dec. 2012). “Magnetic field dynamics based on SOHO/MDI data in the region of flares related to halo coronal mass ejections”. In: *Geomagnetism and Aeronomy* 52, pp. 1075–1086.
- Falconer, D. et al. (Apr. 2011). “A tool for empirical forecasting of major flares, coronal mass ejections, and solar particle events from a proxy of active-region free magnetic energy”. In: *Space Weather* 9, S04003, S04003.
- Falconer, D. A., R. L. Moore, and G. A. Gary (Dec. 2008). “Magnetogram Measures of Total Nonpotentiality for Prediction of Solar Coronal Mass Ejections from Active Regions of Any Degree of Magnetic Complexity”. In: *The Astrophysical Journal* 689, 1433-1442, pp. 1433–1442.
- Falconer, DA (2001). “A prospective method for predicting coronal mass ejections from vector magnetograms”. In: *Journal of Geophysical Research (Space Physics)* 106.A11, pp. 25185–25190.
- Farrugia, C. J. et al. (May 1993). “A study of an expanding interplanetary magnetic cloud and its interaction with the earth’s magnetosphere - The interplanetary aspect”. In: *Journal of Geophysical Research* 98, pp. 7621–7632.
- Farrugia, Charles et al. (Feb. 1992). “A comparative study of dynamically expanding force-free, constant-alpha magnetic configurations with applications to magnetic clouds”. In: *Journal of Geophysical Research (Space Physics)*.
- Fenrich, F. R. and J. G. Luhmann (1998). “Geomagnetic response to magnetic clouds of different polarity”. In: *Geophys. Res. Lett.* 25, pp. 2999–3002.

- Finlay, Christopher (2007). “Alfvén Waves”. In: *Encyclopedia of Geomagnetism and Paleomagnetism*. Ed. by David Gubbins and Emilio Herrero-Bervera. Dordrecht: Springer Netherlands, pp. 3–6.
- Flynn, Sierra et al. (2018). “Understanding the global variability in thermospheric nitric oxide flux using empirical orthogonal functions (EOFs)”. In: *Journal of Geophysical Research (Space Physics)* 123.5, pp. 4150–4170.
- Forbes, T. G. (Oct. 2000). “A review on the genesis of coronal mass ejections”. In: *Journal of Geophysical Research* 105, pp. 23153–23166.
- Forbes, TG and LW Acton (1996). “Reconnection and field line shrinkage in solar flares”. In: *The Astrophysical Journal* 459, p. 330.
- Fox, NJ et al. (2016). “The solar probe plus mission: humanity’s first visit to our star”. In: *Space Science Reviews* 204.1-4, pp. 7–48.
- Fry, C. D. et al. (Feb. 2003). “Forecasting solar wind structures and shock arrival times using an ensemble of models”. In: *Journal of Geophysical Research (Space Physics)* 108, 1070, p. 1070.
- Fuentes, MC López et al. (2000). “The counterkink rotation of a non-Hale active region”. In: *The Astrophysical Journal* 544.1, p. 540.
- Gallagher, P. T., G. R. Lawrence, and B. R. Dennis (May 2003). “Rapid Acceleration of a Coronal Mass Ejection in the Low Corona and Implications for Propagation”. In: *The Astrophysical Journal* 588, pp. L53–L56.
- Gibson, Sarah E, Laurel A Rachmeler, and Stephen M White (2017). “Coronal Magnetometry”. In: *Frontiers in Astronomy and Space Sciences* 4, p. 3.
- Gibson, SE and BC Low (1998). “A time-dependent three-dimensional magnetohydrodynamic model of the coronal mass ejection”. In: *The Astrophysical Journal* 493.1, p. 460.
- Goldstein, H. (Nov. 1983). “On the field configuration in magnetic clouds”. In: *NASA Conference Publication*. Vol. 228. NASA Conference Publication.
- Gonzalez, W. D. and E. Echer (Sept. 2005). “A study on the peak Dst and peak negative Bz relationship during intense geomagnetic storms”. In: 32.18, L18103, p. L18103.

- Gonzalez, W. D., L.-C. Lee, and B. T. Tsurutani (Oct. 1990). "Comment on the polarity of magnetic clouds". In: *Journal of Geophysical Research* 95, pp. 17267–17269.
- Gonzalez, Walter D, Bruce T Tsurutani, and Alicia L Clúa De Gonzalez (1999). "Interplanetary origin of geomagnetic storms". In: *Space Science Reviews* 88.3-4, pp. 529–562.
- Gonzalez, WD et al. (1994). "What is a geomagnetic storm?" In: *Journal of Geophysical Research (Space Physics)* 99.A4, pp. 5771–5792.
- Gopalswamy, N (2004). "A global picture of CMEs in the inner heliosphere". In: *The sun and the heliosphere as an integrated system*. Springer, pp. 201–251.
- Gopalswamy, N. (May 2009). "Coronal mass ejections and space weather". In: *Climate and Weather of the Sun-Earth System (CAWSES): Selected Papers from the 2007 Kyoto Symposium, Edited by T. Tsuda, R. Fujii, K. Shibata, and M. A. Geller, p. 77-120*. Ed. by T. Tsuda et al., pp. 77–120.
- Gopalswamy, N. (Dec. 2010). "Corona Mass Ejections: a Summary of Recent Results". In: *20th National Solar Physics Meeting*. Ed. by Ivan Dorotovic. Vol. 20, pp. 108–130.
- Gopalswamy, N. (Dec. 2016). "History and development of coronal mass ejections as a key player in solar terrestrial relationship". In: *Geoscience Letters* 3, 8, p. 8.
- (Sept. 2017d). "Extreme Solar Eruptions and their Space Weather Consequences". In: *ArXiv e-prints*.
- Gopalswamy, N and BJ Thompson (2000). "Early life of coronal mass ejections". In: *Journal of Atmospheric and Solar-Terrestrial Physics* 62.16, pp. 1457–1469.
- Gopalswamy, N. and S. Yashiro (July 2011). "The Strength and Radial Profile of the Coronal Magnetic Field from the Standoff Distance of a Coronal Mass Ejection-driven Shock". In: *The Astrophysical Journal* 736, L17, p. L17.
- Gopalswamy, N, S Yashiro, and S Akiyama (2007). "Geoeffectiveness of halo coronal mass ejections". In: *Journal of Geophysical Research (Space Physics)* 112.A6.
- Gopalswamy, N. et al. (Dec. 2001). "Predicting the 1-AU arrival times of coronal mass ejections". In: *Journal of Geophysical Research* 106, pp. 29207–29218.

- Gopalswamy, N. et al. (Dec. 2005). “Type II radio bursts and energetic solar eruptions”. In: *Journal of Geophysical Research (Space Physics)* 110, A12S07, A12S07.
- Gopalswamy, N et al. (2008). “Solar sources and geospace consequences of interplanetary magnetic clouds observed during solar cycle 23”. In: *Journal of Atmospheric and Solar-Terrestrial Physics* 70.2-4, pp. 245–253.
- Gopalswamy, N. et al. (Apr. 2009). “The SOHO/LASCO CME Catalog”. In: *Earth Moon and Planets* 104, pp. 295–313.
- Gopalswamy, N et al. (2010). “A catalog of halo coronal mass ejections from SOHO”. In: *Sun and Geosphere* 5.1, pp. 7–16.
- Gopalswamy, N. et al. (Nov. 2013a). “Testing the empirical shock arrival model using quadrature observations”. In: *Space Weather* 11, pp. 661–669.
- Gopalswamy, N. et al. (May 2013b). “The Solar Connection of Enhanced Heavy Ion Charge States in the Interplanetary Medium: Implications for the Flux-Rope Structure of CMEs”. In: *Solar Physics* 284, pp. 17–46.
- Gopalswamy, N. et al. (Apr. 2014). “Anomalous expansion of coronal mass ejections during solar cycle 24 and its space weather implications”. In: *Geophysical Research Letters* 41, pp. 2673–2680.
- Gopalswamy, N. et al. (June 2015). “Large Solar Energetic Particle Events Associated with Filament Eruptions Outside of Active Regions”. In: *The Astrophysical Journal* 806, 8, p. 8.
- Gopalswamy, N et al. (2015). “Properties and geoeffectiveness of magnetic clouds during solar cycles 23 and 24”. In: *Journal of Geophysical Research (Space Physics)* 120.11, pp. 9221–9245.
- Gopalswamy, N. et al. (Nov. 2015a). “Properties and geoeffectiveness of magnetic clouds during solar cycles 23 and 24”. In: *Journal of Geophysical Research (Space Physics)* 120, pp. 9221–9245.
- (Nov. 2015b). “Properties and geoeffectiveness of magnetic clouds during solar cycles 23 and 24”. In: *Journal of Geophysical Research (Space Physics)* 120, pp. 9221–9245.

- Gopalswamy, N. et al. (Apr. 2017a). “Estimation of Reconnection Flux Using Post-eruption Arcades and Its Relevance to Magnetic Clouds at 1 AU”. In: *Solar Physics* 292, 65, p. 65.
- Gopalswamy, N. et al. (2017b). “Coronal flux ropes and their interplanetary counterparts”. In: *Journal of Atmospheric and Solar-Terrestrial Physics*.
- Gopalswamy, N. et al. (Sept. 2017c). “A new technique to provide realistic input to CME forecasting models”. In: *ArXiv e-prints*.
- Gopalswamy, Nat (2009). “The CME link to geomagnetic storms”. In: *Proceedings of the International Astronomical Union* 5.S264, pp. 326–335.
- Gopalswamy, Nat et al. (2001). “Predicting the 1-AU arrival times of coronal mass ejections”. In: *Journal of Geophysical Research (Space Physics)* 106.A12, pp. 29207–29217.
- Gosling, J. T. and D. J. McComas (Apr. 1987). “Field line draping about fast coronal mass ejecta - A source of strong out-of-the-ecliptic interplanetary magnetic fields”. In: *Geophys. Res. Lett.* 14, pp. 355–358.
- Gosling, J. T. et al. (Nov. 1974). “Mass ejections from the sun - A view from SKYLAB”. In: *Journal of Geophysical Research* 79, pp. 4581–4587.
- Gosling, Jo T (1990). “Coronal mass ejections and magnetic flux ropes in interplanetary space”. In: *Physics of magnetic flux ropes* 58, pp. 343–364.
- Gosling, John T (1993). “The solar flare myth”. In: *Journal of Geophysical Research (Space Physics)* 98.A11, pp. 18937–18949.
- Green, Lucie and Deb Baker (2015). “Coronal mass ejections: a driver of severe space weather”. In: *Weather* 70.1, pp. 31–35.
- Green, Lucie M. et al. (2018). “The Origin, Early Evolution and Predictability of Solar Eruptions”. In: *Space Science Reviews* 214.1, p. 46.
- Grotian, W. (Mar. 1939). “Zur Frage der Deutung der Linien im Spektrum der Sonnenkorona”. In: *Naturwissenschaften* 27.13, pp. 214–214.
- Gudiksen, Boris V (2004). “The coronal heating problem”. PhD thesis. Institutionen för astronomi.
- Hagyard, MJ et al. (1984). “A quantitative study relating observed shear in photospheric magnetic fields to repeated flaring”. In: *Solar physics* 91.1, pp. 115–126.

- Hale, George E (1908). “On the probable existence of a magnetic field in sun-spots”. In: *The astrophysical journal* 28, p. 315.
- Hale, George E et al. (1919). “The magnetic polarity of sun-spots”. In: *The Astrophysical Journal* 49, p. 153.
- Hapgood, Mike (2019). “The great storm of May 1921: An exemplar of a dangerous space weather event”. In: *Space Weather* 17.7, pp. 950–975.
- Harrison, Richard A (1990). “The source regions of solar coronal mass ejections”. In: *solar physics* 126.1, pp. 185–193.
- Heinemann, Stephan G et al. (2019). “CME–HSS Interaction and Characteristics Tracked from Sun to Earth”. In: *Solar Physics* 294.9, p. 121.
- Hidalgo, MA (2003). “A study of the expansion and distortion of the cross section of magnetic clouds in the interplanetary medium”. In: *Journal of Geophysical Research (Space Physics)* 108.A8.
- Hill, S. M. et al. (Feb. 2005). “The NOAA Goes-12 Solar X-Ray Imager (SXI) 1. Instrument, Operations, and Data”. In: *Solar Physics* 226, pp. 255–281.
- Hoeksema, J. T. et al. (Sept. 2014). “The Helioseismic and Magnetic Imager (HMI) Vector Magnetic Field Pipeline: Overview and Performance”. In: *Solar Physics* 289, pp. 3483–3530.
- Howard, R. A. et al. (Apr. 2008). “Sun Earth Connection Coronal and Heliospheric Investigation (SECCHI)”. In: *Space Science Reviews* 136, pp. 67–115.
- Howard, T. (2014). *Space Weather and Coronal Mass Ejections*.
- Howard, T. A., D. Nandy, and A. C. Koepke (Jan. 2008). “Kinematic properties of solar coronal mass ejections: Correction for projection effects in spacecraft coronagraph measurements”. In: *Journal of Geophysical Research (Space Physics)* 113, A01104, A01104.
- Howard, TA, D Nandy, and AC Koepke (2008). “Kinematic properties of solar coronal mass ejections: Correction for projection effects in spacecraft coronagraph measurements”. In: *Journal of Geophysical Research (Space Physics)* 113.A1.
- Howard, TA et al. (2016). “Measuring the magnetic field of coronal mass ejections near the Sun using pulsars”. In: *The Astrophysical Journal* 831.2, p. 208.
- Howard, Timothy (2011). *Coronal Mass Ejections*. Vol. 376.

- Hu, Q. et al. (Sept. 2014). “Structures of Interplanetary Magnetic Flux Ropes and Comparison with Their Solar Sources”. In: *The Astrophysical Journal* 793, 53, p. 53.
- Hudson, Hugh, Bernhard Haisch, and Keith T Strong (1995). “Comment on “The solar flare myth” by JT Gosling”. In: *Journal of Geophysical Research (Space Physics)* 100.A3, pp. 3473–3477.
- Hundhausen, A (1999). “Coronal mass ejections”. In: *The Many Faces of the Sun*. Springer, pp. 143–200.
- Hundhausen, A. J. (1997). “Coronal Mass Ejections”. In: *Cosmic Winds and the Heliosphere*. Ed. by J. R. Jokipii, C. P. Sonett, and M. S. Giampapa, p. 259.
- Hundhausen, AJ (1993). “Sizes and locations of coronal mass ejections: SMM observations from 1980 and 1984-1989”. In: *Journal of Geophysical Research (Space Physics)* 98.A8, pp. 13177–13200.
- (1995). “The solar wind”. In: *Introduction to space physics*, pp. 91–128.
- Illing, RME and AJ Hundhausen (1985). “Observation of a coronal transient from 1.2 to 6 solar radii”. In: *Journal of Geophysical Research (Space Physics)* 90.A1, pp. 275–282.
- Isavnin, A., A. Vourlidas, and E. K. J. Kilpua (June 2014). “Three-Dimensional Evolution of Flux-Rope CMEs and Its Relation to the Local Orientation of the Heliospheric Current Sheet”. In: 289.6, pp. 2141–2156.
- Isavnin, A, A Vourlidas, and EKJ Kilpua (2013). “Three-dimensional evolution of erupted flux ropes from the Sun (2–20 R) to 1 AU”. In: *Solar Physics* 284.1, pp. 203–215.
- Ishikawa, Shin-nosuke et al. (2017). “Detection of nanoflare-heated plasma in the solar corona by the FOXSI-2 sounding rocket”. In: *Nature Astronomy* 1.11, pp. 771–774.
- Ivanov, K. G., A. F. Kharshiladze, and E. P. Romashets (Feb. 1993). “Manifestation of the magnetic cloud deceleration effect from data on the interplanetary plasma velocity near the earth”. In: *Geomagnetism and Aeronomy* 33.1, pp. 90–95.
- Janvier, M., P. Démoulin, and S. Dasso (Aug. 2013). “Global axis shape of magnetic clouds deduced from the distribution of their local axis orientation”. In: *Astronomy & Astrophysics* 556, A50, A50.

- Jiang, Yunchun et al. (2003). “H α dimmings associated with the X1.6 flare and halo coronal mass ejection on 2001 October 19”. In: *The Astrophysical Journal Letters* 597.2, p. L161.
- Jing, Ju et al. (2005). “Magnetic reconnection rate and flux-rope acceleration of two-ribbon flares”. In: *The Astrophysical Journal* 620.2, p. 1085.
- Jones, R. A. et al. (2007). “Interaction between coronal mass ejections and the solar wind”. In: *Journal of Geophysical Research (Space Physics)* 112.A8, A08107, A08107.
- Kamide, Y. et al. (Aug. 1998). “Current understanding of magnetic storms: Storm-substorm relationships”. In: *Journal of Geophysical Research* 103, pp. 17705–17728.
- Kamide, Y et al. (1998). “Two-step development of geomagnetic storms”. In: *Journal of Geophysical Research (Space Physics)* 103.A4, pp. 6917–6921.
- Kamide, Y. et al. (Apr. 1998). “Two-step development of geomagnetic storms”. In: *Journal of Geophysical Research* 103, pp. 6917–6922.
- Kamide, Yohsuke and Abraham C-L Chian (2007). *Handbook of the solar-terrestrial environment*. Springer Science & Business Media.
- Kay, C and N Gopalswamy (2017). “Using the coronal evolution to successfully forward model CMEs’ in situ magnetic profiles”. In: *Journal of Geophysical Research (Space Physics)* 122.12, pp. 11–810.
- Kay, C and M Opher (2015). “The heliocentric distance where the deflections and rotations of solar coronal mass ejections occur”. In: *The Astrophysical Journal Letters* 811.2, p. L36.
- Kay, C., M. Opher, and R. M. Evans (June 2015). “Global Trends of CME Deflections Based on CME and Solar Parameters”. In: 805.2, 168, p. 168.
- Kazachenko, M. D. et al. (Aug. 2017). “A Database of Flare Ribbon Properties from the Solar Dynamics Observatory. I. Reconnection Flux”. In: *The Astrophysical Journal* 845, 49, p. 49.
- Kazachenko, Maria D et al. (2017). “A Database of Flare Ribbon Properties From Solar Dynamics Observatory I: Reconnection Flux”. In: *arXiv preprint, arXiv:1704.05097*.
- Kilpua, E. K. J. et al. (2017). “Geoeffective Properties of Solar Transients and Stream Interaction Regions”. In: *Space Science Reviews* 212.3, pp. 1271–1314.

- Kim, R.-S. et al. (Apr. 2017). “Relation of CME Speed and Magnetic Helicity in CME Source Regions on the Sun during the Early Phase of Solar Cycles 23 and 24”. In: *Solar Physics* 292, 66, p. 66.
- Klein, Karl-Ludwig and Silvia Dalla (2017). “Acceleration and propagation of solar energetic particles”. In: *Space Science Reviews* 212.3-4, pp. 1107–1136.
- Klein, L. W. and L. F. Burlaga (Feb. 1982). “Interplanetary magnetic clouds at 1 AU”. In: *Journal of Geophysical Research (Space Physics)* 87, pp. 613–624.
- Klimchuk, James A (2006). “On solving the coronal heating problem”. In: *Solar Physics* 234.1, pp. 41–77.
- (2015). “Key aspects of coronal heating”. In: *Philosophical Transactions of the Royal Society A: Mathematical, Physical and Engineering Sciences* 373.2042, p. 20140256.
- Krall, J. and O. C. St. Cyr (2006a). “Flux-Rope Coronal Mass Ejection Geometry and Its Relation to Observed Morphology”. In: *The Astrophysical Journal* 652.2, p. 1740.
- Krall, J and OC St Cyr (2006b). “Flux-rope coronal mass ejection geometry and its relation to observed morphology”. In: *The Astrophysical Journal* 652.2, p. 1740.
- Krall, J. and O. C. St. Cyr (Dec. 2006). “Flux-Rope Coronal Mass Ejection Geometry and Its Relation to Observed Morphology”. In: *The Astrophysical Journal* 652, pp. 1740–1746.
- Kusano, K, Y Suzuki, and K Nishikawa (1995). “A solar flare triggering mechanism based on the Woltjer-Taylor minimum energy principle”. In: *The Astrophysical Journal* 441, pp. 942–951.
- Lagg, Andreas et al. (2017). “Measurements of photospheric and chromospheric magnetic fields”. In: *Space Science Reviews* 210.1-4, pp. 37–76.
- Lang, Kenneth R (2013). *The Sun from space*. Springer Science & Business Media.
- Larmor, J and S Joseph (1919). “Possible rotational origin of magnetic fields of Sun and Earth”. In: *Elec. Rev* 85, p. 412.
- Larson, D. E. et al. (1997). “Tracing the topology of the October 18-20, 1995, magnetic cloud with 0.1 – 10sup 2keV electrons”. In: *Geophysical Research Letters* 24, pp. 1911–1914.
- LaSota, Jack (2013). “STEREO analysis”. PhD thesis.

- Lavraud, B. and J. E. Borovsky (Sept. 2008). “Altered solar wind-magnetosphere interaction at low Mach numbers: Coronal mass ejections”. In: *Journal of Geophysical Research (Space Physics)* 113, A00B08, A00B08.
- Lavraud, B. et al. (Jan. 2014). “Geo-effectiveness and radial dependence of magnetic cloud erosion by magnetic reconnection”. In: *Journal of Geophysical Research (Space Physics)* 119, pp. 26–35.
- Lawrance, M Bendict, YJ Moon, and A Shanmugaraju (Apr. 2020). “Relationships between Interplanetary Coronal Mass Ejection Characteristics and Geoeffectiveness in the Declining Phase of Solar Cycles 23 and 24”. In: *Solar Physics* 295, p. 62.
- Leamon, R. J. et al. (May 2004). “Helicity of magnetic clouds and their associated active regions”. In: *Journal of Geophysical Research (Space Physics)* 109, A05106, A05106.
- Leighton, Robert B (1969). “A magneto-kinematic model of the solar cycle”. In: *The Astrophysical Journal* 156, p. 1.
- Leka, KD and A Skumanich (1999). “On the value of α AR’ from vector magnetograph data”. In: *Solar Physics* 188.1, pp. 3–19.
- Lemen, J. R. et al. (Jan. 2012). “The Atmospheric Imaging Assembly (AIA) on the Solar Dynamics Observatory (SDO)”. In: *Solar Physics* 275, pp. 17–40.
- Lepping, R. P., D. B. Berdichevsky, and T. J. Ferguson (Oct. 2003). “Estimated errors in magnetic cloud model fit parameters with force-free cylindrically symmetric assumptions”. In: *Journal of Geophysical Research (Space Physics)* 108, p. 1356.
- Lepping, R. P., L. F. Burlaga, and J. A. Jones (Aug. 1990). “Magnetic field structure of interplanetary magnetic clouds at 1 AU”. In: *Journal of Geophysical Research* 95, pp. 11957–11965.
- Lepping, RP et al. (2008). “Estimates of magnetic cloud expansion at 1 AU”. In: *Annales Geophysicae*. Vol. 26. 7. Copernicus GmbH, pp. 1919–1933.
- Li, Y. and J. Luhmann (Feb. 2004). “Solar cycle control of the magnetic cloud polarity and the geoeffectiveness”. In: *Journal of Atmospheric and Solar-Terrestrial Physics* 66, pp. 323–331.

- Lin, J. and T. G. Forbes (Feb. 2000). “Effects of reconnection on the coronal mass ejection process”. In: *Journal of Geophysical Research* 105, pp. 2375–2392.
- Lin, Jun (2004). “CME-flare association deduced from catastrophic model of CMEs”. In: *Solar Physics* 219.1, pp. 169–196.
- Lindsay, GM, CT Russell, and JG Luhmann (1995). “Coronal mass ejection and stream interaction region characteristics and their potential geomagnetic effectiveness”. In: *Journal of Geophysical Research (Space Physics)* 100.A9, pp. 16999–17013.
- Liu, Y. et al. (Oct. 2010). “Reconstructing Coronal Mass Ejections with Coordinated Imaging and in Situ Observations: Global Structure, Kinematics, and Implications for Space Weather Forecasting”. In: *The Astrophysical Journal* 722, pp. 1762–1777.
- Longcope, D. et al. (Aug. 2007). “Modeling and Measuring the Flux Reconnected and Ejected by the Two-Ribbon Flare/CME Event on 7 November 2004”. In: *Solar Physics* 244, pp. 45–73.
- Longcope, D. W. and C. Beveridge (Nov. 2007). “A Quantitative, Topological Model of Reconnection and Flux Rope Formation in a Two-Ribbon Flare”. In: *The Astrophysical Journal* 669, pp. 621–635.
- Lopez, R. E. (Oct. 1987). “Solar cycle invariance in solar wind proton temperature relationships”. In: *Journal of Geophysical Research* 92, pp. 11189–11194.
- Lopez, Ramon E, Daniel N Baker, and Joe Allen (2004). “Sun unleashes Halloween storm”. In: *Eos, Transactions American Geophysical Union* 85.11, pp. 105–108.
- Lopez, Ramon E and John W Freeman (1986). “Solar wind proton temperature-velocity relationship”. In: *Journal of Geophysical Research (Space Physics)* 91.A2, pp. 1701–1705.
- Low, B. C. (Aug. 1996). “Solar Activity and the Corona”. In: *Solar Physics* 167, pp. 217–265.
- Lundquist, S. (1951). “On the Stability of Magneto-Hydrostatic Fields”. In: *Phys. Rev.* 83 (2), pp. 307–311.
- Luoni, Maria Luisa et al. (2011). “Twisted flux tube emergence evidenced in longitudinal magnetograms: magnetic tongues”. In: *Solar Physics* 270.1, p. 45.

- Lynch, BJ et al. (2008). “Topological evolution of a fast magnetic breakout CME in three dimensions”. In: *The Astrophysical Journal* 683.2, p. 1192.
- Lynch, BJ et al. (2009). “Rotation of coronal mass ejections during eruption”. In: *The Astrophysical Journal* 697.2, p. 1918.
- Lyot, Bernard (1939). “The study of the solar corona and prominences without eclipses (George Darwin Lecture, 1939)”. In: *Monthly Notices of the Royal Astronomical Society* 99, p. 580.
- Manchester, W. et al. (Nov. 2017). “The Physical Processes of CME/ICME Evolution”. In: *Space Science Reviews* 212, pp. 1159–1219.
- Manchester, W B, B van der Holst, and B Lavraud (2014). “Flux rope evolution in interplanetary coronal mass ejections: the 13 May 2005 event”. In: *Plasma Physics and Controlled Fusion* 56.6, p. 064006.
- Manchester, W. B. et al. (July 2014). “Simulation of magnetic cloud erosion during propagation”. In: *Journal of Geophysical Research (Space Physics)* 119, pp. 5449–5464.
- Manchester, Ward B. et al. (Feb. 2004). “Modeling a space weather event from the Sun to the Earth: CME generation and interplanetary propagation”. In: *Journal of Geophysical Research (Space Physics)* 109.A2, A02107, A02107.
- Mandrini, Cristina Hemilse et al. (2005). “Interplanetary flux rope ejected from an X-ray bright point-The smallest magnetic cloud source-region ever observed”. In: *Astronomy & Astrophysics* 434.2, pp. 725–740.
- Mandrini, Cristina Hemilse et al. (2007). “Are CME-related dimmings always a simple signature of interplanetary magnetic cloud footpoints?” In: *Solar Physics* 244.1-2, pp. 25–43.
- Marsden, RG et al. (1987). “ISEE 3 observations of low-energy proton bidirectional events and their relation to isolated interplanetary magnetic structures”. In: *Journal of Geophysical Research (Space Physics)* 92.A10, pp. 11009–11019.
- Martin, Sara F (1998). “Filament chirality: A link between fine-scale and global patterns”. In: *International Astronomical Union Colloquium*. Vol. 167. Cambridge University Press, pp. 419–429.
- (2003). “Signs of helicity in solar prominences and related features”. In: *Advances in Space Research* 32.10, pp. 1883–1893.

- Martin, Sara F, Rajesh Bilimoria, and Philip W Tracadas (1994). “Magnetic field configurations basic to filament channels and filaments”. In: *Solar surface magnetism*. Springer, pp. 303–338.
- Martin, SF and AH McAllister (1996). “The skew of X-ray coronal loops overlying H α filaments”. In: *Magnetodynamic phenomena in the solar atmosphere*. Springer, pp. 497–498.
- (1997). “Predicting the sign of magnetic helicity in erupting filaments and coronal mass ejections”. In: *Washington DC American Geophysical Union Geophysical Monograph Series 99*, pp. 127–138.
- Marubashi, K. (1986). “Structure of the interplanetary magnetic clouds and their solar origins”. In: *Advances in Space Research 6*, pp. 335–338.
- Marubashi, K (1997). “Interplanetary magnetic flux ropes and solar filaments”. In: *Coronal mass ejections 99*, pp. 147–156.
- Marubashi, K. and R. P. Lepping (2007). “Long-duration magnetic clouds: a comparison of analyses using torus- and cylinder-shaped flux rope models”. In: *Annales Geophysicae 25.11*, pp. 2453–2477.
- Marubashi, K. and R. P. Lepping (Nov. 2007). “Long-duration magnetic clouds: a comparison of analyses using torus- and cylinder-shaped flux rope models”. In: *Annales Geophysicae 25*, pp. 2453–2477.
- Marubashi, K. et al. (Jan. 2012). “Geometry of the 20 November 2003 magnetic cloud”. In: *Journal of Geophysical Research (Space Physics) 117*, A01101, A01101.
- Marubashi, K et al. (2015). “Geometrical relationship between interplanetary flux ropes and their solar sources”. In: *Solar Physics 290.5*, pp. 1371–1397.
- Mays, M. L. et al. (June 2015). “Ensemble Modeling of CMEs Using the WSA-ENLIL+Cone Model”. In: *Solar Physics 290*, pp. 1775–1814.
- Mays, ML et al. (2015). “Ensemble modeling of CMEs using the WSA-ENLIL+Cone model”. In: *Solar Physics 290.6*, pp. 1775–1814.
- McAllister, AH et al. (1995). “Declining Phase Coronal Evolution: The Statistics of X-ray Arcades”. In: *Bulletin of the American Astronomical Society*. Vol. 27, p. 961.

- McComas, D. J. et al. (Apr. 1988). “Interplanetary magnetic field draping about fast coronal mass ejecta in the outer heliosphere”. In: *Journal of Geophysical Research (Space Physics)* 93, pp. 2519–2526.
- McComas, D. J. et al. (July 1998). “Solar Wind Electron Proton Alpha Monitor (SWEPAM) for the Advanced Composition Explorer”. In: *Space Sci. Rev.* 86, pp. 563–612.
- McComas, DJ et al. (1989). “A test of magnetic field draping induced B z perturbations ahead of fast coronal mass ejecta”. In: *Journal of Geophysical Research (Space Physics)* 94.A2, pp. 1465–1471.
- McComas, DJ et al. (2008). “Weaker solar wind from the polar coronal holes and the whole Sun”. In: *Geophysical Research Letters* 35.18.
- McComas, DJ et al. (2013). “Weakest solar wind of the space age and the current “mini” solar maximum”. In: *The Astrophysical Journal* 779.1, p. 2.
- Michalek, G et al. (2006). “Properties and geoeffectiveness of halo coronal mass ejections”. In: *Space Weather* 4.10, pp. 1–17.
- Michalek, Grzegorz and Seiji Yashiro (Aug. 2013). “CMEs and active regions on the sun”. In: *Advances in Space Research* 52, 521–527.
- Mierla, M et al. (2009). “On 3D reconstruction of coronal mass ejections: I. Method description and application to SECCHI-COR data”. In: *Solar Physics* 259.1-2, p. 123.
- Mierla, Marilena et al. (2010). “On the 3-D reconstruction of coronal mass ejections using coronagraph data”. In:
- Miklenic, C. H., A. M. Veronig, and B. Vršnak (June 2009). “Temporal comparison of nonthermal flare emission and magnetic-flux change rates”. In: *Astronomy & Astrophysics* 499, pp. 893–904.
- Moon, Y.-J. et al. (Dec. 2002). “A Statistical Study of Two Classes of Coronal Mass Ejections”. In: *The Astrophysical Journal* 581, pp. 694–702.
- Moore, R. L., A. C. Sterling, and S. T. Suess (Oct. 2007). “The Width of a Solar Coronal Mass Ejection and the Source of the Driving Magnetic Explosion: A Test of the Standard Scenario for CME Production”. In: *The Astrophysical Journal* 668, pp. 1221–1231.

- Moore, RL, MJ Hagyard, and JM Davis (1987). “Flare research with the NASA/MSFC vector magnetograph: Observed characteristics of sheared magnetic fields that produce flares”. In: *Solar Physics* 113.1-2, pp. 347–352.
- Moore, RL and G Roumeliotis (1992). *Eruptive Solar Flares, ed. Z. Svestka, BV Jackson, & ME Machado.*
- Moore, Ronald L (1987). “Observed form and action of the magnetic field in flares”. In: *Solar Physics* 113, pp. 121–124.
- (1988). “Evidence that magnetic energy shedding in solar filament eruptions is the drive in accompanying flares and coronal mass ejections”. In: *The Astrophysical journal* 324, pp. 1132–1137.
- Möstl, C. et al. (Oct. 2008). “Two-spacecraft reconstruction of a magnetic cloud and comparison to its solar source”. In: *Annales Geophysicae* 26, pp. 3139–3152.
- Möstl, Christian et al. (2014). “Connecting speeds, directions and arrival times of 22 coronal mass ejections from the Sun to 1 AU”. In: *The Astrophysical Journal* 787.2, p. 119.
- Mouschovias, T. Ch. and A. I. Poland (Mar. 1978). “Expansion and broadening of coronal loop transients: a theoretical explanation.” In: *The Astrophysical Journal* 220, pp. 675–682.
- Mozer, FS and PL Pritchett (2010). “Spatial, temporal, and amplitude characteristics of parallel electric fields associated with subsolar magnetic field reconnection”. In: *Journal of Geophysical Research (Space Physics)* 115.A4.
- Mulligan, T, CT Russell, and JG Luhmann (1998). “Solar cycle evolution of the structure of magnetic clouds in the inner heliosphere”. In: *Geophysical Research Letters* 25.15, pp. 2959–2962.
- Munro, RH et al. (1979). “The association of coronal mass ejection transients with other forms of solar activity”. In: *Solar Physics* 61.1, pp. 201–215.
- Nakamura, T. K. M. et al. (2018). “Measurement of the Magnetic Reconnection Rate in the Earth’s Magnetotail”. In: *Journal of Geophysical Research (Space Physics)* 123.11, pp. 9150–9168.
- Nandy, D. (Dec. 2006). “Magnetic helicity and flux tube dynamics in the solar convection zone: Comparisons between observation and theory”. In: *Journal of Geophysical Research (Space Physics)* 111, A12S01, A12S01.

- Nandy, D. et al. (May 2007). “A New Technique For Measuring The Twist Of Photospheric Active Regions Without Recourse To The Force-Free-Field Equation: Reconfirming The Hemispheric Helicity Trend”. In: *American Astronomical Society Meeting Abstracts #210*. Vol. 39. Bulletin of the American Astronomical Society, p. 128.
- Nandy, Dibyendu and Arnab Rai Choudhuri (2002). “Explaining the Latitudinal Distribution of Sunspots with Deep Meridional Flow”. In: *Science* 296.5573, pp. 1671–1673.
- Odstrcil, D (2003). “Modeling 3-D solar wind structure”. In: *Advances in Space Research* 32.4, pp. 497–506.
- Odstrcil, D, P Riley, and XP Zhao (2004). “Numerical simulation of the 12 May 1997 interplanetary CME event”. In: *Journal of Geophysical Research (Space Physics)* 109.A2.
- OECD (2018). *National Risk Assessments*, p. 304.
- Osherovich, VA, CJ Farrugia, and LF Burlaga (1993). “Nonlinear evolution of magnetic flux ropes: 1. Low-beta limit”. In: *Journal of Geophysical Research (Space Physics)* 98.A8, pp. 13225–13231.
- Owens, Mathew J and Robert J Forsyth (2013). “The heliospheric magnetic field”. In: *Living Reviews in Solar Physics* 10.1, p. 5.
- Pal, Sanchita et al. (2017). “A Sun-to-Earth Analysis of Magnetic Helicity of the 2013 March 17-18 Interplanetary Coronal Mass Ejection”. In: *Astrophys. J.* 851.2, 123, p. 123.
- Palmerio, Erika et al. (2017). “Determining the intrinsic CME flux rope type using remote-sensing solar disk observations”. In: *Solar Physics* 292.2, p. 39.
- Palmerio, Erika et al. (2018). “Coronal magnetic structure of Earthbound CMEs and in situ comparison”. In: *Space Weather* 16.5, pp. 442–460.
- Parker, E. N. (1957). “Sweet’s Mechanism for Merging Magnetic Fields in Conducting Fluids”. In: *Journal of Geophysical Research* 62.4, pp. 509–520.
- (July 1963). “The Solar-Flare Phenomenon and the Theory of Reconnection and Annihilation of Magnetic Fields.” In: 8, p. 177.
- (Feb. 1973). “The Reconnection Rate of Magnetic Fields”. In: *Astrophys. J.* 180, pp. 247–252.

- Parker, Eugene N (1955). “The Formation of Sunspots from the Solar Toroidal Field.” In: *The astrophysical journal* 121, p. 491.
- (1958). “Dynamics of the interplanetary gas and magnetic fields.” In: *The Astrophysical Journal* 128, p. 664.
- Perreault, Paul and SI Akasofu (1978). “A study of geomagnetic storms”. In: *Geophysical Journal International* 54.3, pp. 547–573.
- Pesnell, W. D., B. J. Thompson, and P. C. Chamberlin (Jan. 2012). “The Solar Dynamics Observatory (SDO)”. In: *Solar Physics* 275, pp. 3–15.
- Petschek, H. E. (1964). “Magnetic Field Annihilation”. In: *NASA Special Publication* 50, p. 425.
- Pevtsov, AA and KS Balasubramaniam (2003). “Helicity patterns on the sun”. In: *Advances in Space Research* 32.10, pp. 1867–1874.
- Poomvises, W., J. Zhang, and O. Olmedo (July 2010). “Coronal Mass Ejection Propagation and Expansion in Three-dimensional Space in the Heliosphere Based on Stereo/SECCHI Observations”. In: *The Astrophysical Journal* 717, pp. L159–L163.
- Poomvises, Watanachak, Jie Zhang, and Oscar Olmedo (2010). “Coronal mass ejection propagation and expansion in three-dimensional space in the heliosphere based on STEREO/SECCHI observations”. In: *The Astrophysical Journal Letters* 717.2, p. L159.
- Priest, ER (1995). “The Sun and its magnetohydrodynamics”. In: *Introduction to space physics*, pp. 58–90.
- Priest, Eric and Terry Forbes (2000). *Magnetic Reconnection: MHD Theory and Applications*. Cambridge University Press.
- Priest, Eric Ronald and DW Longcope (2017). “Flux-rope twist in eruptive flares and CMEs: due to zipper and main-phase reconnection”. In: *Solar Physics* 292.1, p. 25.
- Prölss, Gerd (2012). *Physics of the Earth’s space environment: an introduction*. Springer Science & Business Media.
- Pulkkinen, Tuija (2007). “Space weather: terrestrial perspective”. In: *Living Reviews in Solar Physics* 4.1, p. 1.

- Qiu, J. and V. B. Yurchyshyn (Nov. 2005). “Magnetic Reconnection Flux and Coronal Mass Ejection Velocity”. In: *The Astrophysical Journal* 634, pp. L121–L124.
- Qiu, J. et al. (Apr. 2004). “Magnetic Reconnection and Mass Acceleration in Flare-Coronal Mass Ejection Events”. In: *The Astrophysical Journal* 604, pp. 900–905.
- Qiu, J. et al. (Apr. 2007). “On the Magnetic Flux Budget in Low-Corona Magnetic Reconnection and Interplanetary Coronal Mass Ejections”. In: *The Astrophysical Journal* 659, pp. 758–772.
- Reale, Fabio (2014). “Coronal loops: observations and modeling of confined plasma”. In: *Living Reviews in Solar Physics* 11.1, p. 4.
- Reinard, AA and DA Biesecker (2008). “Coronal mass ejection-associated coronal dimmings”. In: *The Astrophysical Journal* 674.1, p. 576.
- Reiner, MJ et al. (2003). “Constraints on coronal mass ejection dynamics from simultaneous radio and white-light observations”. In: *The Astrophysical Journal* 590.1, p. 533.
- Richardson, I. G. and H. V. Cane (2010). “Near-Earth Interplanetary Coronal Mass Ejections During Solar Cycle 23 (1996–2009): Catalog and Summary of Properties”. In: *Solar Physics* 264.1, pp. 189–237.
- Richardson, Ian G (2018). “Solar wind stream interaction regions throughout the heliosphere”. In: *Living reviews in solar physics* 15.1, p. 1.
- Richardson, IG and HV Cane (2004). “The fraction of interplanetary coronal mass ejections that are magnetic clouds: Evidence for a solar cycle variation”. In: *Geophysical research letters* 31.18.
- Riley, Pete and NU Crooker (2004). “Kinematic treatment of coronal mass ejection evolution in the solar wind”. In: *The Astrophysical Journal* 600.2, p. 1035.
- Riley, Pete et al. (2004). “Fitting flux ropes to a global MHD solution: a comparison of techniques”. In: *Journal of Atmospheric and Solar-Terrestrial Physics* 66.15–16, pp. 1321–1331.
- Rostoker, G and C-G Fälthammar (1967). “Relationship between changes in the interplanetary magnetic field and variations in the magnetic field at the earth’s surface”. In: *Journal of Geophysical Research* 72.23, pp. 5853–5863.

- Rouillard, A. P. et al. (Aug. 2010). “White Light and In Situ Comparison of a Forming Merged Interaction Region”. In: *Astrophys. J.* 719, pp. 1385–1392.
- Ruffenach, A. et al. (Sept. 2012). “Multispacecraft observation of magnetic cloud erosion by magnetic reconnection during propagation”. In: *Journal of Geophysical Research (Space Physics)* 117, A09101, A09101.
- Ruffenach, A. et al. (Jan. 2015). “Statistical study of magnetic cloud erosion by magnetic reconnection”. In: *Journal of Geophysical Research (Space Physics)* 120, pp. 43–60.
- Rust, David M and Ernest Hildner (1976). “Expansion of an X-ray coronal arch into the outer corona”. In: *Solar Physics* 48.2, pp. 381–387.
- Rust, David M and Ashok Kumar (1996). “Evidence for helically kinked magnetic flux ropes in solar eruptions”. In: *The Astrophysical Journal Letters* 464.2, p. L199.
- Sachdeva, Nishtha et al. (2015). “CME Propagation: Where does Aerodynamic Drag ‘Take Over’?” In: *The Astrophysical Journal* 809.2, p. 158.
- Saez, F et al. (2005). “On the 3-dimensional structure of the streamer belt of the solar corona”. In: *Astronomy & Astrophysics* 442.1, pp. 351–358.
- Sahade, Abril, Mariana Cécere, and Gustavo Krause (2020). “Influence of coronal holes on CME deflections: numerical study”. In: *arXiv preprint arXiv:2004.10834*.
- Sarkar, Ranadeep, Nat Gopalswamy, and Nandita Srivastava (2020). “An Observationally Constrained Analytical Model for Predicting the Magnetic Field Vectors of Interplanetary Coronal Mass Ejections at 1 au”. In: *The Astrophysical Journal* 888.2, p. 121.
- Savani, N. P. et al. (2011a). “Evolution of Coronal Mass Ejection Morphology with Increasing Heliocentric Distance. I. Geometrical Analysis”. In: *Astrophys. J.* 731.2, 109, p. 109.
- Savani, N. P. et al. (2011b). “Evolution of Coronal Mass Ejection Morphology with Increasing Heliocentric Distance. II. In Situ Observations”. In: *Astrophys. J.* 732.2, 117, p. 117.
- Savani, N. P. et al. (June 2015). “Predicting the magnetic vectors within coronal mass ejections arriving at Earth: 1. Initial architecture”. In: *Space Weather* 13.6, pp. 374–385.

- Schatten, Kenneth H., John M. Wilcox, and Norman F. Ness (1969). “A model of interplanetary and coronal magnetic fields”. In: *Solar Physics* 6.3, pp. 442–455.
- Scherrer, P. H. et al. (Dec. 1995). “The Solar Oscillations Investigation - Michelson Doppler Imager”. In: *Solar Physics* 162, pp. 129–188.
- Scherrer, P. H. et al. (Jan. 2012). “The Helioseismic and Magnetic Imager (HMI) Investigation for the Solar Dynamics Observatory (SDO)”. In: *Solar Physics* 275, pp. 207–227.
- Schindler, K. and G. Hornig (2000). “Magnetic Reconnection”. In: *Encyclopedia of Astronomy and Astrophysics*. Ed. by P. Murdin, p. 2224.
- Schmidt, J. M. and P. J. Cargill (Jan. 2003). “Magnetic reconnection between a magnetic cloud and the solar wind magnetic field”. In: *Journal of Geophysical Research (Space Physics)* 108, 1023, p. 1023.
- Schmieder, B., G. Aulanier, and B. Vršnak (Dec. 2015). “Flare-CME Models: An Observational Perspective (Invited Review)”. In: *Solar Physics* 290, pp. 3457–3486.
- Schrijver, Carolus J et al. (2015). “Understanding space weather to shield society: A global road map for 2015–2025 commissioned by COSPAR and ILWS”. In: *Advances in Space Research* 55.12, pp. 2745–2807.
- Schwenn, R. et al. (2005). “The association of coronal mass ejections with their effects near the Earth”. In: *Annales Geophysicae* 23.3, pp. 1033–1059.
- Schwenn, R et al. (2006). “Coronal observations of CMEs”. In: *Coronal Mass Ejections*. Springer, pp. 127–176.
- Schwenn, Rainer (1986). “Relationship of coronal transients to interplanetary shocks: 3D aspects”. In: *Space Science Reviews* 44.1-2, pp. 139–168.
- Sheeley, Jr. N. R. et al. (1983). “Associations between coronal mass ejections and soft X-ray events”. In: *The Astrophysical Journal* 272, pp. 349–354.
- Sheeley, Jr. N. R. et al. (1999). “Continuous tracking of coronal outflows: Two kinds of coronal mass ejections”. In: *Journal of Geophysical Research (Space Physics)* 104.A11, pp. 24739–24767.
- Shen, C. et al. (Nov. 2013). “Full halo coronal mass ejections: Do we need to correct the projection effect in terms of velocity?” In: *Journal of Geophysical Research (Space Physics)* 118, pp. 6858–6865.

- Shibata, K c et al. (1995). “Hot-plasma ejections associated with compact-loop solar flares”. In: *The Astrophysical Journal Letters* 451.2, p. L83.
- Shimazu, H. and M. Vandas (July 2002). “A self-similar solution of expanding cylindrical flux ropes for any polytropic index value”. In: *Earth, Planets, and Space* 54, pp. 783–790.
- Shimazu, Hironori and Marek Vandas (2002). “A self-similar solution of expanding cylindrical flux ropes for any polytropic index value”. In: *Earth, planets and space* 54.7, pp. 783–790.
- Shodhan, S. et al. (Dec. 2000). “Counterstreaming electrons in magnetic clouds”. In: *Journal of Geophysical Research* 105, pp. 27261–27268.
- Sinha, Suvadip, Nandita Srivastava, and Dibyendu Nandy (2019). “Solar Filament Eruptions as Precursors to Flare–CME Events: Establishing the Temporal Connection”. In: *The Astrophysical Journal* 880.2, p. 84.
- Smith, C. W. et al. (July 1998). “The ACE Magnetic Fields Experiment”. In: *Space Sci. Rev.* 86, pp. 613–632.
- Smith, E. J. and A. Balogh (Nov. 2008). “Decrease in heliospheric magnetic flux in this solar minimum: Recent Ulysses magnetic field observations”. In: *Geophys. Res. Lett.* 35, L22103, p. L22103.
- Spiegel, EA and NO Weiss (1980). “Magnetic activity and variations in solar luminosity”. In: *Nature* 287.5783, pp. 616–617.
- Srivastava, N. and P. Venkatakrishnan (May 2002). “Relationship between CME Speed and Geomagnetic Storm Intensity”. In: *Geophysical Research Letters* 29, 1287, p. 1287.
- St. Cyr, OC et al. (2000). “Properties of coronal mass ejections: SOHO LASCO observations from January 1996 to June 1998”. In: *Journal of Geophysical Research (Space Physics)* 105.A8, pp. 18169–18185.
- Sterling, Alphonse C and Hugh S Hudson (1997). “Yohkoh SXT observations of X-ray “dimming” associated with a halo coronal mass ejection”. In: *The Astrophysical Journal Letters* 491.1, p. L55.
- Stone, E. C. et al. (July 1998). “The Advanced Composition Explorer”. In: *Space Science Reviews* 86, pp. 1–22.

- Sturrock, Peter A (1989). “The role of eruption in solar flares”. In: *International Astronomical Union Colloquium*. Vol. 104. 1. Cambridge University Press, pp. 387–397.
- Subramanian, P. and K. P. Dere (Nov. 2001). “Source Regions of Coronal Mass Ejections”. In: *The Astrophysical Journal* 561, pp. 372–395.
- Subramanian, Prasad and KP Dere (2001). “Source regions of coronal mass ejections”. In: *The Astrophysical Journal* 561.1, p. 372.
- Subramanian, Prasad et al. (2014). “Self-similar expansion of solar coronal mass ejections: Implications for Lorentz self-force driving”. In: *The Astrophysical Journal* 790.2, p. 125.
- Sugiura, Masahisa et al. (1964). *Part I. Hourly Values of Equatorial Dst for the IGY.: Part. II. Ring Current Variations During the IGY*. Pergamon Press.
- Sun, X. (Sept. 2013). “On the Coordinate System of Space-Weather HMI Active Region Patches (SHARPs): A Technical Note”. In: *ArXiv e-prints*.
- Švestka, Z and EW Cliver (1992). “History and basic characteristics of eruptive flares”. In: *Eruptive Solar Flares*. Springer, pp. 1–11.
- Sweet, P. A. (1958). “14. The neutral point theory of solar flares”. In: *Symposium - International Astronomical Union* 6, 123–134.
- Sweet, P. A. (Jan. 1958). “The Neutral Point Theory of Solar Flares”. In: *Electromagnetic Phenomena in Cosmical Physics*. Ed. by B. Lehnert. Vol. 6, p. 123.
- Takahashi, T. and K. Shibata (Mar. 2017). “Sheath-accumulating Propagation of Interplanetary Coronal Mass Ejection”. In: *The Astrophysical Journal* 837, L17, p. L17.
- Taubenschuss, U. et al. (2010). “The role of magnetic handedness in magnetic cloud propagation”. In: *Annales Geophysicae* 28.5, pp. 1075–1100.
- Temmer, M. et al. (Jan. 2008). “Acceleration in Fast Halo CMEs and Synchronized Flare HXR Bursts”. In: *The Astrophysical Journal* 673, p. L95.
- Temmer, M. et al. (Apr. 2010). “Combined STEREO/RHESSI Study of Coronal Mass Ejection Acceleration and Particle Acceleration in Solar Flares”. In: *The Astrophysical Journal* 712, pp. 1410–1420.

- Thernisien, A. (June 2011). “Implementation of the Graduated Cylindrical Shell Model for the Three-dimensional Reconstruction of Coronal Mass Ejections”. In: *The Astrophysical Journals* 194, 33, p. 33.
- Thernisien, A., A. Vourlidas, and R. A. Howard (May 2009). “Forward Modeling of Coronal Mass Ejections Using STEREO/SECCHI Data”. In: *Solar Physics* 256, pp. 111–130.
- Thernisien, A. F. R., R. A. Howard, and A. Vourlidas (Nov. 2006). “Modeling of Flux Rope Coronal Mass Ejections”. In: *The Astrophysical Journal* 652, pp. 763–773.
- Thompson, BJ et al. (2000). “Coronal dimmings and energetic CMEs in April–May 1998”. In: *Geophysical research letters* 27.10, pp. 1431–1434.
- Thompson, MJ et al. (1996). “Differential rotation and dynamics of the solar interior”. In: *Science* 272.5266, pp. 1300–1305.
- Titov, VS and P Démoulin (1999). “Basic topology of twisted magnetic configurations in solar flares”. In: *Astronomy and Astrophysics* 351, pp. 707–720.
- Tiwari, S. K. et al. (July 2015). “Near-Sun speed of CMEs and the magnetic non-potentiality of their source active regions”. In: *Geophysical Research Letters* 42, pp. 5702–5710.
- Török, T. and B. Kliem (Oct. 2007). “Numerical simulations of fast and slow coronal mass ejections”. In: *Astronomische Nachrichten* 328, p. 743.
- Török, T and Bernhard Kliem (2003). “The evolution of twisting coronal magnetic flux tubes”. In: *Astronomy & Astrophysics* 406.3, pp. 1043–1059.
- (2005). “Confined and ejective eruptions of kink-unstable flux ropes”. In: *The Astrophysical Journal Letters* 630.1, p. L97.
- Tripathi, D, V Bothmer, and H Cremades (2004). “The basic characteristics of EUV post-eruptive arcades and their role as tracers of coronal mass ejection source regions”. In: *Astronomy & Astrophysics* 422.1, pp. 337–349.
- Tsurutani, Bruce T et al. (1988). “Origin of interplanetary southward magnetic fields responsible for major magnetic storms near solar maximum (1978–1979)”. In: *Journal of Geophysical Research (Space Physics)* 93.A8, pp. 8519–8531.

- Van Ballegooijen, AA (1982). “The overshoot layer at the base of the solar convective zone and the problem of magnetic flux storage”. In: *Astronomy and Astrophysics* 113, pp. 99–112.
- Vandas, M et al. (2006). “Comparison of force-free flux rope models with observations of magnetic clouds”. In: *Advances in Space Research* 38.3, pp. 441–446.
- Vandas, Marek, Eugene Romashets, and Athanassios Geranios (2015). “Modeling of magnetic cloud expansion”. In: *Astronomy & Astrophysics* 583, A78.
- Vasyliunas, Vytenis M (1975). “Theoretical models of magnetic field line merging”. In: *Reviews of Geophysics* 13.1, pp. 303–336.
- Vourlidas, A et al. (2000). “Large-angle spectrometric coronagraph measurements of the energetics of coronal mass ejections”. In: *The Astrophysical Journal* 534.1, p. 456.
- Vourlidas, A. et al. (Dec. 2002). “Mass and energy properties of LASCO CMEs”. In: *Solar Variability: From Core to Outer Frontiers*. Ed. by A. Wilson. Vol. 1. ESA Special Publication, pp. 91–94.
- Vourlidas, A et al. (2011). “The first observation of a rapidly rotating coronal mass ejection in the middle corona”. In: *The Astrophysical Journal Letters* 733.2, p. L23.
- Vourlidas, A. et al. (June 2011). “The First Observation of a Rapidly Rotating Coronal Mass Ejection in the Middle Corona”. In: *The Astrophysical Journal* 733, L23, p. L23.
- Vourlidas, A. et al. (May 2013). “How Many CMEs Have Flux Ropes? Deciphering the Signatures of Shocks, Flux Ropes, and Prominences in Coronagraph Observations of CMEs”. In: *Solar Physics* 284, pp. 179–201.
- Vršnak, Bojan et al. (2010). “The role of aerodynamic drag in propagation of interplanetary coronal mass ejections”. In: *Astronomy & Astrophysics* 512, A43.
- Vršnak, Bojan et al. (2013). “Propagation of interplanetary coronal mass ejections: The drag-based model”. In: *Solar physics* 285.1-2, pp. 295–315.
- Vršnak, Bojan et al. (2014). “Heliospheric propagation of coronal mass ejections: comparison of numerical WSA-ENLIL+ Cone model and analytical drag-based model”. In: *The Astrophysical Journal Supplement Series* 213.2, p. 21.

- Vršnak, Bojan et al. (2019). “Heliospheric Evolution of Magnetic Clouds”. In: *The Astrophysical Journal* 877.2, p. 77.
- Vršnak, B. (Oct. 2008). “Processes and mechanisms governing the initiation and propagation of CMEs”. In: *Annales Geophysicae* 26, pp. 3089–3101.
- (Nov. 2016). “Solar eruptions: The CME-flare relationship”. In: *Astronomische Nachrichten* 337, p. 1002.
- Vršnak, B. et al. (July 2007). “Projection effects in coronal mass ejections”. In: *Astronomy & Astrophysics* 469, pp. 339–346.
- Vršnak, B. et al. (July 2013). “Propagation of Interplanetary Coronal Mass Ejections: The Drag-Based Model”. In: *Solar Physics* 285, pp. 295–315.
- Wang, J. et al. (Jan. 1996). “Flares and the Magnetic Nonpotentiality”. In: *The Astrophysical Journal* 456, p. 861.
- Wang, Y. and J. Zhang (June 2008). “A Statistical Study of Solar Active Regions That Produce Extremely Fast Coronal Mass Ejections”. In: *The Astrophysical Journal* 680, 1516-1522, pp. 1516–1522.
- Wang, Y-M, J Lean, and NR Sheeley (2000). “The long-term variation of the Sun’s open magnetic flux”. In: *Geophys. Res. Lett.* 27.4, pp. 505–508.
- Wang, Y.-M. and Jr. N. R. Sheeley (Oct. 1988). “The solar origin of long-term variations of the interplanetary magnetic field strength”. In: *Journal of Geophysical Research (Space Physics)* 93, pp. 11227–11236.
- (July 1995). “Solar Implications of ULYSSES Interplanetary Field Measurements”. In: *Astrophys. J. Lett.* 447, p. L143.
- Wang, Y-M and Jr. N. R. Sheeley (2015). “Coronal mass ejections and the solar cycle variation of the Sun’s open flux”. In: *Astrophys. J. Lett.* 809.2, p. L24.
- Wang, Y-M et al. (2000). “The dynamical nature of coronal streamers”. In: *Journal of Geophysical Research (Space Physics)* 105.A11, pp. 25133–25142.
- Wang, Yi-Ming, Scott H. Hawley, and Neil R. Sheeley (1996). “The Magnetic Nature of Coronal Holes”. In: *Science* 271.5248, pp. 464–469.
- Wang, Yuming et al. (2004). “Deflection of coronal mass ejection in the interplanetary medium”. In: *Solar Physics* 222.2, pp. 329–343.
- Wang, Yuming et al. (Aug. 2004). “Deflection of coronal mass ejection in the interplanetary medium”. In: 222.2, pp. 329–343.

- Wang, Yuming et al. (July 2014). “Deflected propagation of a coronal mass ejection from the corona to interplanetary space”. In: *Journal of Geophysical Research (Space Physics)* 119.7, pp. 5117–5132.
- Wang, Yuming et al. (2018). “Understanding the twist distribution inside magnetic flux ropes by anatomizing an interplanetary magnetic cloud”. In: *Journal of Geophysical Research (Space Physics)* 123.5, pp. 3238–3261.
- Webb, David F (2002). “CMEs and the solar cycle variation in their geoeffectiveness”. In: *From Solar Min to Max: Half a Solar Cycle with SOHO*. Vol. 508, pp. 409–419.
- Webb, David F and Russell A Howard (1994). “The solar cycle variation of coronal mass ejections and the solar wind mass flux”. In: *Journal of Geophysical Research (Space Physics)* 99.A3, pp. 4201–4220.
- Webb, David F and Timothy A Howard (2012). “Coronal mass ejections: observations”. In: *Living Reviews in Solar Physics* 9.1, p. 3.
- Webb, DF et al. (2000). “Relationship of halo coronal mass ejections, magnetic clouds, and magnetic storms”. In: *Journal of Geophysical Research (Space Physics)* 105.A4, pp. 7491–7508.
- Wilson, Robert M (1987). “Geomagnetic response to magnetic clouds”. In: *Planetary and space science* 35.3, pp. 329–335.
- (1990). “On the behavior of the Dst geomagnetic index in the vicinity of magnetic cloud passages at Earth”. In: *Journal of Geophysical Research (Space Physics)* 95.A1, pp. 215–219.
- Woltjer, Lodewijk (1958). “A theorem on force-free magnetic fields”. In: *Proceedings of the National Academy of Sciences of the United States of America* 44.6, p. 489.
- Wu, C.-C. and R. P. Lepping (May 2007). “Comparison of the Characteristics of Magnetic Clouds and Magnetic Cloud-Like Structures for the Events of 1995 - 2003”. In: *Solar Physics* 242, pp. 159–165.
- (2008). “Geomagnetic activity associated with magnetic clouds, magnetic cloud-like structures and interplanetary shocks for the period 1995 2003”. In: *Advances in Space Research* 41, pp. 335–338.
- Wu, C-C and RP Lepping (2006). “Solar cycle effect on geomagnetic storms caused by interplanetary magnetic clouds”. In:

- Xie, H., N. Gopalswamy, and O. C. St. Cyr (May 2013). “Near-Sun Flux-Rope Structure of CMEs”. In: *Solar Physics* 284, pp. 47–58.
- Yashiro, S et al. (2004). “A catalog of white light coronal mass ejections observed by the SOHO spacecraft”. In: *Journal of Geophysical Research (Space Physics)* 109.A7.
- Yashiro, S. et al. (July 2004). “A catalog of white light coronal mass ejections observed by the SOHO spacecraft”. In: *Journal of Geophysical Research (Space Physics)* 109, A07105, A07105.
- Yeates, A. R. et al. (2010). “A nonpotential model for the Sun’s open magnetic flux”. In: *Journal of Geophysical Research (Space Physics)* 115.A9.
- Yeates, Anthony (Oct. 2018). *antyeates1983/pfss: First release of pfss code*.
- Yurchyshyn, Vasyl (2008). “Relationship between EIT posteruption arcades, coronal mass ejections, the coronal neutral line, and magnetic clouds”. In: *The Astrophysical Journal Letters* 675.1, p. L49.
- Zhang, J. et al. (Sept. 2001). “On the Temporal Relationship between Coronal Mass Ejections and Flares”. In: *The Astrophysical Journal* 559, pp. 452–462.
- Zhang, J. et al. (Dec. 2007). “Correction to “Solar and interplanetary sources of major geomagnetic storms (Dst = -100 nT) during 1996-2005””. In: *Journal of Geophysical Research (Space Physics)* 112, A12103.
- Zhang, Jie et al. (2007). “Solar and interplanetary sources of major geomagnetic storms (Dst- 100 nT) during 1996–2005”. In: *Journal of Geophysical Research (Space Physics)* 112.A10.
- Žic, Tomislav, Bojan Vršnak, and Manuela Temmer (2015). “Heliospheric propagation of coronal mass ejections: Drag-based model fitting”. In: *The Astrophysical Journal Supplement Series* 218.2, p. 32.
- Zirker, Jack B (1977). “Coronal holes and high-speed wind streams”. In: *Reviews of Geophysics* 15.3, pp. 257–269.
- Zurbuchen, Thomas H and Ian G Richardson (2006). “In-situ solar wind and magnetic field signatures of interplanetary coronal mass ejections”. In: *Coronal mass ejections*. Springer, pp. 31–43.